

UC Davis

UC Davis Electronic Theses and Dissertations

Title

The Role of Stellar Feedback in Galaxy Evolution

Permalink

<https://escholarship.org/uc/item/63h286cd>

Author

Hirtenstein, Jessie

Publication Date

2021

Peer reviewed|Thesis/dissertation

The Role of Stellar Feedback in Galaxy Evolution

By

JESSICA HIRTENSTEIN
DISSERTATION

Submitted in partial satisfaction of the requirements for the degree of

DOCTOR OF PHILOSOPHY

in

Physics

in the

OFFICE OF GRADUATE STUDIES

of the

UNIVERSITY OF CALIFORNIA

DAVIS

Approved:

Tucker Jones

Maruša Bradač

Andrew Wetzel

Committee in Charge

2021

Contents

Abstract	iv
Acknowledgments	vi
Chapter 1. Introduction	1
1.1. Small Scale Challenges to Λ CDM	4
1.2. Chemical Enrichment Through Cosmic History	6
1.3. Thesis Overview	9
Chapter 2. The OSIRIS Lens-Amplified Survey (OLAS) I: Dynamical Effects of Stellar Feedback in Low Mass Galaxies at $z \sim 2$	11
2.1. Introduction	11
2.2. Data Acquisition	14
2.3. Methods	16
2.4. Analysis	20
2.5. Discussion	25
2.6. Summary	28
Chapter 3. Disentangling the Physical Origin of Emission Line Ratio Offsets at High Redshift With Spatially Resolved Spectroscopy	31
3.1. Introduction	31
3.2. Methodology: Distinguishing Ionization Sources	34
3.3. HST Sample Selection and Spectroscopy	39
3.4. Analysis	44
3.5. Emission Line Powering Mechanisms	48
3.6. Emission line excitation from star forming regions at high redshift	55

3.7. Summary	59
Chapter 4. Conclusion	63
Appendix A. Fire Simulations	66
Appendix B. OLAS Kinematic Maps	67
Appendix C. HST Emission Line Maps	76
Bibliography	84

The Role of Stellar Feedback in Galaxy Evolution

Abstract

Stellar feedback, or the process by which stars inject energy, metals and gas into the interstellar medium (ISM), plays an integral role in the formation and evolution of galaxies. Stellar feedback enriches the ISM with heavy metals formed via star formation, redistributes gas and dust within galaxies, and regulates star formation. In this dissertation I explore the role of stellar feedback in galaxy evolution, namely its ability to alter the dark matter distribution in dwarf galaxies as well as explore systematic effects in measuring galaxy chemical evolution, which is one of the most powerful probes of feedback.

I present the OSIRIS Lens-Amplified Survey (OLAS), a kinematic survey of gravitationally lensed galaxies at $z \sim 1 - 3$ taken with Keck adaptive optics, which is designed to address the so-called ‘cusp-core problem’. Simulations suggest that gaseous outflows driven by stellar feedback can be strong enough to alter the total mass distribution of dwarf galaxies. OLAS probes the stellar mass and specific star formation rate (sSFR) range where simulations predict that stellar feedback is most effective at driving gaseous outflows that create galaxy-wide potential fluctuations which can generate dark matter cores. I find a correlation between sSFR and gas phase velocity dispersion at fixed stellar mass that is consistent with the trend predicted by simulations: feedback from star formation drives star-forming gas and newly formed stars into more dispersion dominated orbits. My results support the scenario that stellar feedback drives gaseous outflows and potential fluctuations, which in turn drive dark matter core formation in dwarf galaxies.

I also present spatially resolved Hubble Space Telescope grism spectroscopy of 15 galaxies at $z \sim 0.8$. I analyze $H\alpha + [N II]$, $[S II]$ and $[S III]$ emission on kiloparsec scales to explore which mechanisms are powering emission lines at high redshifts. A key goal is to test which processes may be responsible for the well-known offset of high redshift galaxies from the $z \sim 0$ locus in the $[O III]/H\beta$ versus $[N II]/H\alpha$ BPT (Baldwin-Phillips-Terlevich) excitation diagram. Offsets in the BPT diagram highlight differing strong emission line ratios (and thus, ISM conditions) at different redshifts, however most studies use strong line ratios measured from local galaxies as a main diagnostic to measure galaxy metallicity. This assumption propagates systematic errors in

metallicity measurements to high redshift, and yields more uncertainty in the effects of feedback (i.e., the amount of mass and metal loss) at high redshifts. I study the spatially resolved emission line maps of $[\text{S II}]/(\text{H}\alpha + [\text{N II}])$ and $[\text{S III}]/[\text{S II}]$ as a function of surface brightness and position within a galaxy to examine evidence for active galactic nuclei (AGN), shocks, diffuse ionized gas (DIG), or escaping ionizing radiation, all of which may contribute to the BPT offsets observed in our sample and therefore cause systematic errors in metallicity measurements. In general I find that the observed emission is dominated by star forming H II regions, indicating that the BPT line ratio offsets are caused by different properties of H II regions at high redshift compared to their local counterparts. I discuss trends with demographic properties and the possible role of α -enhanced abundance patterns in the emission spectra of high redshift galaxies. These results indicate that photo-ionization modeling with stellar population synthesis inputs is a valid tool to explore the specific star formation properties which may cause BPT offsets, to be explored in future work.

Finally, I discuss how future observations and the next generation of telescope facilities will be able to build upon the results of this dissertation to further understand the role of stellar feedback in galaxy formation through cosmic time.

Acknowledgments

There are so many people I'd like to thank who have helped me get to where I am today. First and foremost I'd like to thank my mom, who has been my biggest supporter every step of the way. From teaching me at a young age I can do anything I put my mind to, to consoling me during stressed out late night phone calls and joining me on an observing run at Keck, I truly couldn't have done this without her. I'd also like to thank my brother, Matt, for his never-ending support.

None of this would have been possible without my advisor, Tucker Jones. I started working with Tucker his first year as faculty at UC Davis, and I always like to say in that first year we figured it out together. He has been so supportive over the years and patiently helped introduce me into the world of astronomy. I couldn't have asked for a better advisor.

I would also like to thank Maruša Bradač and Andrew Wetzel for serving on my dissertation committee, along with the rest of the UCD astronomy faculty for their countless words of encouragement and advice over the past six years. I also wouldn't have gotten this far without my undergraduate professors, Jessica Uscinski, Nate Harshman and Phil Johnson. Thank you for creating such an inviting community in the physics department at AU and inspiring me to want to continue on in physics.

I'd like to thank Jenna Samuel, Azalee Bostroem, Ariadna Venegas Li, Anastasiya Salova, Victoria Strait, Rose Baunach, Geoff Chen, Imran Hasan, Chase Hansen, Cameron Saylor, Chris Lugo, and the rest of my cohort and friends I've made while at UC Davis. The countless baking nights, shopping trips, farmers markets and potlucks all balanced out the never-ending work and non-stop stress of a Ph.D., and for that I am forever grateful. I would also like to thank Kathy Muirhead, Marlo Bloom, Lori Interlicchio and CJ Murphy for being my constant support systems.

And lastly, I'd like to thank everyone else's pets that have gotten me through the past six years. A special shoutout to Clyde, Sunny, Higgins, Dui, Poppy, Theodore, Callie, Roxie, Hazel, Froggy and all the other pet friends I've made along the way.

CHAPTER 1

Introduction

One of the major goals in astronomy is to understand how galaxies form and evolve through cosmic time, growing from small over-densities in the early universe into the massive, virialized structures we observe today. The standard cosmological model consists of cold dark matter (CDM) plus dark energy (Λ) driving the expansion of the universe. Within Λ CDM, structure is seeded through adiabatic fluctuations under the force of gravity competing with, and ultimately overcoming cosmic expansion, collapsing into bound, virialized objects that eventually grow into galaxies.

Dark matter dominates the universe's total mass, and therefore gravitational force. To a leading order, we can consider only dark matter under the effects of gravity when generating predictions about galaxy formation and evolution. Based on this assumption, we have a clear theoretical basis of how structures (i.e. dark matter) should grow. In the early universe dark matter amassed and collapsed into virialized halos at low mass scales, and merged hierarchically to form larger halos (e.g., Lacey & Cole 1993, Figure 1.1). In later times the accretion process is much smoother, with a majority of galaxy growth happening in-situ. In reality, galaxies are comprised of two main components, baryonic (or “luminous”) matter, encompassing all stars, gas and dust within a virialized structure, and the dark matter halos in which they reside. Baryons accrete onto these dark matter halos and form visible galaxies. Since baryons are also affected by non-gravitational forces their role in galaxy evolution becomes increasingly complicated.

Λ CDM (without baryons) does is very successful in describing our universe on the largest scales, corroborating observational evidence of large-scale galaxy clustering, cosmic acceleration and measurements of the cosmic microwave background (Planck Collaboration et al., 2020). However, it is incomplete and thus is not able to predict galaxy properties on small scales, such as the number of satellite galaxies surrounding the Milky Way and the inferred central density profiles of nearby dwarf galaxies. This points to the need to include and better model baryons in Λ CDM models. Possible tensions also may motivate the explorations of revisions to Λ CDM such as modified laws of

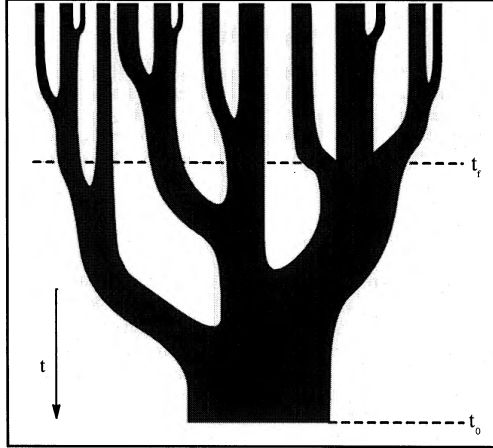


FIGURE 1.1. Reproduced from Lacey & Cole (1993)¹. A schematic representation of a dark matter halo merger tree, illustrating hierarchical structure formation. In this figure time increases from top to bottom, and each branch represents a dark matter halo, with the width of branches representing each halos mass. The present time, t_0 , and the formation time, t_f , are noted by horizontal dashed lines, where t_f is defined as the time at which the parent halo containing more than half of the mass of the final halo was created. From this schematic, we can see that in early times dark matter clumps and collapses into small halos, which over time merge into the massive dark matter halos that host galaxies today.

gravity and warm or self-interacting dark matter, or highlights the importance of baryonic physics into our models. This dissertation focuses on the latter, analyzing the importance of stellar feedback in galaxy evolution.

Dark matter and dark energy, despite making up a combined $\sim 96\%$ of the critical density of the universe, has not yet been directly detected. Therefore, a majority of our understanding of galaxies and how they evolve comes from observations of the luminous matter that makes up only a small fraction of our universe. Through careful observations from ground and space-based telescopes, we are able to detect galaxies over 13 billion years in the past, just 400-500 million years after to the Big Bang. With photometry spanning billions of years we can see variations in galaxy properties such as size, shape and color. In particular, if we place these galaxies chronologically we can begin to create a snapshot timeline, on average, of the history of galaxy formation and evolution across cosmic time. But *how* do galaxies grow from small compact structures into massive spirals

¹Reproduction of Figure 6 from Merger Rates in Hierarchical Models of Galaxy Formation by Lacey, C., and Cole, S., Monthly Notices of the Royal Astronomical Society, Volume 262.

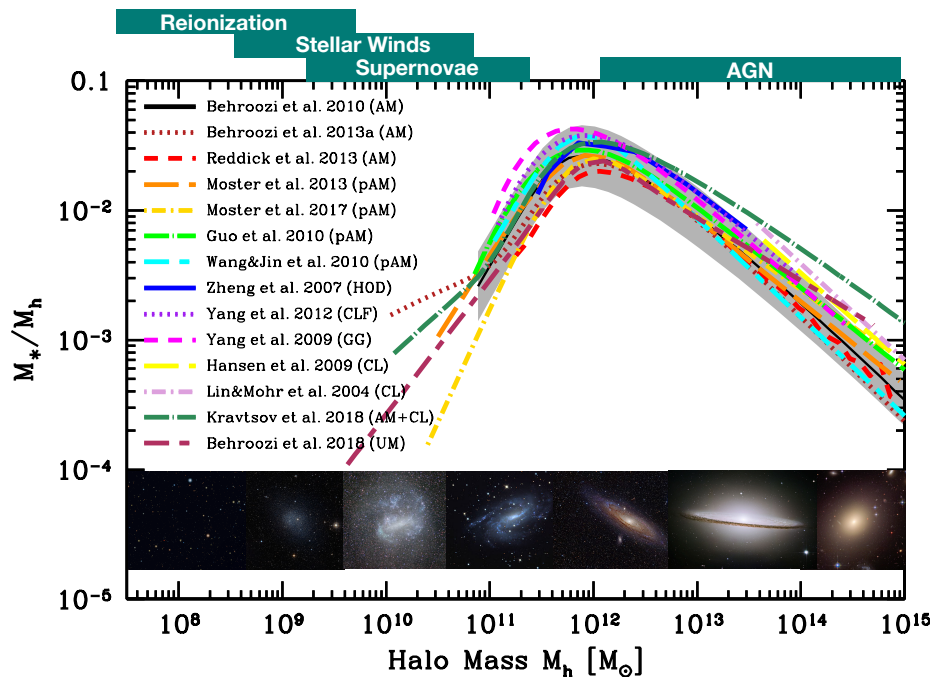


FIGURE 1.2. Reproduced from Wechsler & Tinker (2018)². The stellar mass to halo mass ratio of galaxies at $z = 0$. Galaxies with halo masses of roughly $10^{12} M_{\odot}$ are most efficient at forming stars, noted by the peak in this distribution. AGN feedback suppresses star formation in higher mass halos, while processes such as stellar winds and supernovae, i.e. stellar feedback, are responsible for regulating star formation at the low mass end.

and spheroids? What are the processes that drive their evolution, and how can we observe and characterize them? These are the questions I aim to answer in this dissertation.

Galaxies evolve through repeated cycles of gas accretion, star formation and stellar feedback. Stellar feedback, or the process by which galaxies inject energy, metals, gas and dust into the interstellar medium (ISM), is an integral component of their evolution. Typical feedback processes consist of violent supernovae explosions that exchange newly formed heavy metals via fusion in stellar cores into the ISM and stellar winds redistributing said material throughout the galaxy. Although individual feedback processes occur on small scales, their collective nature culminates into galaxy wide inflows and outflows that disrupt gas distributions and regulate star formation, as seen

²Republished with permission of Annual Reviews, Inc., from Annual Review of Astronomy and Astrophysics Volume 56, The Connection Between Galaxies and Their Dark Matter Halos (2018) by Wechsler, Risa H. and Tinker, Jeremy L.; permission conveyed through Copyright Clearance Center, Inc.

in Figure 1.2. The galaxy stellar mass-to-halo mass ratio peaks for halo masses of $M_h \sim 10^{12} M_\odot$, indicating that typical L^* galaxies like the Milky Way (MW) are most efficient at forming stars. The decrease in this ratio towards both higher and lower halo masses suggests that star formation is suppressed by AGN feedback in higher mass galaxies (which also have reduced star formation efficiency due to reduced gas cooling in the outer halo), and stellar feedback in low mass galaxies.

Stellar feedback is particularly effective in low mass galaxies because the powerful outflows are strong enough to overcome the shallower gravitational potentials that house lower mass galaxies. We also see evidence for the effects of feedback on galaxy evolution through measurements of metal content, where heavy metals are redistributed throughout galaxies via strong feedback episodes, noted in direct trends with the amount of heavy metals and stellar mass, where galaxies with a higher stellar mass have higher metallicities (known as the mass-metallicity relation, MZR). Similarly, the metal enriched circumgalactic medium (CGM) suggests that these outflows are powerful enough to eject gas and metals *outside* of galaxies.

From analysis of emission from star forming regions, we can measure properties such as the velocity dispersion of ionized gas surrounding young stars which traces the potential well of galaxies, and therefore analyze whether stellar feedback from young stars may directly effect the dark matter distribution in dwarf galaxies by flattening their central dark matter density profiles. Similarly, we can measure and analyze specific emission line ratios to distinguish between potential processes that are driving emission, and thus governing galaxy metallicities. Overall, it is clear that analyzing the emission from star forming regions with recent feedback episodes can further inform us of the processes driving galaxy evolution.

1.1. Small Scale Challenges to Λ CDM

Not only is stellar feedback responsible for regulating star formation, but it is also integral in the co-evolution of galaxies and their dark matter halos. The Λ CDM paradigm does an exemplary job of describing the universe on the largest scales, correctly predicting the large scale structure of the universe such as galaxy clusters, filaments and voids. However down to the smallest scales, dwarf galaxies, there are three classic challenges to Λ CDM when comparing dark-matter only simulations

of MW-mass halos to observations of dwarf satellite galaxies around the MW (see Bullock & Boylan-Kolchin (2017) for a comprehensive review of the small scale challenges to Λ CDM).

The first of these small scale challenges to Λ CDM, known as the “Missing Satellites Problem”, details the lack of confirmed MW satellites as compared to the number of predicted dark matter subhalos; dark matter only simulations predict thousands of virialized dark matter subhalos capable of hosting galaxies surrounding their MW-mass host, whereas there are only ~ 60 observationally confirmed satellite galaxies of the MW (Simon, 2019). Next, dark matter only simulations within the Λ CDM paradigm predict dark matter halos with central density profiles that rise very steeply at small radii (referred to as “cusps”), whereas the central density profile of many nearby dwarf galaxies prefer fits to a more constant density core, known as the “Cusp-Core Problem” (Dekel et al., 2021; Oh et al., 2011). Finally, we have the “Too Big To Fail Problem” (Boylan-Kolchin et al., 2011; Read et al., 2006), which stems from instead of assigning observed satellites to simulated halos via abundance matching (i.e., systematically assigning the most massive satellites to the most massive dark matter subhalos) they are alternatively paired by their inferred central masses. With this methodology, the most massive observed MW satellites are never paired with the ~ 10 most massive dark matter subhalos from simulations. Since galaxies were able to form in lower mass dark matter subhalos, we would expect to see galaxies form in the most massive subhalos as well; these most massive subhalos are though to be “too big to fail” at forming galaxies. Similarly, when matching observed MW satellites to simulated dark matter halos via abundance matching, the overall normalization of dark matter in the central regions firmly disagree – fiducial Λ CDM simulations predict satellites to host much more dark matter in their central regions than is measured in observations of satellites around the MW.

These tensions with the Λ CDM paradigm at small scales posed important questions for the field, leading research towards various alternative forms of dark matter to be seriously considered such as warm dark matter (Spergel & Steinhardt, 2000; Viel et al., 2005) and self-interacting dark matter (Buckley & Fox, 2010; Vogelsberger et al., 2014; Zavala et al., 2013). Any credible cosmological theory must look like Λ CDM on large scales while also reproducing properties of present day dwarf galaxies. If these alternative theories could accurately describe all aspects of our universe there would be major implications towards our current understanding of the nature of dark matter.

However we do not need to abandon the CDM paradigm, but rather we should include baryons into our models to invoke baryonic physics and stellar feedback processes. Simulations that include stellar feedback and baryonic physics have shown that they are able to resolve small scale tensions with Λ CDM (e.g., Chan et al., 2015; El-Badry et al., 2016, 2017; Governato et al., 2012; Oñorbe et al., 2015; Pontzen & Governato, 2012; Read et al., 2016; Read et al., 2018). Such simulations suggest that galaxy formation becomes increasingly inefficient within the lowest mass halos, fully suppressing star formation and predicting the smallest dark matter halos to fail to form stars. Similarly, in baryonic simulations the strong gravitational tidal field from the MW-mass central galaxies (which is not present in DM-only simulations) acts to tidally disrupt and destroy many luminous and non-luminous subhalos (resolving the missing satellites problem). If galaxies form enough stars, simulations also predict the energy from supernovae may be able to redistribute dark matter within dwarf galaxies and generate dark matter cores. This suggests that baryonic physics, in particular stellar feedback, plays a vital part in the formation and evolution of galaxies.

However, not all stellar feedback models yield results that alter the central density profile of dwarf galaxies (e.g., Bose et al., 2018). Furthermore, the models that successfully resolve these tensions in the local group with stellar feedback all implement drastically different feedback and star formation prescriptions that predict different galaxy properties at high redshift, such as galaxy masses, chemical enrichment and pollution of the ISM (Davé et al., 2012; Gibson et al., 2013). Observationally, the challenges to Λ CDM are almost entirely based on local universe studies. Therefore, we need high redshift tests to further explore whether stellar feedback may play a critical role in galaxy evolution and distinguish between the high redshift possibilities in numerous hydrodynamic simulations. In Chapter 2 I further explore stellar feedback as an integral driver of galaxy evolution at high redshifts ($z \sim 2$), studying whether feedback may truly be responsible for altering the central dark matter density profiles of galaxies and thus resolving the Cusp-Core problem.

1.2. Chemical Enrichment Through Cosmic History

The same feedback processes that contribute to the dark and baryonic matter co-evolution in galaxies are also responsible for governing their metal content. Heavy metals are produced in galaxies via star formation and enrich the ISM through cycles of stellar winds, violent supernovae

explosions and other gas inflow and outflow mechanisms. The interplay of gas accretion, star formation, stellar feedback and outflows all contribute the baryon cycle and shaping galaxy growth.

Using collisionally excited emission lines we can extract key diagnostics regarding the gas-phase chemical abundances in galaxies, and begin to unravel their histories. One can study the connection between metallicity and stellar mass through the mass-metallicity relation (MZR). As shown in Figure 1.3, there is a distinct trend in metallicity with both stellar mass and redshift. The metallicities of galaxies increases with mass at fixed redshift, and decreases as a function of redshift. As galaxies and their stellar content grow over time, successive generations of stars enrich the ISM with more and more metals. More massive galaxies have more stellar content, and thus more metals overall. The MZR exists in both local galaxies and at high redshifts, allowing us to parse how the interactions between star formation, gas accretion and feedback evolve throughout cosmic history.

Through analyzing metallicity measurements at high redshift we can deepen our understanding of the role of feedback in galaxy evolution. Recent works use the MZR to constrain inflows and outflows as a function of redshift, analyzing factors such as the efficiency of metal removal, mass loading factors in galaxies and gas accretion and recycling (e.g., Anglés-Alcázar et al., 2017; Lilly et al., 2013; Sanders et al., 2018, 2021a). If we can understand how the metal content of galaxies evolves through time we can further analyze the feedback mechanisms that are propelling the chemical evolution and enrichment of galaxies.

Unfortunately, getting accurate measurements of metallicity is not always straightforward. Thus, astronomers use the gas-phase oxygen abundance ($12 + \log \text{O}/\text{H}$) as a main diagnostic for characterizing chemical enrichment. Due to oxygen’s overall abundance relative to other metals and numerous strong emission lines, the gas phase oxygen abundance is often used as a tracer of the ISM metallicity (hereafter, “metallicity” will refer to the gas phase oxygen abundance). The most robust measurement of a galaxy’s oxygen abundance comes from auroral line ratio measurements ($[\text{O III}]\lambda 4363$ to $[\text{O III}]\lambda\lambda 4959, 5007$), which are sensitive to the electron temperature of the ionized gas. Using ratios of strong oxygen lines to Balmer lines, combined with estimates of the electron temperature and density, we can infer the oxygen abundance. This direct method of metallicity measurement cannot be applied to a majority of local galaxies because the $[\text{O III}]\lambda 4363$ line is ~ 100

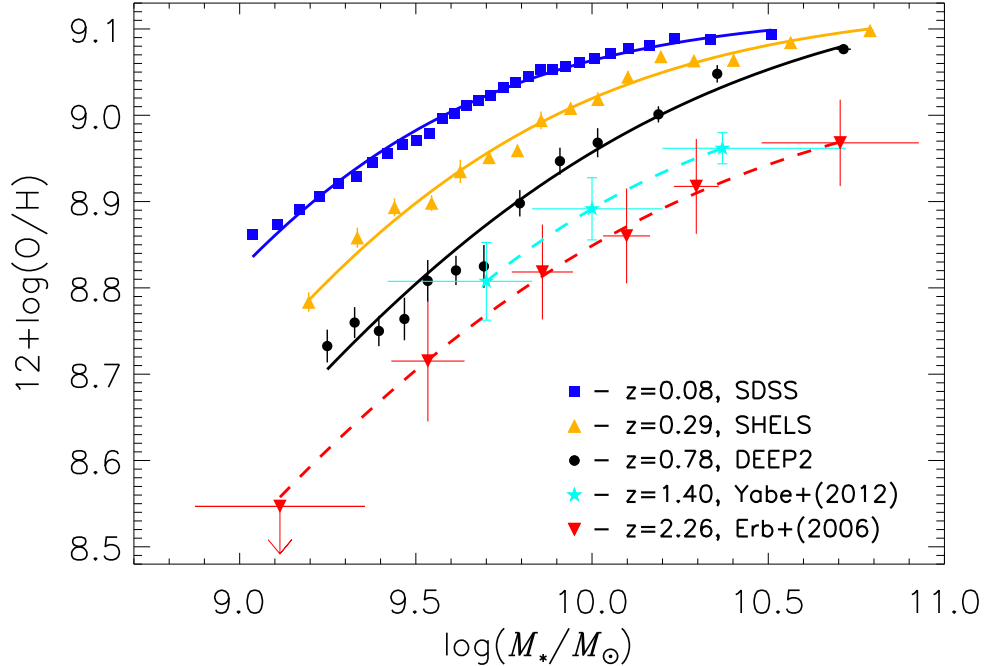


FIGURE 1.3. Reproduced from Zahid et al. (2013)³ (see also, Curti et al. 2020 and Sanders et al. 2021a). Metallicity, quantified through the gas-phase oxygen abundance $12 + \log \text{O}/\text{H}$, plotted against galaxy stellar mass, M_* , showing the mass-metallicity relation at 5 epochs of cosmic time. At fixed redshift, high mass galaxies have more stellar content and thus an increased population for metal production resulting in higher metallicities. Lower redshift galaxies have more evolved stellar populations and have had more time for repeated stellar feedback events to enrich the ISM and increase their overall metallicity. From this relationship we predict that the effects of stellar feedback on galaxy evolution are dependent both on time and galaxy stellar mass.

times weaker than $[\text{O III}]\lambda 5007$. A more practical method of measuring metallicity, although introducing more uncertainty, relies on bright collisionally excited metal lines fit to the relationship between direct T_e metallicities and strong line ratios in H II regions. Common strong line calibrations are based on the line ratios $[\text{N II}]\lambda 6584/\text{H}\alpha$ (Pettini & Pagel, 2004), $([\text{O III}]/\text{H}\beta)/([\text{N II}]/\text{H}\alpha)$ (Pettini & Pagel, 2004), or the “ R_{23} ” ratio $([\text{O III}]\lambda 3727 + [\text{O III}]\lambda\lambda 4959, 5007)/\text{H}\beta$ (Liang et al., 2007; Pilyugin & Thuan, 2005). Finally, one can estimate metallicity through photoionization modeling, using stellar population synthesis to predict the theoretical emission-line ratios at varying input metallicities. However even in local galaxies with high quality observations, each of these

³Reproduced with permission from The Astrophysical Journal Letters, Volume 771, Issue 2, article id. L19, page 6, The Chemical Evolution of Star-Forming Galaxies Over the Last 11 Billion Years (2013) by H. Jabran Zahid et al.

methods introduce their own systematic uncertainties and have measurements that disagree with one another, and thus we do not know which (if any) produces a true measurement of metallicity.

A comprehensive understanding of star formation histories and chemical evolution in galaxies requires accurate metallicity measurements across cosmic time. To measure metallicity at higher redshifts, we currently assume similar environments and use the same strong line ratios as in low redshift galaxies, which we know is an incorrect assumption. In order to correct the systematic errors incurred when applying the local strong line calibrations to high redshift populations we need to understand what is different about the emission line excitation in high redshift galaxies as compared to local galaxies. In order to trust our metallicity measurements across all redshifts and make strong claims about the evolution of heavy metals and star formation histories of galaxies, we need an understanding of the primary mechanisms driving emission lines at high redshift. Chapter 3 explores this idea in more detail, diagnosing the physical processes governing H II regions at high redshift to aid in calibrating metallicity measurements across cosmic time.

1.3. Thesis Overview

Stellar feedback clearly plays a crucial role in the formation and evolution of galaxies, although is still not well understood. There remain many open questions regarding its strength, its role in disrupting galactic kinematics, and governing the enrichment and distribution of metals in galaxies. This dissertation address two main problems regarding the role of feedback through cosmic time.

In Chapter 2 I explore stellar feedback as a resolution to the cusp-core problem at high redshifts. I invoke a novel approach, analyzing the relationship between the velocity dispersion of ionized gas near young stars (tracing the depth of the gravitational potential well, and thus the underlying dark matter distribution) and the specific star formation rate (tracing stellar feedback) in low mass galaxies at $z \sim 2$. This direct relationship suggests a precursor for core formation at high redshifts and provides an observational test for stellar feedback as a resolution to the small scale challenges to one of the small scale tensions with Λ CDM. This is the Accepted Manuscript version of an article accepted for publication in The Astrophysical Journal. IOP Publishing Ltd is not responsible for any errors or omissions in this version of the manuscript or any version derived from it. The Version of Record is available online at [10.3847/1538-4357/ab113e](https://doi.org/10.3847/1538-4357/ab113e).

In Chapter 3 I analyze spatially resolved emission lines to distinguish the primary powering mechanisms driving galaxy emission in a sample of galaxies at $z \sim 0.8$. Essentially all high redshift studies use metallicity diagnostics developed in local galaxies, and rely on the assumption of similar ISM conditions across all redshift ranges. Our results find no significant contribution to observed emission from AGN, shocked gas or diffuse ionized gas (DIG) and suggest that star forming H II regions are the main drivers of observed emission lines at high redshift. Understanding the specific properties that drive emission at high redshift will bring us closer to calibrating metallicity measurements between the low and high redshift universe. This is the version of the article before peer review or editing, as submitted to The Astrophysical Journal (eprint available at <https://arxiv.org/pdf/2106.13810.pdf>).

In Chapter 4 I summarize my main conclusions and discuss paths for future work. The results presented in this dissertation lay groundwork for the quality of data we can expect using the observational capabilities of the next generation of telescopes, such as the James Webb Space Telescope (JWST) and 30-m class Extremely Large Telescopes (ELTs). Larger, deeper datasets with higher resolution will revolutionize the field of observational astronomy, and further constrain the role of stellar feedback in galaxy evolution.

The OSIRIS Lens-Amplified Survey (OLAS) I: Dynamical Effects of Stellar Feedback in Low Mass Galaxies at $z \sim 2$

2.1. Introduction

The standard cosmological model has been tremendously successful in predicting the large-scale structure and distribution of galaxies in terms of dark energy and cold dark matter (Λ CDM; e.g. Planck Collaboration et al. 2018). However in the most common systems, dwarf galaxies ($\log(M_*/M_\odot) \lesssim 8 - 9$), there is tension between the predictions of dark-matter only simulations and observations. Dark-matter only models predict steep central dark matter profiles (referred to as cusps; Navarro et al. 1996; Navarro et al. 2010), yet observed dwarf galaxies in the local universe reveal dark matter halos with a diversity of profiles, with many having nearly constant-density cores (e.g. McGaugh et al. 2001; de Blok et al. 2008). This “cusp-core” problem is one of the most significant and long-standing challenges to standard Λ CDM and has motivated alternative dark matter theories such as warm dark matter (e.g. Spergel & Steinhardt 2000; Viel et al. 2005) and self-interacting dark matter (e.g. Buckley & Fox 2010; Zavala et al. 2013; Vogelsberger et al. 2014) to resolve this tension, among others. Thus, understanding the origin of the cusp-core problem is vital to understanding the dominant mass component of the universe.

One exciting resolution to the cusp-core problem that does not require abandoning Λ CDM is to include baryonic physics in cosmological simulations. Recent works show stellar feedback may be capable of altering the dark matter distribution of dwarf galaxies within the local group (e.g. Governato et al. 2012; Pontzen & Governato 2012; Chan et al. 2015; Oñorbe et al. 2015; Read et al. 2016, El-Badry et al. 2016; El-Badry et al. 2017; Read et al. 2018). These studies show that strong baryonic outflows at sub-kpc scales significantly lower the central density of dark matter halos, resolving the cusp-core problem and revealing the mass range where feedback most significantly drives core formation: stellar masses $M_* \sim 10^6 - 10^9 M_\odot$.

However, not all stellar feedback models alter the central density profile of dwarf galaxies (i.e., Bose et al. 2018). Further, the models that successfully resolve the cusp-core problem in local group dwarfs have different expectations at high redshifts (e.g., Gibson et al. 2013), such as competing implications for galaxy masses, chemical enrichment and pollution of the interstellar and intergalactic media (e.g., Davé et al. 2012).

We are motivated to probe intermediate redshifts ($z \sim 1-3$) from both an observational and theoretical standpoint. Observationally, this epoch corresponds to a peak in star formation rate (SFR) density (see Madau & Dickinson 2014), and thus galaxy assembly activity, where stellar feedback (dominated by young, massive stars) is most active. Similarly, models predict that the strength of galaxy coring can correlate with gas accretion rates and SFRs, so higher redshifts are likely more interesting to test this scenario.

To gain a comprehensive understanding of the impact of stellar feedback on our universe at all epochs, we must discern between these different feedback models. To effectively study density profiles on sub-kpc scales needed to characterize dwarf galaxy structure, we require observations utilizing both adaptive optics (AO) and gravitational lensing. We introduce a new survey, the OSIRIS Lens-Amplified Survey (OLAS), which takes advantage of massive galaxy clusters as gravitational lenses as well as AO at Keck Observatory with the OH-Suppressing Infrared Imaging Spectrograph (OSIRIS), pushing down to roughly 1.5 orders of magnitude lower in both stellar mass and SFR than other similar AO studies at intermediate redshifts (Förster Schreiber et al. 2018), and dramatically extending the sample at the lowest masses for which lensing is necessary (Stark et al. 2008, Jones et al. 2010, Livermore et al. 2015, Contini, T. et al. 2016), as seen in Figure 2.1. Additionally, the AO corrections yield an order of magnitude increase in spatial resolution compared to seeing-limited kinematic studies (e.g. Wuyts et al. 2016, Stott et al. 2016). Typical seeing-limited resolution of $\gtrsim 0.5''$ is insufficient to resolve even our lensed galaxy targets, whereas we achieve good spatial sampling from the combination of AO and lensing magnification. Future work will further explore the resolved kinematics and dynamical mass profiles. Here, we focus on an initial test which is straightforward and theoretically well-motivated.

Here we compare galaxy kinematics with sSFRs to test observational signatures of core formation found in simulations. Physically, bursts of star formation drive powerful outflows which lower

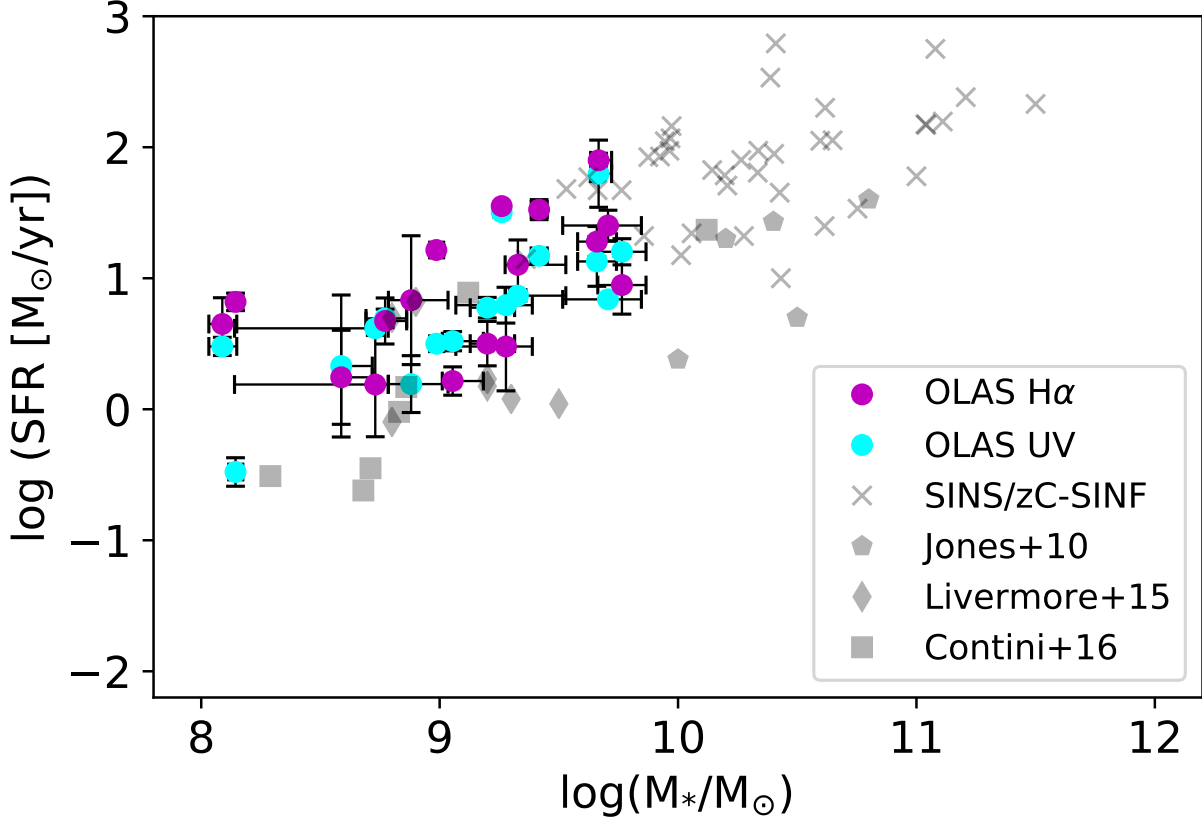


FIGURE 2.1. OLAS stellar masses and SFRs (shaded circles with error bars), with SFR measured from nebular emission lines (purple) and UV-continuum (cyan) for each source, reaching the mass and redshift range where feedback is predicted to have the strongest dynamical effect ($M_* \lesssim 10^9 M_\odot$). Gray data points show similar surveys with varying combinations of AO and lensing (crosses - AO only; Förster Schreiber et al. 2018 (SINS/zC-SINF), pentagons - both AO and lensing; Jones et al. 2010, diamonds - both AO and lensing; Livermore et al. 2015, squares - neither AO nor lensing, Contini, T. et al. 2016, $z > 1$).

the central mass density in galaxies. This rapid change in gravitational potential is expected to drive both baryons and dark matter to wider orbits, manifesting as a lower stellar velocity dispersion, σ_* , with a correlation between σ_* and recent sSFR (El-Badry et al. 2017). The velocity dispersion of stars is a direct indicator of potential fluctuations; here we study the integrated velocity dispersion of H α in star forming regions (denoted as σ , unless otherwise stated). Unlike stars, gas kinematics can be altered due to stellar feedback, regardless of whether or not the gravitational

TABLE 2.1. Overview of observational data

Cluster	ID	z	RA	Dec	Dates	AO	Filter	Scale	t_{exp}	PSF ^a	μ	m_{F160} ^b
					MM/DD/YY			"	s	"		
A370	02056	1.27	02:39:50.260	-01:34:24.20	11/01/17	LGS	Hn1	0.05	3000	0.096	$1.90^{+0.04}_{-0.02}$	23.1
A370	03097	1.55	02:39:50.270	-01:35:02.70	10/30/17	NGS	Hn4	0.1	10800	0.165	$2.30^{+0.11}_{-0.10}$	22.4
A370	03312 ^c	1.60	02:39:47.543	-01:35:12.23	10/30/17	NGS	Hn4	0.1	5400	0.135	$1.90^{+0.04}_{-0.04}$	22.5
M0717	01828	1.47	07:17:39.367	+37:44:31.88	10/25-26/18	LGS	Hn3	0.05	6600	0.131	$3.02^{+0.15}_{-0.14}$	22.9
M0717	02064	2.07	07:17:39.125	+37:44:18.45	11/01/17	LGS	Kn1	0.1	7200	0.136	$6.48^{+0.97}_{-0.79}$	23.3
M0744	00920	1.28	07:44:50.950	+39:27:35.80	10/29/17	NGS	Hn1	0.1	7200	0.192	$20.2^{+2.29}_{-1.72}$	20.7
M0744	01203	1.65	07:44:47.420	+39:27:24.10	10/21/16	LGS	Hn5	0.05	2700	0.092	$3.16^{+0.06}_{-0.06}$	22.0
M0744	02341	1.28	07:44:51.053	+39:26:27.82	10/24/18	LGS	Hn1	0.05	4500	0.281	$2.09^{+0.16}_{-0.07}$	22.5
M1149	00593	1.48	11:49:37.661	+22:24:27.00	06/13/17	LGS	Hn3	0.1	3000	0.281	$1.54^{+0.01}_{-0.00}$	22.2
M1149	00683	1.68	11:49:35.294	+22:24:22.28	06/12/17	LGS	Hn5	0.1	3600	0.149	$4.05^{+0.02}_{-0.01}$	25.5
M1149	01058	1.25	11:49:34.044	+22:24:00.38	06/12/17	LGS	Hn1	0.05	4500	0.104	$2.52^{+0.01}_{-0.00}$	22.5
M1149	01802	2.16	11:49:39.358	+22:23:09.06	05/31/18	LGS	Kn2	0.05	7200	0.062	$2.42^{+0.03}_{-0.03}$	23.1
M1423	00248	1.42	14:23:50.124	+24:05:32.17	06/12/17	LGS	Hn2	0.1	4320	0.164	$2.02^{+0.07}_{-0.07}$	21.7
M2129	00465	1.36	21:29:28.174	-07:40:54.71	10/25/18	LGS	Hn2	0.05	4500	0.127	$1.74^{+0.08}_{-0.04}$	22.1
M2129	00478	1.67	21:29:24.511	-07:40:54.79	06/12/17	LGS	Hn5	0.1	1800	0.228	$1.79^{+0.04}_{-0.03}$	24.5
M2129	01408	1.48	21:29:28.569	-07:42:01.95	06/13/17	LGS	Hn3	0.05	5400	0.207	$1.86^{+0.17}_{-0.13}$	23.5
M2129	01665	1.56	21:29:25.956	-07:42:24.15	10/25/18	LGS	Hn4	0.05	3600	0.075	$1.52^{+0.04}_{-0.03}$	23.1
M2129	01833	2.29	21:29:27.054	-07:42:35.72	06/12/17	LGS	Kn3	0.05	2700	0.129	$1.56^{+0.08}_{-0.05}$	22.1

^a Native point spread functions (PSFs) derived from the full width half max of the tip/tilt star

^b AB magnitude measured in the HST/WFC3-IR F160W filter

^c This object was determined to be an AGN and is excluded from this analysis

potential is significantly affected. Nonetheless, we are testing a predicted correlation between σ and sSFR, which is a necessary, but not sufficient, prerequisite for coring.

This chapter is organized as follows. In Section 2.2 we introduce our target selection criteria and sample. Section 2.3 describes our reduction and data extraction methods, both observationally and from the simulations. In Section 3.4, we discuss the kinematic properties of our sample, present a relationship between σ , M_* , and sSFR from simulations and compare our data with the predicted relationship from the FIRE simulations. In Section 3.5, we discuss our results. Finally, in Section 2.6, we summarize our results and discuss the possibilities this work proposes for future research. We assume a flat Λ CDM cosmology with $H_0 = 70 \text{ km s}^{-1} \text{ Mpc}^{-1}$, $\Omega_m = 0.3$, and $\Omega_\Lambda = 0.7$.

2.2. Data Acquisition

In order to probe stellar feedback at sub-kpc scales in both this critical range of low mass ($\log(M_*/M_\odot) < 9$) and high redshift ($z > 1$), we require high-resolution spatial sampling and kinematic data. For our observations, we use OSIRIS (Larkin et al. 2006), a near-infrared integral field unit (IFU) spectrograph at Keck Observatory with AO, to give us the necessary resolution and spatial sampling for detailed kinematic measurements at the scales of galactic cores.

TABLE 2.2. Data Properties

Cluster	ID	Mass	log(SFR) (UV)	log(SFR) (H α)	Local σ	Integrated σ	Δv^a	v/σ	Kinematic Class ^b
		log(M_*/M_\odot)	log(M_\odot/yr)	log(M_\odot/yr)	km/s	km/s	km/s		
A370	02056	$8.77^{+0.09}_{-0.08}$	$0.69^{+0.06}_{-0.07}$	$0.67^{+0.08}_{-0.18}$	11.7 ± 2.8	33.8 ± 4.5	36	1.53 ± 1.25	2
A370	03097	$9.32^{+0.20}_{-0.05}$	$0.87^{+0.04}_{-0.04}$	$1.10^{+0.20}_{-0.19}$	31.8 ± 2.5	68.8 ± 8.5	134	2.09 ± 0.275	1
M0717	01828	$8.72^{+0.05}_{-0.59}$	$0.61^{+0.05}_{-0.05}$	$0.19^{+0.21}_{-0.40}$	44.2 ± 7.2	50.7 ± 10.5	54	0.61 ± 0.224	2
M0717	02064	$8.08^{+0.06}_{-0.06}$	$0.48^{+0.07}_{-0.07}$	$0.65^{+0.13}_{-0.20}$	42.9 ± 5.3	74.4 ± 8.2	142	1.64 ± 0.288	1
M0744	00920	$9.05^{+0.13}_{-0.04}$	$0.52^{+0.07}_{-0.07}$	$0.21^{+0.11}_{-0.11}$	56.4 ± 1.4	65.5 ± 2.7	262	2.32 ± 0.189	1
M0744	01203	$9.26^{+0.01}_{-0.01}$	$1.50^{+0.03}_{-0.04}$	$1.55^{+0.03}_{-0.03}$	73.4 ± 3.1	97.9 ± 6.5	188	1.28 ± 0.128	1
M0744	02341	$9.19^{+0.11}_{-0.07}$	$0.78^{+0.07}_{-0.08}$	$0.50^{+0.16}_{-0.17}$	62.7 ± 0.99	47.9 ± 10.9	32	0.248 ± 0.150	2
M1149	00593	$9.41^{+0.03}_{-0.03}$	$1.17^{+0.02}_{-0.02}$	$1.52^{+0.07}_{-0.08}$	36.3 ± 2.7	82.6 ± 8.0	158	2.17 ± 0.373	1
M1149	00683	$8.14^{+0.03}_{-0.03}$	$-0.48^{+0.09}_{-0.11}$	$0.82^{+0.06}_{-0.07}$	43.2 ± 3.5	62.9 ± 9.9	102	1.17 ± 0.315	1
M1149	01058	$8.98^{+0.03}_{-0.03}$	$0.50^{+0.01}_{-0.01}$	$1.22^{+0.06}_{-0.04}$	23.4 ± 2.2	51.3 ± 5.1	46	0.965 ± 0.337	2
M1149	01802	$9.70^{+0.14}_{-0.19}$	$0.84^{+0.02}_{-0.02}$	$1.40^{+0.09}_{-0.12}$	55.4 ± 2.8	84.2 ± 4.2	264	2.39 ± 0.255	1
M1423	00248	$9.76^{+0.10}_{-0.10}$	$1.20^{+0.08}_{-0.10}$	$0.95^{+0.16}_{-0.22}$	26.5 ± 5.6	48.8 ± 11.9	52	0.968 ± 0.575	2
M2129	00465	$9.65^{+0.08}_{-0.08}$	$1.13^{+0.13}_{-0.19}$	$1.28^{+0.24}_{-0.12}$	63.4 ± 2.2	80.2 ± 6.0	84	0.655 ± 0.206	2
M2129	00478	$8.58^{+0.13}_{-0.01}$	$0.33^{+0.23}_{-0.54}$	$0.24^{+0.19}_{-0.36}$	22.0 ± 4.2	37.4 ± 10.1	20	0.469 ± 0.359	2
M2129	01408	$8.80^{+0.16}_{-0.09}$	$0.19^{+0.15}_{-0.22}$	$0.83^{+0.09}_{-0.49}$	64.4 ± 1.8	53.8 ± 8.1	54	0.425 ± 0.150	2
M2129	01665	$9.27^{+0.11}_{-0.21}$	$0.79^{+0.10}_{-0.14}$	$0.48^{+0.17}_{-0.34}$	59.0 ± 0.6	40.5 ± 17.4	4	0.03 ± 0.185	2
M2129	01833	$9.60^{+0.05}_{-0.03}$	$1.80^{+0.16}_{-0.26}$	$1.90^{+0.06}_{-0.05}$	79.1 ± 4.5	104.5 ± 13.0	158	1.01 ± 0.165	2

^a Δv is defined here as $v_{max} - v_{min}$.

^b 1: smooth, monotonic velocity gradient, 2: disturbed kinematics.

Our targets are drawn from the Hubble Space Telescope (HST) program, the Grism Lens-Amplified Survey from Space (GLASS; Treu et al. 2015). GLASS obtained near-IR grism spectroscopy of 10 galaxy clusters, detecting spatially resolved emission lines from large samples of background lensed galaxies. GLASS data and other HST imaging provide stellar masses, emission line maps, SFRs and metallicities (as presented in Wang et al. 2017, Wang et al. 2018). OSIRIS followup is critical as HST lacks the spectral resolution to measure kinematics. The GLASS data are necessary to pre-select targets with suitable stellar masses and redshifts. We distinctly look for galaxies with sufficiently strong H α for spatial mapping with OSIRIS that probe the aforementioned critical stellar mass and redshift range to test against simulations. However, this introduces a possible selection effect because our observations are biased towards galaxies with higher sSFRs (stronger H α) whereas the simulations we compare to are not selected based on nebular emission strength. As we note in Section 2.4.2, our observations indeed have higher sSFRs than the simulated galaxies. A larger sample of observational data which pushes to lower sSFR will make this comparison more robust.

Between October 2016 and October 2018, we observed 17 gravitationally lensed, star forming galaxies with redshifts $1.2 < z < 2.3$ and masses $8 < \log(M_*/M_\odot) < 9.8$, one of which was found to be an AGN and is excluded from this analysis. We observed in the H and K bands where the

Strehl ratio is good, at both the 0.05 and 0.1'' pixel scale. The targets are mostly observed with laser guide star (LGS) AO, with some targets observed in the natural guide star (NGS) AO mode during laser failures. The OLAS sample to-date has a median FWHM of 0.136'', observed with clear sky conditions. A more detailed description of our target sample and relevant properties can be found in Tables 2.1 and 2.2.

2.3. Methods

2.3.1. OSIRIS spectroscopic data. OSIRIS provides spatially resolved kinematic information in the form of a 3-D data cube. We reduced the data using the OSIRIS reduction pipeline¹ with a scaled sky subtraction. We perform a sigma-clipping to remove outlier pixels and smooth the data in the spatial directions to increase the signal to noise, yielding a larger area for our kinematic analysis. We then fit a gaussian in velocity space to the H α emission line at each spatial pixel (spaxel) to determine the velocity and local velocity dispersion, imposing a 5σ detection threshold for acceptable fits (Figure 2.2, Appendix B).

We correct the local velocity dispersion (the mean value of σ from individual spaxels) for beam smearing, determined from local velocity shear and the spatial PSF (smoothed according to each science target), as well as instrumental broadening, measured from skylines. In each spaxel, the observed velocity dispersion is corrected by subtracting contributions from both effects in quadrature, yielding a combined median correction of 22.2 km/s (median percent difference of 38.2%). This method corrects for beam smearing due to all resolved velocity shear, regardless of whether the source exhibits rotation or disordered kinematics. The intrinsic local dispersion may still be overestimated if there is unresolved velocity structure, but we adopt this as a conservative approach with no dependence on modeling assumptions.

¹<https://github.com/Keck-DataReductionPipelines/OsirisDRP>

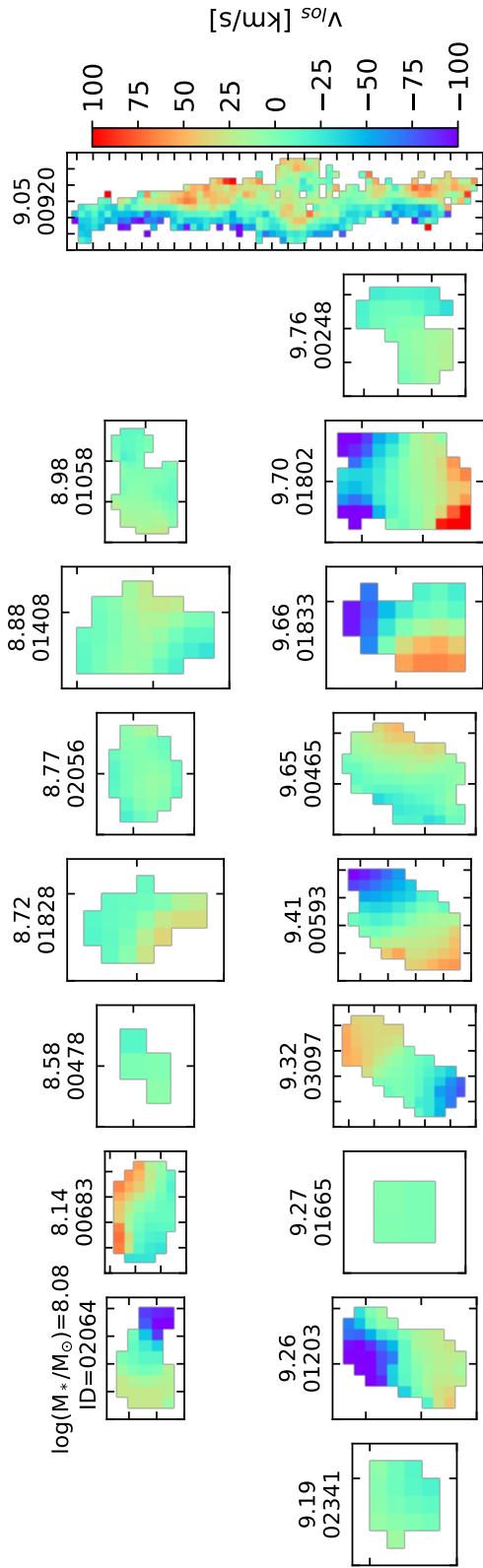


FIGURE 2.2. H α velocity maps for 17 star forming galaxies in our sample observed to date. The galaxies are sorted by stellar mass and are shown with a common velocity scale. Axis tick marks are 0.25 arcseconds in all panels. Targets with $\log(M_*/M_\odot) < 9$ (top row) typically have lower velocity shear, whereas the more massive galaxies on the bottom row predominantly show ordered rotational motion.

We also sum all spaxels into a 1-dimensional spectrum to measure the integrated velocity dispersion for each target. We correct the integrated velocity dispersion measurements for instrumental broadening, subtracting the instrumental contribution from the integrated dispersion in quadrature, yielding a median correction of 10.2 km/s (median percent difference of 15.5%). This allows us to directly compare measured data with the simulations via the framework of El-Badry et al. (2017). The values for local and integrated velocity dispersions are listed in Table 2.2.

2.3.2. Photometry and SED fitting. We determine stellar masses of our targets by modeling their spectral energy distributions (SEDs), following similar methods as our previous work with the GLASS survey (e.g., Jones et al. 2015; Wang et al. 2018). HST photometry from the HFF (Hubble Frontier Fields; Lotz et al. 2017) and CLASH (Cluster Lensing and Supernova Survey with Hubble; Postman et al. 2012) surveys is fit with the stellar population synthesis code FAST (Kriek et al. 2009). We adopt Bruzual & Charlot (2003) spectral templates, Chabrier IMF, solar metallicity, Calzetti et al. (2000) dust attenuation curve, and an exponentially declining star formation history. Each target’s SED is well sampled with at least 7 bands of HST photometry, spanning observed wavelengths 0.4-1.6 μm . In each case we subtract the contribution of strong emission lines [OII], [OIII], $\text{H}\beta$, $\text{H}\alpha$ + [NII], and [SII] from the broad-band continuum (following Jones et al. 2015; emission lines are measured from GLASS data). This correction reduces the derived stellar masses by $\sim 0.1 - 0.2$ dex, with typically larger effects in lower mass galaxies. Resulting best-fit stellar masses are given in Table 2.2.

For this work we are interested in determining SFRs averaged over the last ~ 100 Myr, which we measure from the rest-frame UV continuum. This provides a value which is independent of the $\text{H}\alpha$ -based SFR and probes a longer timescale. We measure UV spectral slopes β (where $f_\lambda \propto \lambda^\beta$) and luminosities using HST F475W and F606W photometry. These filters correspond to rest-frame $\lambda = 1400 - 2600 \text{ \AA}$ for our targets. We use β to correct for UV extinction following Meurer et al. (1999), and calculate SFRs from the UV luminosity following Kennicutt (1998) adjusted for a Chabrier IMF. The results are given in Table 2.2 as SFR (UV). SED modeling also provides estimates of the recent SFR, which are generally consistent. We adopt the direct measurement of SFR from UV continuum as it is insensitive to the assumed star formation history used to model the SEDs.

The stellar masses and SFRs (listed in Table 2.2) are all corrected for lensing magnification (μ ; Table 2.1), with magnification errors included in the uncertainties of the mass estimates. The lens models for the galaxy clusters used in this work were constructed using the lens modeling code Strong and Weak Lensing United (Bradač et al. 2005; Bradač et al. 2009). The code uses strongly and weakly lensed galaxies to reconstruct the gravitational potential on a refined pixel grid. This type of code is often referred to as free-form in that it does not fit the parameters of an analytical mass profile. Lens models for some of the clusters are described in previous works: A370 (Strait et al. 2018), MACS1149 (Finney et al. 2018), MACS1423 (Hoag et al. 2017), MACS2129 (Huang et al. 2016). The lens models for the remaining clusters are described in Hoag et al. (2018, in preparation).

2.3.3. Comparison to simulations. The main objective is to test whether trends between sSFR and $H\alpha$ gas velocity dispersion, σ , predicted by cosmological simulations are in fact present in our data. We compare our results with the Feedback in Realistic Environments (FIRE) simulations, for which galaxies at these masses form dark matter cores via stellar feedback, as a step towards understanding how stellar feedback drives gas kinematics and thus may drive galaxy-wide potential fluctuations and dark matter coring. An overview of the simulated galaxies used are listed in Table A.1, and full details of the simulations are described in Hopkins et al. (2018) and El-Badry et al. (2018b).

El-Badry et al. (2017) measured correlations between stellar kinematics and sSFRs. Given that we most readily measure gas kinematics via nebular emission lines, we recalculate for the FIRE simulations, carefully matching velocity dispersion calculations from FIRE to our observed data. Specifically, we measure $H\alpha$ emission in the observations, so we compare to the HII regions in the simulations, i.e. ionized gas near young stars. In every snapshot (40 snapshots per galaxy), we isolate the ionized gas particles within 100 pc of young (<10 Myr) stars and calculate the density weighted dispersion of their velocities, taking the median value over 100 randomized lines of sight. We do not account for the thermal contribution to σ in our calculations, but they are negligible at these velocity dispersions.

Stellar masses and sSFRs are also determined for each simulated galaxy snapshot. As shown in Table A.1, the simulated galaxies probe the same mass range as our observations. We calculate

sSFR averaged over the last 10 (100) Myr by summing the total mass of stars younger than 10 (100) Myr within a given galaxy, corrected for stellar mass loss, and divide by that same timescale.

2.4. Analysis

2.4.1. Kinematic Maps. We present the lensed (image plane) velocity maps for our sample in Figure 2.2. These maps are generated by plotting the velocity values at every spaxel, extracted as described in Section 2.3.1. Targets with $\log(M_*/M_\odot) < 9$ typically have lower velocity shear, whereas the more massive galaxies predominantly show strong, ordered rotational motion. More detailed kinematic information (including velocity, velocity dispersion and error maps, HST images and H α maps) for each target are presented in Appendix B.

Energetic bursts from stellar feedback episodes may also be strong enough to disrupt gas in galaxies; recent works show stellar feedback may flatten (or in some cases, invert) metallicity gradients and destroy gaseous disks (e.g., Gibson et al. 2013; Leethochawalit et al. 2016; Ma et al. 2017; Wang et al. 2018). This provides yet another test where OLAS is useful to compare to different feedback models. We separate our targets into two kinematic classes: (1) those that exhibit a smooth, monotonic velocity gradient, have $v/\sigma > 1.1$, and available stellar mass map from HST imaging shows no clear signs of merging/disturbance, and (2) those that do not exhibit smooth gradients, have $v/\sigma < 1.1$ or the available stellar mass map shows signs of merging/disturbance. Our choice of v/σ threshold is physically motivated as follows: Rotation supports most of the dynamical mass when $v_{rot} > \sigma\sqrt{2}$ (as measured at the scale radius; Burkert et al. 2010). In addition, the mean measured rotational velocity of randomly oriented disks will be reduced by a factor of $\sin(i) = \pi/4$. Combined, these results yield a cutoff between rotationally supported and dispersion dominated systems with $v/\sigma = 1.1$. This preliminary kinematic classification is to note if there are any immediate trends of galaxy morphology (i.e., rotating disks) with stellar mass, in search of a stellar mass range where stellar feedback may be strong enough to destroy disks.

Figure 2.3 shows the relationship between σ_{local} , v/σ_{local} , and M_* , where v is the peak-to-peak velocity shear ($v = \frac{1}{2}(v_{max} - v_{min})$), and σ_{local} is the mean local (measured per pixel) velocity dispersion of the galaxy (Table 2.2). To examine trends over a wider mass range, we additionally consider the results from the SIGMA survey (Simons et al. 2016) and the KLASS survey (Mason

et al. 2017; we note that the velocity dispersions measured in KLASS being systematically lower than OLAS are likely due to a difference in modeling, particularly in the presence of unresolved velocity shear. Additionally, the samples are small and selection criteria differed between the surveys). If feedback destroys gaseous disks below some threshold mass, we would expect a sharp decrease in v/σ_{local} and/or larger scatter below that stellar mass. We do not see a clear signature of this effect in Figure 2.3. There is a slight positive correlation between σ_{local} with M_* ($r^2 = 0.28$) in the OLAS data. This correlation indicates that velocity dispersion is likely a source of dynamical support at low mass. However we find no evidence of a threshold mass for rotational disk support in the current analysis. This will be explored further in future work with more detailed kinematic classification and disk model fitting.

2.4.2. Relationship between integrated velocity dispersion, mass, sSFR. El-Badry et al. (2017) discuss the relationship between sSFR and stellar velocity dispersion at fixed M_* . We expect qualitatively similar trends for our calculations of velocity dispersion using ionized gas near young stars. To mirror these results, we separate our targets into near constant mass bins of $\log(M_*/M_\odot) \sim 8, 8.6, 8.8, 9.2,$ and 9.7 , matching our observed galaxy masses to galaxies from the FIRE simulations, where all galaxies are within 0.2 dex of their respective mass bin. We compare the integrated velocity dispersion (σ) from OLAS to match our calculations from the FIRE simulations. By examining the relationship between sSFR and σ at fixed stellar mass, we establish a physical link between kinematics and sSFR (i.e. due to feedback-driven outflows), isolated from mass-dependent trends.

Compiling all of our simulated galaxies ranging in stellar masses $7.5 < \log(M_*/M_\odot) < 9.9$, redshifts $1.2 < z < 2.7$ and sSFRs $-11.75 < \log(sSFR_{neb}(M_\odot/yr)) < -7.9$, $-12.6 < \log(sSFR_{UV}(M_\odot/yr)) < -8.3$, we parametrize σ_{pred} from the FIRE simulations (independent of the observed data) into the following general form, where $\sigma_{pred} = \sigma_{pred}(M_*, \text{sSFR})$:

$$(2.1) \quad \log \sigma_{pred} = a \log(sSFR) + b \log(M_*) + c \log(M_*) \log(sSFR),$$

where M_* and sSFR are in units of solar masses (M_\odot) and yr^{-1} . We find no dependence on redshift within the simulated galaxies; including redshift as a parameter does not significantly improve

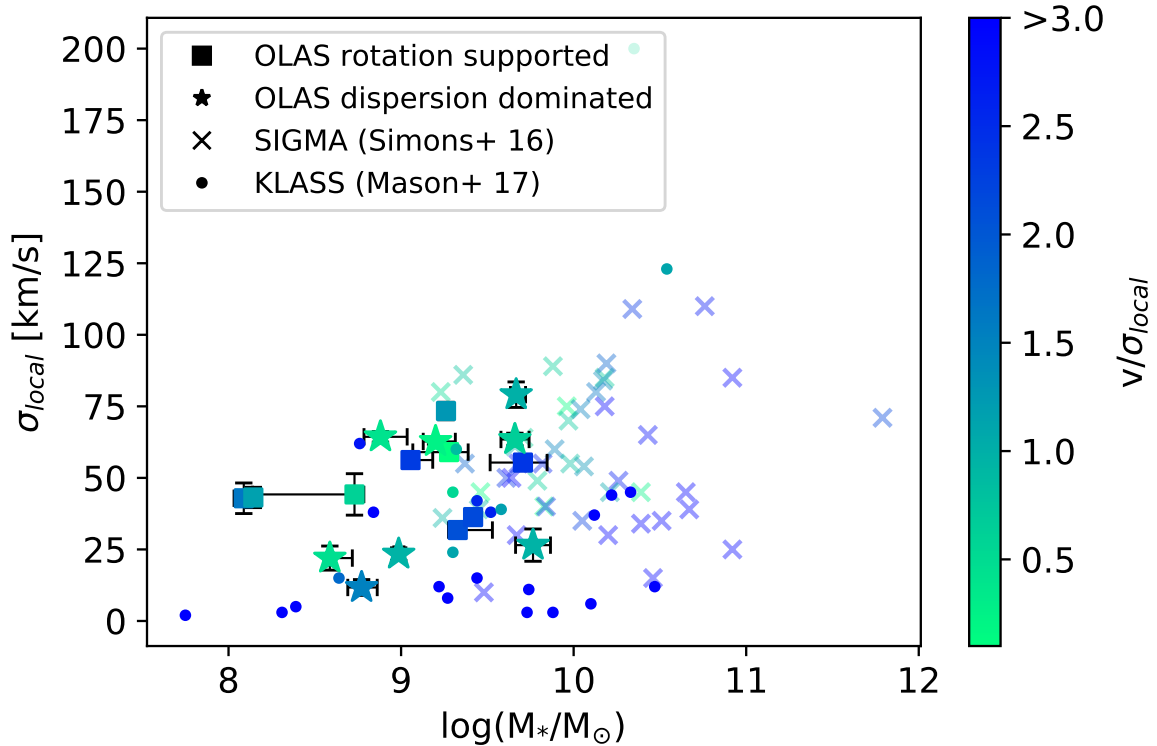


FIGURE 2.3. Local velocity dispersion plotted against stellar mass, color coded by v/σ_{local} (Table 2.2). Filled squares represent OLAS targets with smooth velocity gradients while stars represent those that exhibit disordered kinematics. Crosses show data from the SIGMA survey (Simons et al. 2016) and filled circles are data from the KLASS survey (Mason et al. 2017). The v/σ_{local} is computed differently within the KLASS sample, but we show their values for comparison. We do not see any trend in v/σ_{local} with M_* in the OLAS sample, giving no information of a mass scale where stellar feedback destroys disks.

the fit. This is in agreement with the findings from Hung et al. (2018) where they find intrinsic velocity dispersion within the FIRE simulations to be independent of redshift for $z > 1$. We find the coefficients a , b , and c for both sSFR averaged over 10 and 100 Myr, which we compare to the $H\alpha$ -based and UV-based SFR measurements, respectively, listed in Table 2.3.

The scenario for baryonic coring requires feedback to drive coherent gas outflows on the scale of the entire galaxy, thus causing an increase in σ with increased sSFR. Figure 2.4 shows the best-fit lines compared with both simulations and observed galaxies. At fixed stellar mass, we observe a clear trend in σ with sSFR. This correlation quantitatively supports the hypothesis that star

TABLE 2.3. Fit Parameters From FIRE

sSFR [Myr] ^a	a	b	c	1 σ scatter ^b
10	0.1006	0.3892	0.0126	0.171
100	0.0732	0.4120	0.0181	0.175

^a Timescale (in Myr) over which SFR is averaged.

^b Rms (68%) scatter in $\log \sigma_{pred}$ around the best fit line.

formation and associated feedback indeed have an effect on the gas kinematics, a prerequisite for feedback-driven core formation. However we note that such a correlation may arise from multiple processes; for example a high gas fraction could induce both higher sSFR and velocity dispersion (e.g., Genzel et al. 2011). Nonetheless, equation 2.1 provides a good fit to the simulated galaxies over the full range of stellar mass and sSFR probed. The OLAS observations typically fall within the scatter of the fit. The observed galaxies have generally higher sSFR than the simulated sample, which could potentially introduce a small bias in extrapolating the fit. However we expect no significant effect on the conclusions, and if anything the observational data provide further support that the trend seen in simulations holds over a wide dynamic range. This could be further addressed in future work with an increased sample of simulated galaxies spanning a broader range of sSFR.

2.4.3. Comparing data and simulations. We also compare our observed OLAS velocity dispersions to the predicted values from the simulations using Equation 2.1, combining our data from Figure 2.4 into one relationship (where $\sigma_{pred} = \sigma(M_*, sSFR)$, using SFR averaged over both 10 and 100 Myr). Figure 2.5 presents σ_{pred} compared to OLAS observations. 16/17 observed galaxies are consistent within their 1 σ uncertainties to σ_{pred} with both sSFR averaged over 10 and 100 Myr.

To quantify whether the observational data are consistent with the trend seen in simulations, we compute a linear fit of σ_{obs} vs σ_{pred} . For both SFR averaged over both 10 and 100 Myrs, the results are consistent with expectations to within 1 standard deviation (i.e., unity slope and zero offset). The reduced chi-square values are 0.3 and 0.5 for sSFR averaged over 10 and 100 Myr, respectively, where values less than 1 may indicate observational uncertainties are overestimated, or that simulations over-predict the scatter by 30-50%.

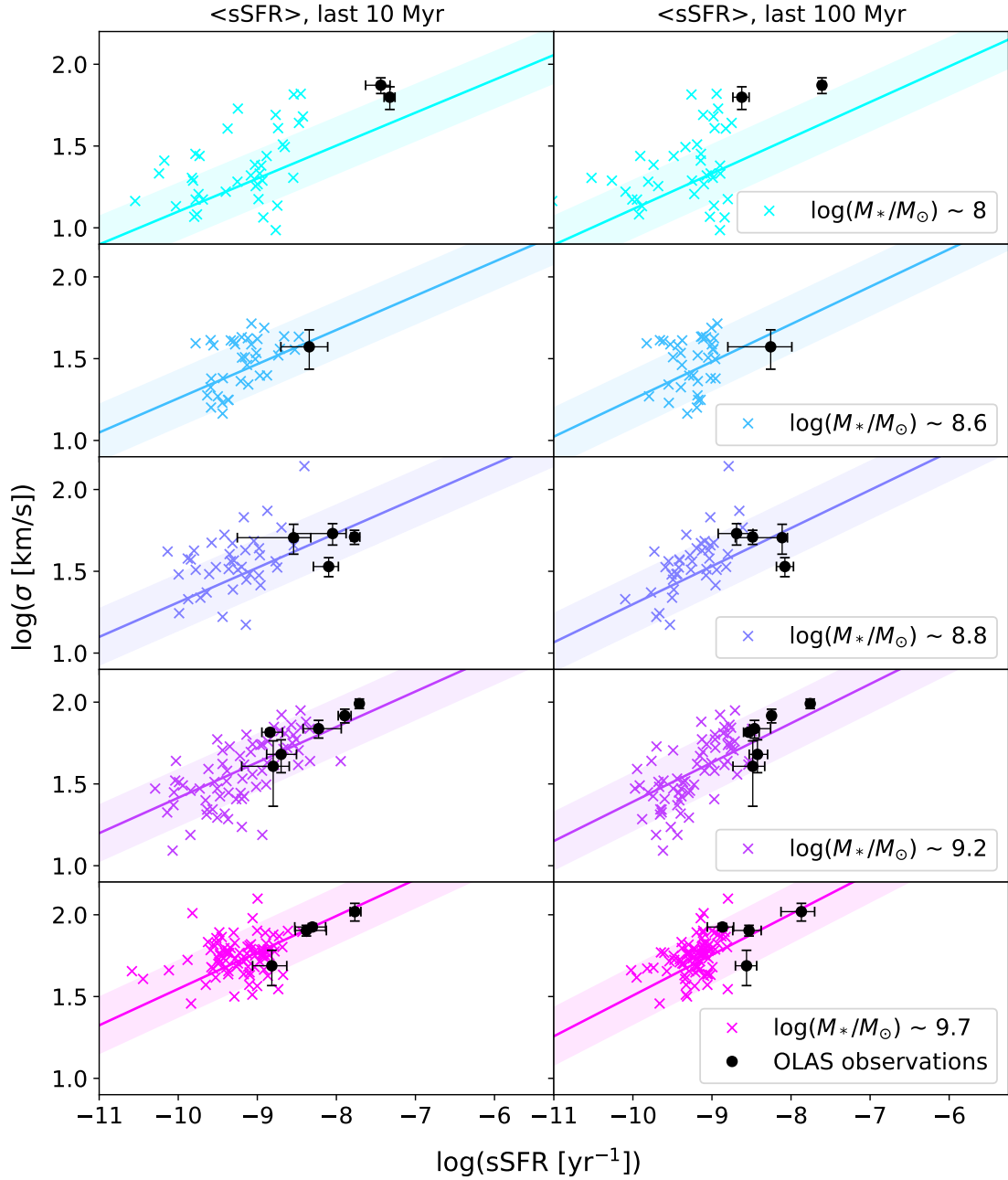


FIGURE 2.4. Colored panels show, at fixed mass, the relationships between integrated σ and sSFR for sSFR averaged over both 10 (left) and 100 (right) Myr, as compared to observed line of sight velocity dispersion from our OSIRIS data (black points with error bars). Crosses represent extracted values from individual simulated galaxies. Solid lines and shaded regions show the dispersion and 1σ scatter from Equation 2.1 evaluated in each panels respective galaxy mass using fitted parameters from Table 2.3.

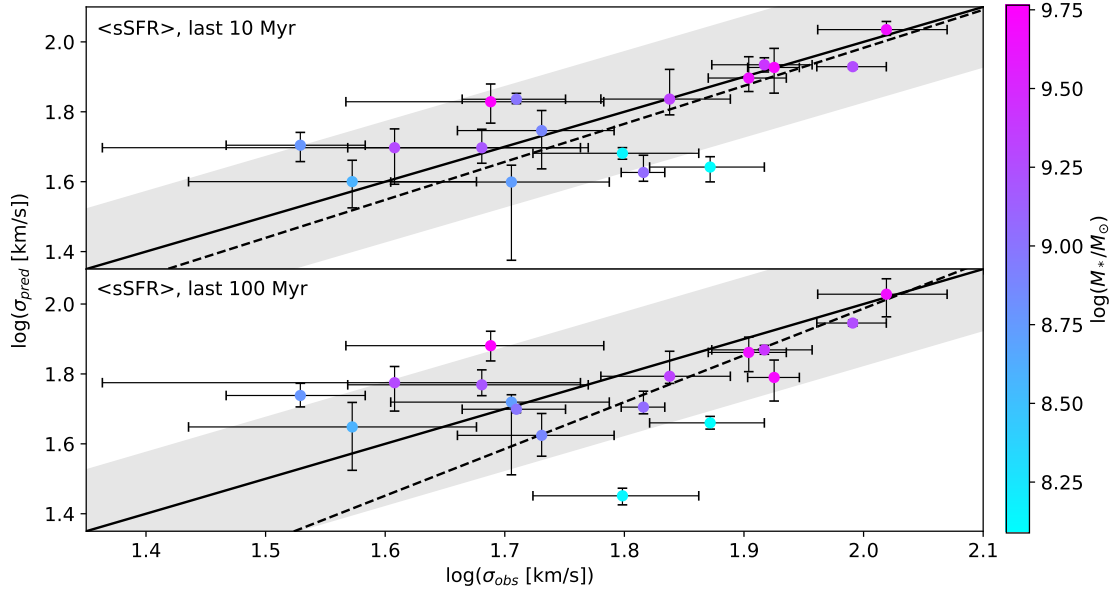


FIGURE 2.5. Measured integrated σ (σ_{obs}) for each galaxy in our OSIRIS sample, compared to predictions from the simulations, σ_{pred} (based on M_* and sSFR, Equation 2.1), color coded by galaxy stellar mass for sSFR averaged over 10 (top) and 100 (bottom) Myr. In both panels, the solid line represents $\sigma_{obs} = \sigma_{pred}$ with the shaded region showing 68% scatter of simulated galaxies around the best fit to $\log \sigma_{pred}$. The dashed line shows the best fit line measured from the data points. Our observations of σ agree best with the predicted velocity dispersion from the simulations using Equation 2.1, when sSFR is calculated over a 10 Myr timescale rather than a 100 Myr timescale. Over 100 Myr timescales, gas kinematics are affected by processes that act over dynamical timescales, whereas over 10 Myr timescales gas kinematics are affected by recent episodes of star formation.

2.5. Discussion

2.5.1. Rotational support at low mass. We preliminarily explore the relationship between smooth velocity gradients and galaxy stellar mass in search of a mass scale where stellar feedback is strong enough to overcome galaxy gravitational potentials and destroy disks. At higher masses we expect feedback to have a less dynamical effect due to deep potential wells.

Recent works show that at $z \sim 2$, high-mass galaxies ($\log(M_*/M_\odot) > 10.2$) are generally rotationally supported with primitive disks, while large fractions of lower mass galaxies are just beginning to form disks (Simons et al. 2016). We do not see any such trends within our current data set with galaxies across a wide stellar mass range showing velocity shears (as shown in Figure 2.3). Within the FIRE simulations, there are not generally disk-like structures in low-redshift

galaxies below $\log(M_*/M_\odot) \sim 10$. As noted in El-Badry et al. 2018a, the FIRE simulations may over-predict dispersion in low-mass galaxies at low redshift and thus skew predictions of rotational support to higher masses, although this trend has not been tested at the redshifts in this analysis. We require a larger sample, as well as a more complete kinematic analysis to give further insight on a mass scale at which feedback destroys disks in galaxies.

2.5.2. sSFR and Dispersion. If stellar feedback significantly alters the gravitational potentials of dwarf galaxies, we expect to observe a direct relationship between line-of-sight velocity dispersion and recent star formation (El-Badry et al. 2017). We indeed find a direct relationship between σ and sSFR: at fixed mass, higher sSFR correlates with higher σ , consistent with predicted values from simulated galaxies (Figure 2.5; Equation 2.1).

We examine this relationship over two relevant timescales, with sSFR averaged over 10 and 100 Myr. 10 Myr timescales trace the lifetime of massive stars, which are the main contributors to stellar feedback processes, whereas 100 Myr timescales cover dynamical timescales of galaxies, allowing the possibility for multiple starbursts episodes in addition to giving galaxies adequate time for their kinematics to respond to fluctuating gravitational potentials.

Our data exhibit a near equivalent correlation - 0.171 and 0.175 dex scatter - for sSFR averaged over both 10 and 100 Myr respectively, as shown in Table 2.3. The simulated data also appear to have similar scatter in fixed mass bins, as shown in Figure 2.4. This differs from the analysis in El-Badry et al. (2017), where they show a stronger correlation between *stellar* kinematics and sSFR when sSFR is averaged over 100 Myr as compared to sSFR averaged over 10 Myr. This disagreement may be due to the differences in analyses; this work evaluates the velocity dispersion of *gas* in ionized HII regions near young stars, contrasting the direct dispersion of all stars as measured in El-Badry et al. (2017). Completing our analysis with velocity dispersion calculated from all stars in the simulations yields a tighter correlation (smaller scatter), with SFR averaged over 100 Myr, consistent with El-Badry et al. (2017). The stronger correlation in σ of all stars with sSFR averaged over 100 Myr may be due to the dynamical time delay between rapidly fluctuating gravitational potentials and these fluctuations altering kinematics of stars. Gas kinematics may be affected on shorter dynamical timescales than stellar kinematics, as gas is affected by stellar feedback on short timescales whereas stellar kinematics are not.

Since our predicted σ s are affected by both sSFR and stellar mass (Equation 2.1), we are careful to verify that the observed trend in dispersion is not solely dependent upon mass. The correlation coefficient of the OLAS sample between M_* and integrated σ is 0.34, smaller than the correlation between the observed and predicted σ : 0.69 and 0.47 for sSFR averaged over 10 and 100 Myr, respectively. Thus, $\sigma(M_*, sSFR)$ vs σ is more strongly correlated than M_* vs σ , showing that the intrinsic relationship between M_* and σ is not the only contributor to the observed correlation of σ with sSFR. From this, we conclude that σ and sSFR are indeed correlated, and this observed relation is in good agreement with the FIRE simulations.

2.5.3. Implications for core formation. Simulations predict that core formation in dwarf galaxies may be driven by stellar feedback, provided that two conditions are met. First, feedback-driven mass loss rates must be dynamically significant. Second, multiple such strong feedback events must occur over a galaxy’s star formation history in order to eventually form a large central core. This study addresses the first condition, focusing on the effects of star formation feedback at a single epoch. To address core formation we must additionally consider dwarf galaxy star formation histories probed by complementary methods (e.g. Teyssier et al. 2013, El-Badry et al. 2016, Sparre et al. 2017). These results notably show bursty star formation histories oscillating over timescales on the order of ~ 100 Myr, with starbursts on the order of ~ 10 -100 Myr in cosmological simulations. As discussed in El-Badry et al. (2017), the power-law slopes of galaxy density profiles are predicted to be anti-correlated with sSFR and σ . In other words, cores and cusps oscillate in time with sSFR; periods of high sSFR and σ yield cusp-y density profiles, which flatten into cores following starburst episodes with strong gaseous outflows.

Of course it is not possible to measure reliable SFR histories for individual galaxies on the timescales relevant to verify these oscillations. A promising observational test of burstiness is to compare the SFR measured on different timescales, e.g. from $H\alpha$ and UV continuum, in large samples. Recently Emami et al. (2018) used this technique to study dwarf galaxies at $z=0$, finding galaxies with $M_* < 10^{7.5} M_\odot$ undergo strong bursts of star formation over shorter timescales ($t_{burst} < 30$ Myr), while more massive galaxies ($M_* > 10^{8.5} M_\odot$) experience longer, less powerful bursts, with $t_{burst} > 300$ Myr. These results support bursty star formation histories which appear

to be required for core formation. A similar study at $z \simeq 2$ would be of great interest in establishing the statistical properties of starburst timescales within the low-mass galaxy population. Differences between $H\alpha$ and UV-derived SFRs for the OLAS sample (Figure 2.1) indeed suggest that SFR fluctuates on < 100 Myr timescales, in our modest sample. However at present it remains an open question as to whether galaxies in fact undergo the number and frequency of repetitive star formation and feedback episodes needed to form cores, and over what timescales this transition may occur.

Our analysis shows that, using both fixed mass bins as well as a parameterized fit including stellar mass dependence, we observe the same trends in σ with sSFR as in cosmological simulations. However this is only one piece of the puzzle. We are careful to note that our analysis traces gas kinematics in dwarf galaxies, and not stellar kinematics. Gas kinematics of HII regions are affected by both feedback-induced outflows and the galaxy gravitational potential, unlike the kinematics of stars which are solely dependent upon the potential. The agreement of gas dispersion with sSFR is a precursor of the core formation process; if we did not observe this trend in the gas, it would be difficult to argue the trend would follow in the stars (and dark matter). While we cannot directly conclude stellar feedback resolves the cusp-core problem from these results, we can support that our observations of gas kinematics are in excellent agreement with predictions from simulations that do resolve the cusp-core problem with feedback. This initial observational test therefore paves the way for more stringent future kinematic studies such as dynamical mass modeling, and direct measurement of stellar kinematics with deep spectroscopy and/or future larger telescopes

2.6. Summary

The OSIRIS Lens-Amplified Survey (OLAS) is designed to address the role of stellar feedback in low mass galaxies at intermediate redshift. We introduced OLAS and presented the first results from the current sample of 17 galaxies. By using a combination of gravitational lensing and Keck AO, we provide a unique, spatially resolved kinematic sample of galaxies with low M_* and sSFR, pushing ~ 1.5 orders of magnitude lower in both quantities than other AO surveys (Figure 2.1), and explored tests of feedback driven core formation in low mass galaxies. Our main results are as follows:

- (1) We presented spatially resolved, image plane H α velocity maps (Figure 2.2) and preliminarily explored the relationship between rotational support (v/σ_{local}), ordered vs disordered kinematics, and stellar mass in comparison with recent literature (Simons et al., 2016, Figure 2.3). We used this relationship as a proxy for the strength of stellar feedback; i.e., to examine whether stellar feedback is strong enough to disrupt the overall gas kinematics of galaxies and destroy disks at these stellar mass scales. In this rudimentary classification scheme, we do not note any convincing trends that would signify a mass threshold for disruption of gaseous disks. We require a larger data set, in combination with a comprehensive dynamical analysis for kinematic classification, in order to search for a stellar mass scale where feedback destroys disks in galaxies as expected from theoretical arguments.
- (2) We tested the relationship between velocity dispersion and sSFR as predicted in El-Badry et al. (2017) from the FIRE simulations. While El-Badry et al. (2017) analyzed this relationship using stellar velocity dispersions, we studied star forming HII regions of the simulations to best mimic our observations. From the FIRE simulations we quantified line-of-sight σ as a function of M_* and sSFR, presenting the functional form (Equation 2.1) and its parameters (Table 2.3), finding no significant redshift dependence. Our results are consistent with predictions from simulations to within one standard deviation using sSFRs averaged over both 10 and 100 Myr. We confirm that galaxies with higher sSFR have higher σ at fixed mass, and the observed trend is in good agreement with that predicted by our analysis of theoretical simulations.
- (3) Simulations have predicted that core formation is driven by stellar feedback which alters the gravitational potentials, and thus the stellar kinematics and central dark matter density profiles. While we cannot make direct claims about the motions of stars with OLAS observations, this work uses the kinematics of ionized gas in star forming regions which are an appropriate tracer for stellar kinematics. We find that our observed gas kinematics are consistent with predictions from the FIRE simulations which do generate dark matter cores at these masses, suggesting that stellar feedback may indeed induce core formation in low mass galaxies as the simulations show. This agreement paves the way for further, more definitive, dynamical studies.

This work presents a new observational test of the origin of the cusp-core problem, one of the most important and outstanding challenges to the cold dark matter paradigm. Answering whether or not cores form through baryonic feedback processes can either validate or disprove the CDM hypothesis. This new approach is interesting because by extending our observations out to higher redshift (instead of restricting to the local universe), we probe the epoch in cosmic history where stellar feedback has the most dynamical effect. If we could not observe the predicted trend between σ and sSFR where feedback is predicted to have the strongest effect on galaxy kinematics, we would not expect feedback to be a catalyst for core formation.

We do find kinematic signatures of stellar feedback altering the kinematics of dwarf galaxies which are in good agreement with fully cosmological simulations that resolve the cusp-core problem with baryonic feedback. Future studies using JWST, TMT/IRIS and other thirty-meter class telescopes will allow us to observe galaxies with lower sSFRs, providing a wider dynamic range, as well as observe stellar kinematics, offering more direct tracers of galaxy gravitational potentials. These upcoming advances will further allow us to use stellar feedback in dwarf galaxies beyond the local group as a probe for studying dark matter core formation, helping us understand the major mass component of the universe.

Disentangling the Physical Origin of Emission Line Ratio Offsets at High Redshift With Spatially Resolved Spectroscopy

3.1. Introduction

Much of our knowledge of galaxy evolution across cosmic time is based on strong nebular emission lines at rest-frame optical wavelengths. Analysis of nebular line emission reveals properties of star formation and ionized gas including the total star formation rate (SFR), metallicity, gas density, and ionization parameter. Such studies have proven highly productive, with the advent of sensitive multiplexed spectrographs enabling comprehensive emission line studies at high redshifts (e.g., Kashino et al., 2019; Momcheva et al., 2016; Sanders et al., 2016b; Shapley et al., 2015; Steidel et al., 2014).

A key limitation of evolutionary studies is that some properties are typically not measured directly, in particular the gas metallicity (for which we will adopt the standard convention in terms of oxygen abundance: $12 + \log \text{O}/\text{H}$). Instead, nearly all studies at high redshift rely on calibrations of strong emission line ratios to estimate the galaxy metallicity (but see, e.g., Gburek et al. 2019; Patrício et al. 2018; Sanders et al. 2016a, 2020a for small $z > 1$ samples that have the direct metallicities based on electron temperature T_e). When applying these strong-line diagnostics, it is implicitly assumed that the high redshift samples have similar interstellar medium (ISM) physical conditions as star forming regions in nearby ($z \sim 0$) galaxies, which are used to calibrate these methods.

Large spectroscopic samples of $z > 1$ galaxies have revealed significant redshift evolution in the excitation sequences of strong emission line ratios. Most notably, it is now well-established that there is an offset in the “BPT diagram” of $[\text{O III}]/\text{H}\beta$ versus $[\text{N II}]/\text{H}\alpha$ (Baldwin et al., 1981) between $z > 1$ samples and the locus of $z \sim 0$ star-forming galaxies (e.g., Kashino et al., 2017; Shapley et al., 2015; Steidel et al., 2014). This BPT offset suggests an evolution in the underlying

physical properties governing emission line production, such as the shape of the ionizing spectrum, gas density, ionization parameter, and chemical abundance pattern (e.g., Kewley et al., 2013a). One consequence of changing ISM conditions is that the translation between strong-line ratios and metallicity will also evolve, such that applying locally calibrated diagnostics at high redshifts will yield systematically biased metallicity estimates (e.g., Bian et al., 2018; Patrício et al., 2018; Sanders et al., 2021b). This systematic error will directly affect inferences on galaxy formation and evolution based on the observed chemical evolution of galaxies (e.g., Lilly et al., 2013; Sanders et al., 2021b; Troncoso et al., 2014; Zahid et al., 2014).

Several hypotheses for the observed emission-line ratio offsets at high redshift have been suggested (e.g. Kewley et al. 2013a). These include emission mixing from low-luminosity active galactic nuclei (AGN; e.g., Wright et al. 2010) or shocked gas (e.g., Yuan et al. 2012), contributions from diffuse ionized gas (DIG; e.g., Zhang et al. 2016), an enhanced N/O abundance ratio (e.g., Masters et al. 2016, 2014; Shapley et al. 2015), high ionization parameter (e.g., Kewley et al. 2013b), and hard ionizing spectra driven by super-solar α /Fe abundance patterns (e.g., Sanders et al., 2020a; Shapley et al., 2019; Steidel et al., 2016; Topping et al., 2020a,b). To distinguish among these possibilities – and thereby recover accurate results with emission line studies – we require sensitive physical measurements beyond those typically available from the strongest nebular lines.

A critical step forward is the measurement of gas-phase metallicity and temperature using the “direct” T_e method based on auroral emission lines. In our earlier work, Jones et al. (2015) presented T_e -based abundance measurements for a sample of star forming galaxies at $z \sim 0.8$ drawn from the DEEP2 Galaxy Redshift Survey (DEEP2; Davis et al. 2003; Newman et al. 2013). Jones et al. (2015) found that the relations between direct metallicity and rest-optical line ratios of [O II], [O III], $H\beta$, and [Ne III] for the $z \sim 0.8$ sample are remarkably consistent with the sample of $z \sim 0$ galaxies from Izotov et al. (2006). While this comparison appeared to suggest no evolution in metallicity calibrations over $z = 0 - 0.8$, a key caveat is that the Izotov et al. (2006) sample comprises extreme local galaxies with high specific SFRs analogous to those of high-redshift galaxies due to selection effects, as noted by Sanders et al. (2020a, 2021b).

Comparison to a wider range of local galaxy properties is important for fully understanding the evolution of metallicity calibrations. Indeed, in comparing more representative samples of local

galaxies and H II regions to T_e -based samples at higher redshifts, Sanders et al. (2020a) found evidence that strong-line metallicity calibrations evolve between $z \sim 0$ and $z \sim 1.5 - 3.5$. By modeling the spectra of their $z \sim 2$ T_e sample, these authors found that the evolution of strong-line calibrations is due to a harder ionizing spectrum driven by α -enhancement of young, massive stars, in agreement with strong-line and rest-UV studies providing similar explanations for the $z \sim 2$ BPT diagram offset (Runco et al., 2021; Sanders et al., 2020b; Shapley et al., 2019; Steidel et al., 2016; Strom et al., 2018; Topping et al., 2020a,b). While these studies based on integrated galaxy spectra have yielded great progress in understanding the drivers of galaxy line ratio evolution, there remain potential contributors that cannot be easily identified in integrated measurements including DIG emission, weak AGN, and shocks.

This work is concerned with the spatially resolved analysis of a subset of galaxies studied by Jones et al. (2015) to further understand the ionizing sources that power nebular line emission in high- z galaxies. Here we use *Hubble Space Telescope* (HST) WFC3-IR grism spectroscopy covering the $H\alpha + [N \text{ II}]^1$, $[S \text{ II}]$, and $[S \text{ III}]$ emission lines for 15 galaxies at $\simeq 1$ kpc spatial resolution. Spatial mapping of these emission lines enables several key tests of the ionization mechanisms. In particular we seek to distinguish emission powered by star formation (i.e. H II regions), AGN, shocked gas and DIG. If AGN (particularly LINERs: low-ionization nuclear emission line regions) are present and responsible for BPT offsets, we expect to observe an elevated $[S \text{ II}]/(H\alpha + [N \text{ II}])$ ratio in the central ~ 1 kpc resolution element. Conversely if BPT offsets are due to shocked gas or DIG, we would expect elevated $[S \text{ II}]/(H\alpha + [N \text{ II}])$ in low surface brightness regions. Contributions from density-bounded H II regions with escaping ionizing radiation are expected to result in elevated $[S \text{ III}]/[S \text{ II}]$ ratios in the corresponding spatial regions. The diffraction-limited *HST* spectroscopic data presented herein therefore allow us to differentiate between these possibilities and discern the origin of redshift evolution in the BPT diagram. Understanding the cause of these line ratio offsets will allow us to better calibrate metallicity measurements between the low and high redshift universe.

This paper is structured as follows. In Section 3.2, we use spatially resolved spectroscopy of example galaxies at $z \sim 0$ to verify the methodology that we will apply to *HST*/WFC3-IR grism

¹ $H\alpha$ and $[N \text{ II}]\lambda\lambda 6548, 6584$ emission lines are blended at the spectral resolution of the WFC3-IR data; we refer to the sum of these lines as $H\alpha + [N \text{ II}]$. Likewise $[S \text{ II}]$ refers to the sum of the blended $[S \text{ II}]\lambda\lambda 6716, 6731$ lines.

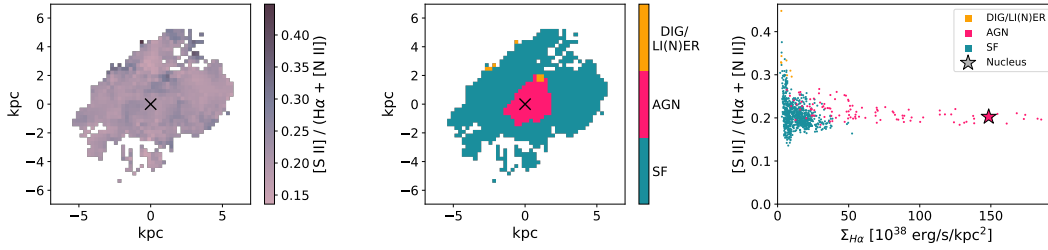
spectra. We describe our *HST* sample and data reduction methods in Section 3.3. In Section 3.4 we describe our analysis techniques and discuss one sample object in depth. In Sections 3.5 and 3.6 we analyze the various processes which can potentially power the observed emission lines. Finally, in Section 3.7, we summarize our results and discuss implications of this work for future research. Where necessary we assume a flat Λ CDM cosmology with $H_0 = 69.6 \text{ km s}^{-1} \text{ Mpc}^{-1}$, $\Omega_m = 0.286$, and $\Omega_\Lambda = 0.714$. All magnitudes are on the AB system.

3.2. Methodology: Distinguishing Ionization Sources

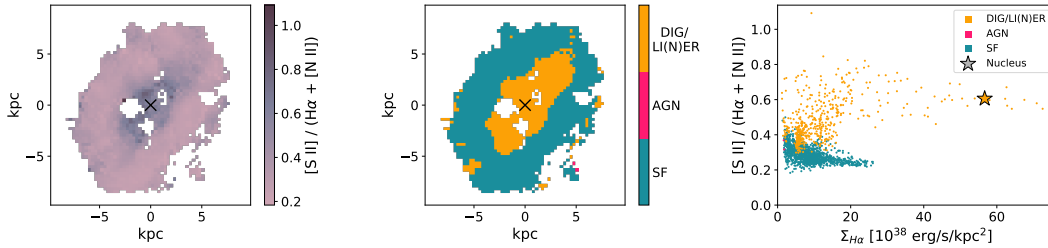
To establish our methodology, we first consider examples of different sources of emission line excitation observed in low-redshift galaxies from the SDSS-IV Mapping Nearby Galaxies at APO (MaNGA) survey (Bundy et al., 2015), which obtained optical integral field spectroscopy (IFS) at $\sim 1 \text{ kpc}$ resolution for $\sim 10,000$ low-redshift galaxies. In this section we use MaNGA IFS data to demonstrate how various ionization scenarios can be clearly distinguished using the diagnostics available with HST grism data. Our primary diagnostic is the line ratio $[\text{S II}]/(\text{H}\alpha + [\text{N II}])$, combined with the $\text{H}\alpha + [\text{N II}]$ surface brightness and spatial location within a galaxy.

We utilized the MaNGA catalogs and emission-line flux maps produced using the PIPE3D pipeline² (Sánchez et al., 2016a,b). For each galaxy, we selected all spaxels with $S/N \geq 3$ in $\text{H}\alpha$, $\text{H}\beta$, $[\text{O III}]\lambda 5007$, $[\text{N II}]\lambda 6584$, $[\text{S II}]\lambda 6716$, and $[\text{S II}]\lambda 6731$. We then calculated the line ratios $[\text{O III}]/\text{H}\beta$, $[\text{N II}]/\text{H}\alpha$, $[\text{S II}]/\text{H}\alpha$, and $[\text{S II}]/(\text{H}\alpha + [\text{N II}])$, noting that reddening correction is not required due to the close proximity of the wavelengths of the lines in each ratio. Following Belfiore et al. (2016), we classified spaxels as primarily ionized by star formation (SF), Seyfert-like AGN, or as low-ionization emission regions (LIERs), based on cuts in the $[\text{O III}]/\text{H}\beta$ vs. $[\text{S II}]/\text{H}\alpha$ diagram using the demarcations of Kewley et al. (2001, 2006). LIERs that are nuclear (e.g., LINERs) can be attributed to low-luminosity AGN, while LIERs that are extended throughout the disk are thought to originate from shocked gas and/or DIG emission (Belfiore et al., 2016). We furthermore computed the observed $\text{H}\alpha + [\text{N II}]$ luminosity surface brightness ($\Sigma_{\text{H}\alpha}$) using the $\text{H}\alpha + [\text{N II}]$ fluxes, spaxel sizes, and measured redshifts.

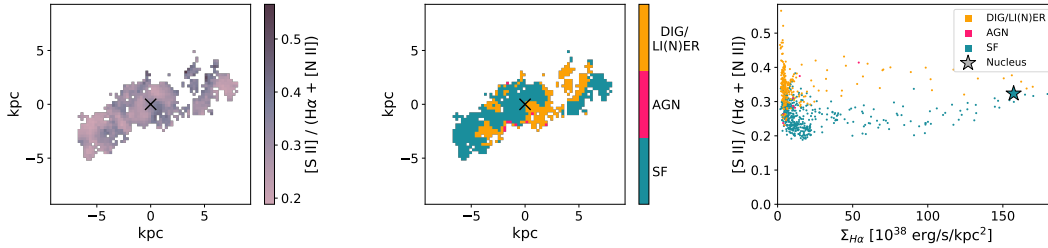
²Available online at <https://www.sdss.org/dr14/manga/manga-data/manga-pipe3d-value-added-catalog/>.



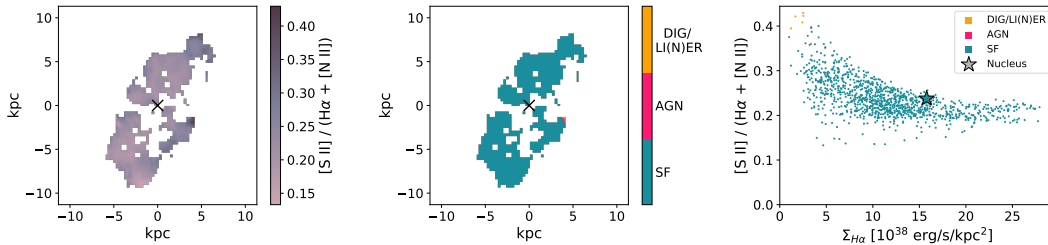
(a) MaNGA galaxy 10001-6102 with central region dominated by Seyfert type AGN emission. Since the AGN-dominated nucleus (pink) has the same range of $[S\ II]/(H\alpha+[N\ II])$ as the purely star formation spaxels (teal), we cannot use this diagnostic to discern between Seyfert AGN and star forming regions.



(b) MaNGA galaxy 8134-9102 with central region dominated by LINER type AGN emission. The spaxels separate into two clear populations, notably those categorized as LI(N)ER emission (orange) are found in the nuclear regions and have elevated levels of $[S\ II]/(H\alpha+[N\ II])$ across all surface brightnesses relative to the purely star forming regions (teal).



(c) MaNGA galaxy 8082-12702 with contributions from shocks and DIG. The spaxels categorized as DIG emission (orange) have elevated $[S\ II]/(H\alpha+[N\ II])$ relative to star forming regions (teal) and are concentrated in the lowest surface brightness regions.



(d) MaNGA galaxy 8085-12704 with emission lines dominated by star formation (teal) in all spatial regions. We see only one population in the rightmost panel, where the ratio of $[S\ II]/(H\alpha+[N\ II])$ remains consistently flat for all spaxels across all surface brightnesses.

FIGURE 3.1. Demonstration of the methods applied in this paper to distinguish emission line excitation from different sources. This figure shows examples of MaNGA galaxies showing a range of excitation mechanisms including regions dominated by (a) Seyfert AGN, (b) LINER type AGN, (c) shocks or DIG and (d) star formation. *Left panels:* Spatially resolved $[\text{S II}]/(\text{H}\alpha+[\text{N II}])$ maps. Black crosses denote galaxy nuclei. *Middle panels:* Spaxels color coded by dominant forms of emission following the demarcations of Kewley et al. (2001, 2006): DIG/LI(N)ER (orange), AGN (pink) and star formation (teal). *Right panels:* $[\text{S II}]/(\text{H}\alpha+[\text{N II}])$ plotted against $\text{H}\alpha+[\text{N II}]$ surface brightness, following the same dominant emission color codings. These galaxies show how different emission regions separate into clear populations when analyzed with this metric of spatially resolved $[\text{S II}]/(\text{H}\alpha+[\text{N II}])$, which we apply to HST grism data of $z \simeq 0.8$ galaxies in this work.

We produced maps of $[\text{S II}]/(\text{H}\alpha+[\text{N II}])$ and SF vs. LIER vs. AGN classification, as well as plots of $[\text{S II}]/(\text{H}\alpha+[\text{N II}])$ vs. $\Sigma_{\text{H}\alpha}$ (where $\Sigma_{\text{H}\alpha}$ represents the $\text{H}\alpha+[\text{N II}]$ surface brightness) for many MaNGA targets in order to evaluate how well these observables can distinguish between the various ionization mechanisms that we will use for our subsequent HST analysis. Illustrative examples of four MaNGA targets are shown in Figure 3.1. In each row, the left panel displays a map of the $[\text{S II}]/(\text{H}\alpha+[\text{N II}])$ ratio, the middle panel shows the ionization mechanism classification for each spaxel, and the right panel presents $[\text{S II}]/(\text{H}\alpha+[\text{N II}])$ as a function of $\Sigma_{\text{H}\alpha}$, with the properties of the central 1 kpc indicated by a star. For purposes of Figure 3.1, we adopt a single classification for shocks, DIG, LIER, and LINER (i.e., “DIG/LI(N)ER”) as these origins are not clearly distinguished by the emission line ratios alone. In our analysis herein we adopt the following conventions: concentrated nuclear LIER emission is considered a signature of *LINER AGN* (e.g., Figure 3.1b), while spatially extended low-surface brightness LIER emission is considered a signature of *shocks* and *DIG* (e.g., Figure 3.1c). In our analysis, we distinguish between LINER and DIG/LIER regions by their spatial distribution and $\text{H}\alpha+[\text{N II}]$ surface brightnesses: LINER emission is nuclear in origin and thus will be concentrated in the central regions of the galaxies, typically with higher $\text{H}\alpha+[\text{N II}]$ surface brightness whereas DIG/LIER regions are located throughout the disk and in galaxy outskirts, in regions with predominantly lower $\text{H}\alpha+[\text{N II}]$ surface brightnesses.

3.2.1. Weak AGN. A combination of AGN and star formation excitation can naturally explain the offsets in the BPT diagram observed at high redshift. This scenario can be distinguished

TABLE 3.1. Target Properties

Target ID	RA	Dec	Redshift	BPT offset ^a	Magnitude	H α Equivalent Width
				dex		Å
DEEP2-13016475	14:20:57.8616	+52:56:41.83	0.747	0.065	23.35 \pm 0.04	1516.8 \pm 93.7
DEEP2-13043682	14:20:08.3688	+53:06:37.57	0.761	0.097	22.31 \pm 0.02	240.4 \pm 26.6
DEEP2-13043716	14:19:48.0672	+53:05:12.62	0.781	0.111	21.11 \pm 0.02	305.4 \pm 15.7
DEEP2-14018918	14:21:45.4104	+53:23:52.71	0.770	0.070	22.97 \pm 0.03	618.8 \pm 39.2
DEEP2-21021292	16:46:35.3952	+34:50:27.80	0.763	-0.001 ^b	22.14 \pm 0.03	246.4 \pm 11.9
DEEP2-21027858	16:46:28.9848	+34:55:19.82	0.841	-0.115 ^b	22.83 \pm 0.05	886.3 \pm 51.8 ^c
DEEP2-22020856	16:51:31.4496	+34:53:15.82	0.796	0.092	23.02 \pm 0.04	438.5 \pm 31.3
DEEP2-22028402	16:51:31.9272	+34:55:29.28	0.797	0.076	20.28 \pm 0.02	325.0 \pm 4.9
DEEP2-22022835	16:50:34.5960	+34:52:52.09	0.843	0.001	23.50 \pm 0.05	1035.1 \pm 191.9 ^c
DEEP2-22032252	16:53:03.4608	+34:58:48.71	0.748	0.295	24.17 \pm 0.07	700.0 \pm 107.4
DEEP2-22044304	16:51:20.3232	+35:02:32.38	0.793	0.144	23.20 \pm 0.04	990.0 \pm 93.5
DEEP2-41059446	02:26:21.4913	+00:48:06.64	0.779	0.016	22.17 \pm 0.02	344.0 \pm 25.4
DEEP2-42045870	02:30:10.6027	+00:41:17.37	0.835	-0.030 ^b	21.94 \pm 0.02	396.6 \pm 40.0
DEEP2-31046514	23:27:07.5024	+00:17:41.18	0.790	0.058	22.85 \pm 0.03	529.9 \pm 43.7
DEEP2-31047144	23:26:55.4256	+00:17:52.60	0.855	0.182	22.90 \pm 0.03	848.5 \pm 44.9

^a BPT offsets are calculated as the minimum distance from the $z \sim 0$ star forming locus on the [O III]/H β versus [N II]/H α BPT diagram.

^b These targets fall beneath the star forming locus in [O III]/H β so we list their BPT offsets as negative.

^c These objects have negative [N II] best-fit fluxes, so their equivalent widths assume no contribution of [N II] to the blended H α + [N II] signal.

by spatially resolving the nuclear emission line ratios from those of surrounding star forming regions (as demonstrated by, e.g., Wright et al., 2010). Figures 3.1a and 3.1b show galaxies with Seyfert and LINER AGN, respectively, in the central regions. In both cases the galaxy outskirts show significant emission from star forming regions, leading to composite integrated spectra. As seen in the right-hand panel of Figure 3.1a, we cannot use [S II]/(H α + [N II]) as a diagnostic to distinguish Seyfert AGN from star forming H II regions, because the AGN-dominated nuclei and H II regions both have the same range of [S II]/(H α + [N II]) flux ratios. However we can see in Figure 3.1b that LINER-like low-luminosity AGN are clearly distinguished as having a much higher central [S II]/(H α + [N II]) ($\simeq 0.6$ in this case), compared to $\simeq 0.2$ – 0.3 for H II regions (teal spaxels). Therefore, we expect to observe regions with elevated [S II]/(H α + [N II]) in the centers of our target galaxies (likely with high surface brightness) if they have significant emission from LINER AGN.

The differences in [S II]/(H α + [N II]) result from LINERs having characteristically higher [S II]/H α ratios than Seyferts, though comparable [N II]/H α . Both types of AGN generally have high ratios

TABLE 3.2. Emission Line Measurements

Target ID	integrated $H\alpha+[N\ II]^a$	integrated $[S\ II]^a$	integrated $[S\ III]^a$	Keck $[N\ II]/H\alpha^b$	Keck $[O\ III]/H\beta^c$
	$10^{-16} \text{ erg/s/cm}^2$	$10^{-16} \text{ erg/s/cm}^2$	$10^{-16} \text{ erg/s/cm}^2$		
DEEP2-13016475	7.69 ± 0.16	0.68 ± 0.14	0.81 ± 0.09	0.019 ± 0.002	6.16 ± 0.06
DEEP2-13043682	3.90 ± 0.21	1.00 ± 0.17	0.49 ± 0.17	0.062 ± 0.008	4.64 ± 0.08
DEEP2-13043716	15.24 ± 0.29	1.78 ± 0.21	2.80 ± 0.29	0.147 ± 0.003	2.77 ± 0.05
DEEP2-14018918	4.38 ± 0.20	0.46 ± 0.17	0.53 ± 0.21	0.021 ± 0.006	6.19 ± 0.08
DEEP2-21021292	4.12 ± 0.20	0.71 ± 0.17	0.22 ± 0.18	0.055 ± 0.007	3.80 ± 0.07
DEEP2-21027858	4.96 ± 0.13	0.65 ± 0.11	0.72 ± 0.30	-0.027 ± 0.017^d	4.91 ± 0.11
DEEP2-22020856	3.30 ± 0.17	0.41 ± 0.15	0.27 ± 0.24	0.045 ± 0.006	5.20 ± 0.08
DEEP2-22028402	27.67 ± 0.31	3.68 ± 0.26	4.49 ± 0.35	0.147 ± 0.001	2.49 ± 0.03
DEEP2-22022835	2.57 ± 0.15	0.08 ± 0.13	0.70 ± 0.34	-0.003 ± 0.012^d	5.22 ± 0.12
DEEP2-22032252	2.22 ± 0.16	0.33 ± 0.14	0.18 ± 0.09	0.123 ± 0.023	5.37 ± 0.11
DEEP2-22044304	5.44 ± 0.17	0.85 ± 0.15	0.63 ± 0.25	0.054 ± 0.003	5.51 ± 0.04
DEEP2-41059446	4.74 ± 0.31	1.24 ± 0.28	1.40 ± 0.38	0.031 ± 0.006	4.90 ± 0.13
DEEP2-42045870	3.58 ± 0.25	0.82 ± 0.23	0.06 ± 0.47	0.036 ± 0.005	4.16 ± 0.07
DEEP2-31046514	4.03 ± 0.24	1.01 ± 0.22	0.55 ± 0.33	0.043 ± 0.014	4.85 ± 0.12
DEEP2-31047144	5.29 ± 0.15	0.56 ± 0.13	0.50 ± 0.58	0.046 ± 0.010	6.45 ± 0.13

^a Measured from HST WFC3-IR grism spectra.

^b $[N\ II]\lambda 6584/H\alpha$, measured from MOSFIRE or NIRSPEC spectra, as described in Section 3.3.2.

^c Measured from DEEP2 spectra as described in Jones et al. (2015). Here $[O\ III]$ refers to the $\lambda 5007$ line but is calculated as $2.98 \times$ the $[O\ III]\lambda 4959$ flux, as $[O\ III]\lambda 5007$ is redshifted beyond the spectral coverage in several targets.

^d These objects have negative $[N\ II]$ fluxes in their fits. Figures using these data show 2σ upper limits.

of $[N\ II]/H\alpha$ and $[S\ II]/H\alpha$ compared to H II regions. Although Seyfert AGN are not cleanly distinguished from H II regions using the $[S\ II]/(H\alpha+[N\ II])$ diagnostic, we note that other signatures such as X-ray luminosity and broad emission lines can be used to differentiate these sources.

3.2.2. Shocks and Diffuse Ionized Gas. As with LINER AGN activity, contributions from shocks or DIG can affect our observed emission line ratios. We can distinguish these effects via spatially resolved $[S\ II]/(H\alpha+[N\ II])$, where we expect elevated ratios to be localized just outside of the most luminous star forming regions and in galaxy outskirts in the case of shocks (e.g., Newman et al., 2012), or in regions of lower $H\alpha$ surface brightness in the case of DIG (e.g., Zhang et al., 2016).

The galaxy shown in Figure 3.1c shows widespread regions dominated by DIG/shocked gas emission. These DIG, shock, or LIER-dominated areas can be distinguished from star forming H II regions, by their signature of elevated $[S\ II]/(H\alpha+[N\ II])$ at relatively low $H\alpha+[N\ II]$ surface brightness $\Sigma_{H\alpha}$. Therefore, we expect to observe regions with elevated $[S\ II]/(H\alpha+[N\ II])$ in the

lowest surface brightness regions of our *HST* galaxies if their emission is dominated by shocked gas or DIG.

3.2.3. Escaping Ionizing Radiation. The observed BPT offsets of high redshift galaxies can also be explained in part by a higher fraction of density-bounded H II regions, which may be expected at the corresponding higher star formation surface densities (e.g., Alexandroff et al., 2015; Beckman et al., 2000). If ionizing radiation escapes from these regions and into the surrounding intergalactic medium, we expect elevated [S III]/[S II] ratios in and around the density-bounded regions (which are likely the highest surface brightness regions; e.g., Zastrow et al. 2011). For example, Zastrow et al. (2013) show the presence of optically thin “ionization cones” characterized by strong [S III] emission extended over kpc scales, which reveal significant escaping ionizing radiation. HST grism spectroscopy presented in this work provides coverage of [S III] at ~ 1 kpc resolution, although we generally do not detect the emission with high enough significance to search for such ionization cones, and thus we focus on other diagnostics. Nonetheless this approach may be of interest for galaxies with high confirmed or suspected ionizing escape fractions.

3.2.4. Star Formation. Finally, we consider the possibility that none of the above effects are significant, and that nebular emission in high-redshift galaxies is powered predominantly by star formation. In this case, offsets in the BPT diagram may be caused by different intrinsic properties of the massive stars and/or ionized gas in H II regions. If line emission in a galaxy is driven purely by star formation, we do not expect to see any extreme signatures with [S II]/($H\alpha + [N II]$) in relation to surface brightness or galactocentric radius. The relationship should remain a single population that is relatively flat with [S II]/($H\alpha + [N II]$) $\lesssim 0.3$, as seen in Figure 3.1d. Thus we do not expect to see strongly elevated [S II]/($H\alpha + [N II]$) at high or low surface brightnesses in our *HST* sample if their emission is uniformly dominated by star formation.

3.3. HST Sample Selection and Spectroscopy

Having established the utility of spatially resolved line ratio mapping with $z \sim 0$ galaxies, we will now apply the approach from Section 3.2 to HST grism spectroscopy at higher redshift ($z \sim 0.8$). Despite the larger cosmological distance, HST delivers ~ 1.0 kpc spatial resolution which is comparable to the low-redshift examples used to verify our methodology.

3.3.1. Sample. An overview of our HST sample is presented in Table 3.1. Our targets are a subset of the “ T_e sample” of 32 galaxies at $z \sim 0.8$ from Jones et al. (2015), which were originally drawn from the DEEP2 Galaxy Redshift Survey (DEEP2; Davis et al. 2003; Newman et al. 2013). The T_e sample was selected to be suitable for direct T_e -based metallicity measurements, and unbiased with regard to detection significance of the key temperature-sensitive [O III] λ 4363 emission line. In brief, the selection criteria from Jones et al. (2015) are: (1) coverage from at least [O II] $\lambda\lambda$ 3726,3729 to [O III] λ 4959 in the DEEP2 spectra; (2) no signs of nuclear activity in the DEEP2 spectra; (3) sensitive measurement of the line ratio $R_{[\text{O III}]}$ = [O III] λ 4363 / [O III] $\lambda\lambda$ 4959,5007 with $1\text{-}\sigma$ uncertainty ≤ 0.0025 . The last requirement ensures that [O III] λ 4363 is detected at $\geq 3\sigma$ significance for the median $R_{[\text{O III}]}$ ratio of the sample. The sample selection results in a bias toward high emission line luminosity and high excitation (e.g., large [O III]/ $H\beta$ ratios), relative to the star-forming populations at $z = 0.8$ and $z \simeq 0$ (see discussion in Section 2.3 of Jones et al., 2015). However, this selection is blind to the actual [O III] λ 4363 flux. Of the 32 galaxies in the parent T_e sample, [O III] λ 4363 is detected at a median significance of 5.3σ (with 6 galaxies having $< 3\sigma$ significance). The T_e sample galaxies have typical $M_* \simeq 10^{8.5} - 10^{9.5} M_\odot$ and span a narrow range of redshift $z = 0.72 - 0.86$.

3.3.2. Keck near-IR spectroscopy. We obtained followup near-infrared spectroscopy of 23 galaxies from the T_e sample in order to measure the $H\alpha$, [N II], and [S II] emission lines, using the Keck/NIRSPEC and Keck/MOSFIRE spectrographs (Jones et al. in prep), used to measure the BPT offsets of our sample. While weather conditions prevented us from securing near-IR spectra of all targets, the observed subset is representative of the T_e sample. Relative to the broader $z \simeq 0.8$ star forming galaxy population, this sample has large emission line equivalent widths and specific SFRs, relatively blue continuum colors, and luminosities representative of the overall sample observed by the DEEP2 survey (Jones et al., 2015). In brief, data were reduced using the LONGSLIT_REDUCE pipeline written by George Becker in the case of NIRSPEC, and the MOSFIRE Data Reduction Pipeline in the case of MOSFIRE. Both pipelines perform wavelength calibration, instrument signature removal, sky subtraction, and 1-D spectral extraction. MOSFIRE 1-D spectra were extracted using the BMEP program (Freeman et al., 2019) following the methods used in the MOSDEF survey (Kriek et al., 2015). Standard star observations taken on the same

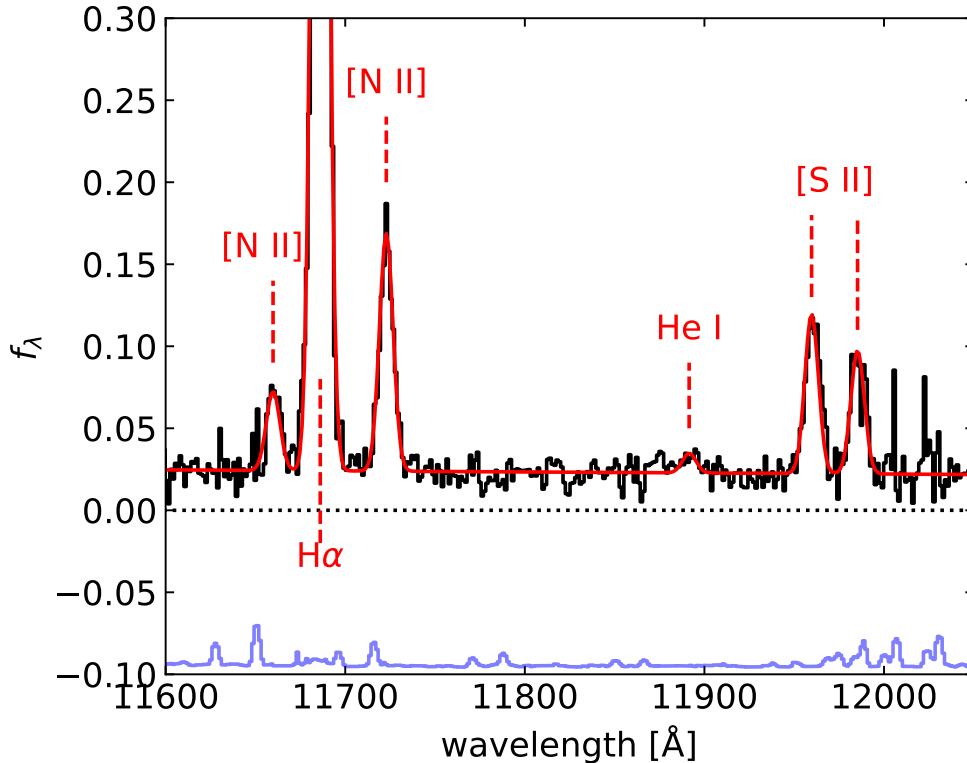


FIGURE 3.2. Near-IR Keck/MOSFIRE spectrum of DEEP2-13043716 at $z = 0.78$ showing the $H\alpha$, $[N II]$, and $[S II]$ emission lines. The reduced spectrum is shown in black, normalized to have peak $H\alpha$ flux density = 1. Gaussian fits to the strong emission lines are in red, and the $1\text{-}\sigma$ error spectrum is in blue (offset by -0.1). The $[N II]$ and $H\alpha$ lines, as well as the $[S II]$ doublet are spectrally resolved.

nights were used for telluric correction. Emission line fluxes were measured using single Gaussian fits (as in Jones et al., 2015). Figure 3.2 shows an example Keck/MOSFIRE spectrum and best-fit emission line profiles, with good spectral resolution of the $[N II]$ and $[S II]$ doublets. We selected the 15 galaxies with the largest $[S II]$ emission fluxes for HST grism spectroscopy, which forms the basis of this study. Availability of moderate resolution ground-based spectra is an important aspect, as this provides the $[N II]/H\alpha$ ratio for our targets (which is not available from HST grism spectra alone). Although the $[S II]$ flux selection may bias the HST subsample in terms of emission line ratios, we find that the 15 HST targets are representative of the parent sample in terms of location on the $[N II]$ BPT diagram. Figure 3.3 shows both the $[O III]/H\beta$ versus $[N II]/H\alpha$ and $[S II]/H\alpha$ BPT diagrams for the HST sample, color coded by their offset from the $[N II]$ BPT

diagram (hereafter referred to as “BPT offset”) with negative offsets lying below the typical $z \sim 0$ star forming locus. Each target’s BPT offset is calculated as the minimum distance from the $z \sim 0$ star forming locus on the $[\text{O III}]/\text{H}\beta$ versus $[\text{N II}]/\text{H}\alpha$ BPT diagram, with a median offset of ~ 0.08 dex. In both diagrams, our targets ($z \sim 0.8$) show a variety of offsets from where $z \sim 0$ H II regions typically lie. This work explores the cause of the $[\text{N II}]$ BPT offset by spatially mapping emission lines to distinguish between various potential mechanisms that may drive emission at high redshift.

3.3.3. HST observations and data reduction. The targets were observed using HST’s Wide Field Camera 3 (WFC3) via program GO-15077. Each target was observed for a single orbit, with 4 dithered G141 grism exposures plus 2 direct imaging exposures with the F140W filter, with a median exposure time of ~ 2100 seconds per target. Photometric magnitudes are calculated from direct images and we assume a systematic error floor of 0.02 magnitudes (see Table 3.1). We use the Grism Redshift and Line Analysis software (Grizli³; Brammer 2019) to reduce the HST slitless grism spectroscopy data. Grizli offers a complete data reduction pipeline, beginning with preprocessing both the raw direct image and grism exposures, forward modeling their entire field of view, fitting redshifts through a spectral template synthesis, extracting both 1D and 2D spectra (e.g. Figure 3.4), and outputting spatially resolved emission line maps and integrated emission line fluxes (given for our targets in Table 3.2). Of particular importance for this work is the level of contamination from overlapping spectra and zeroth-order images, which occurs with slitless grism data and can introduce errors in emission line measurements. In all cases the telescope orientation angle was constrained to avoid overlap of bright objects with our primary target spectra, and we additionally inspect the output spectra to check for contamination residuals. We do not find any cases where contamination significantly affects the primary target spectra which form the basis of this work.

In this paper we are mainly concerned with spatially resolved nebular emission line fluxes. Our analysis uses the $\text{H}\alpha + [\text{N II}]$ and $[\text{S II}]$ emission line maps directly from Grizli, where both the $\text{H}\alpha + [\text{N II}]$ lines and the $[\text{S II}]\lambda\lambda 6717, 6731$ doublet are blended due to the grism’s low spectral resolution. When both lines of the $[\text{S III}]\lambda\lambda 9068, 9531$ doublet are available, we use a weighted average of the doublet for our $[\text{S III}]$ measurement, using the fixed ratio of 2.44:1 between the

³<https://github.com/gbrammer/grizli>, version 0.8.0-4-g1153432

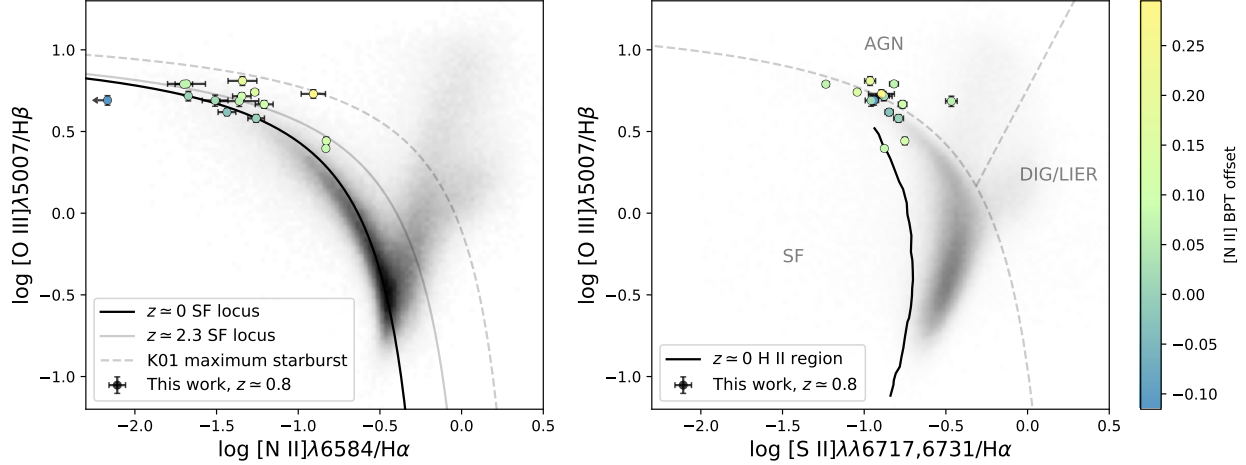


FIGURE 3.3. *Left*: [N II]-[O III] BPT diagram for our $z \sim 0.8$ sample, color coded by offset from the Kewley et al. (2013a) $z \sim 0$ star forming locus (solid black line), where negative offsets indicate the target falls below the star forming locus. Higher redshift galaxies are significantly offset from the $z \sim 0$ star forming locus in the [N II] BPT diagram, as demonstrated by an equivalent locus at $z \simeq 2.3$ from the MOSDEF Survey (solid gray line: Shapley et al., 2015). All of the HST targets lie below the maximum starburst line (Kewley et al., 2001, K01). The grayscale 2D density histograms in both panels show the same sample of $z \sim 0$ galaxies from SDSS (Abazajian et al., 2009). *Right*: [S II]-[O III] BPT diagram for the HST sample. Gray dashed lines show the separation into SF, AGN, and DIG/LIER regions at $z \sim 0$ following the demarcations of Kewley et al. (2001, 2006). The solid black line shows the median relation of local H II regions from Sanders et al. (2020b) based on observations from the CHAOS survey (Berg et al., 2015; Croxall et al., 2015, 2016). We note that the S20 line shows the median relation from pure H II regions (i.e., lacking any DIG emission) and is offset from the galaxy-integrated SDSS sample, which contains DIG contributions. The HST targets are also offset from the median $z = 0$ H II region sequence in the [S II]-[O III] BPT plane, falling along the typical locus of luminous compact star forming galaxies at $z \sim 0$.

stronger ($\lambda 9531$) and weaker ($\lambda 9068$) lines. When $[S III]\lambda 9531$ is redshifted out of the G141 grism wavelength coverage and thus cannot be detected, we use only the $[S III]\lambda 9068$ line multiplied by a factor of 2.44 (i.e. expressed as the expected intensity of the $\lambda 9531$ line). Figures 3.5 and 3.6 show examples of HST data products, showing direct images of the entire sample and spatially resolved emission line maps for one target (DEEP2-13043716), respectively. The pixel scale of the emission line maps is $0''1$, and the angular resolution is $0''13$ (full width at half-maximum). Emission line maps for the remainder of the sample can be found in Appendix C.

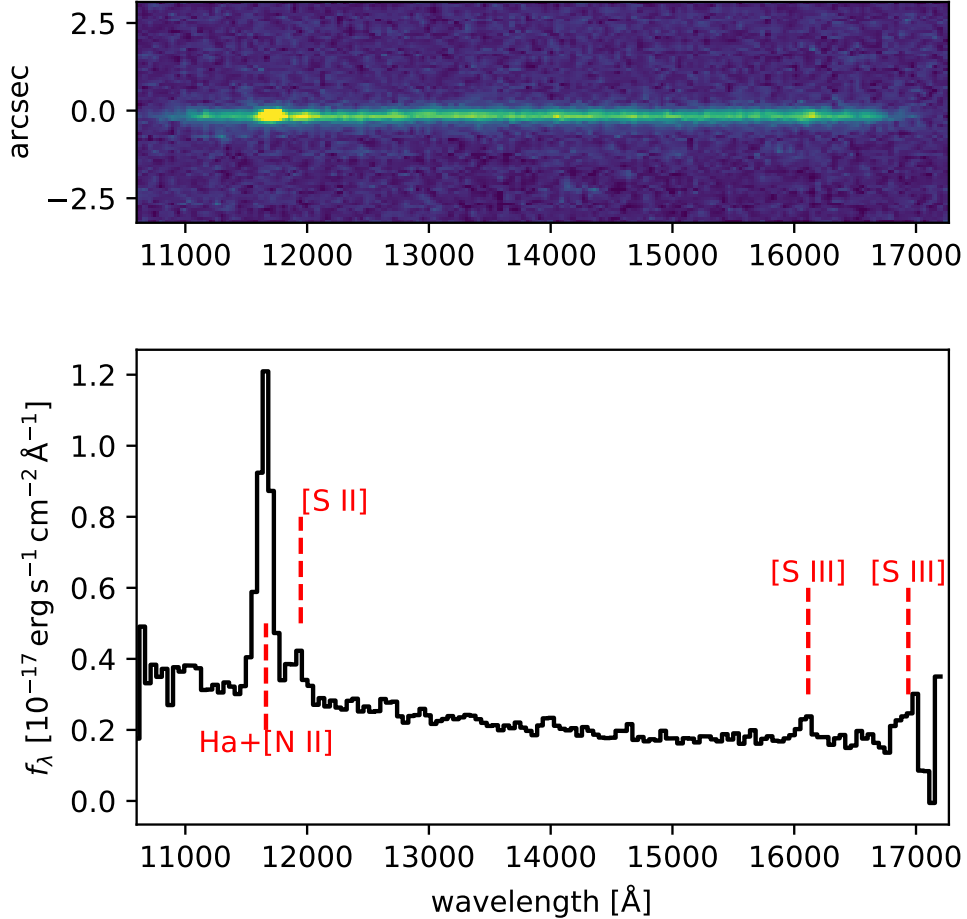


FIGURE 3.4. HST/WFC3-IR slitless grism spectrum of DEEP2-13043716 as processed by Grizli. *Top*: 2D galaxy spectrum. *Bottom*: Flux-calibrated 1D spectrum with our emission lines of interest highlighted: $\text{H}\alpha + [\text{N II}]$, $[\text{S II}]$, and the $[\text{S III}]$ doublet. Although $\text{H}\alpha + [\text{N II}]$ are blended in the HST grism spectra, as is the $[\text{S II}]$ doublet, these lines are clearly resolved in moderate resolution ground-based spectra available for all targets (e.g., Figure 3.2).

3.4. Analysis

This work utilizes the $\text{H}\alpha + [\text{N II}]$, $[\text{S II}]$, and $[\text{S III}]$ emission line maps output from Grizli to study spatially resolved emission line ratios. We are specifically interested in regions with elevated $[\text{S II}]/(\text{H}\alpha + [\text{N II}])$ or $[\text{S III}]/[\text{S II}]$, which are indicative of potential effects of weak AGN, shocks and DIG, or escaping ionizing radiation as demonstrated in Section 3.2. These effects can plausibly cause the observed deviation of high redshift galaxies from the $z \sim 0$ star forming locus in BPT diagrams.

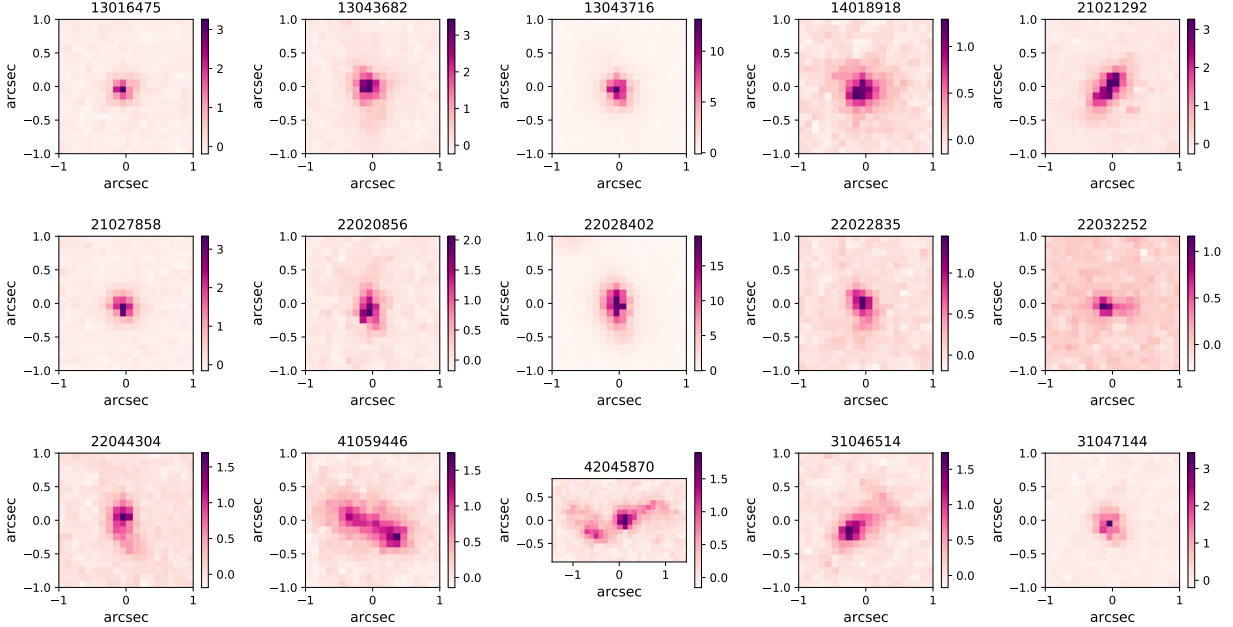


FIGURE 3.5. Direct HST F140W images for our HST sample. Nearly all targets have relatively compact morphologies, and even our most extended object, DEEP2-42045870, is free from $H\alpha + [N\ II]$ and $[S\ II]$ blending effects. Colorbars have units of 10^{-20} erg/s/cm²/Å.

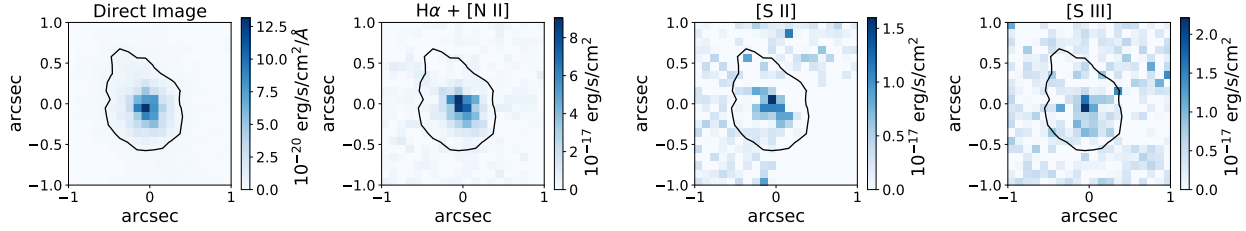


FIGURE 3.6. Raw Grizli emission line maps for DEEP2-13043716. From left to right: Direct image, $H\alpha + [N\ II]$, $[S\ II]$, and $[S\ III]$ emission line maps. The contours show the ~ 25.5 magnitudes/arcsec² flux cutoff for defining galaxy extent.

We define the spatial extent of each target from its F140W direct image by applying a surface brightness cutoff for each system of ~ 25.5 magnitudes/arcsec². This cutoff probes into the outer regions of our targets, including essentially all detected line emission while mitigating the amount of noise included from larger radii. This area corresponds to $\sim 20 - 140$ independent spatial resolution elements per target (median of 40), indicating our galaxies are resolved and we have the appropriate resolution to distinguish spatial structure and trends with surface brightness. The

targets are however sufficiently compact that there is no significant blending between the $\text{H}\alpha + [\text{N II}]$ and $[\text{S II}]$ lines (see Figures 3.4 and 3.5), such that we obtain clean maps of both over the same spatial regions.

To increase the signal-to-noise ratio (SNR) for spatially resolved analysis, we utilize two methods of binning our data before calculating the line ratios of interest, namely $[\text{S II}]/(\text{H}\alpha + [\text{N II}])$ and $[\text{S III}]/[\text{S II}]$. First we binned the data by $\text{H}\alpha + [\text{N II}]$ surface brightness in order to reach the lowest surface brightness regions that are not necessarily spatially contiguous. This is motivated by our objective to search for possible DIG or LIER emission (e.g., Figure 3.1c shows prominent DIG at low surface brightness regions scattered throughout the galaxy). Second, to examine spatially correlated regions, we use the Voronoi binning method of Cappellari & Copin (2003). Voronoi binning assigns spatially adjacent pixels to bins with a predetermined SNR requirement, and allows us to distinguish between the central and outer regions of galaxies more clearly. We required a median SNR threshold of 10 for $\text{H}\alpha + [\text{N II}]$ in each Voronoi bin.

Here we briefly discuss results for the galaxy DEEP2-13043716 demonstrated in Figures 3.7 and 3.8, as an example of what can be learned from the grism spectroscopy. This galaxy is offset by ~ 0.1 dex from the $z \sim 0$ star forming locus in the BPT diagram, slightly above the median offset in our sample (Table 3.1). The ratio $[\text{S II}]/(\text{H}\alpha + [\text{N II}]) \simeq 0.12$ is remarkably constant across an order of magnitude in surface brightness, thus ruling out LINER AGN, shocks and DIG as the dominant forms of emission on kpc scales. The $[\text{S III}]/[\text{S II}]$ ratio for this object is broadly constant with values ~ 1 – 2 , although the error bars are large for regions of lower surface brightness. However in our regions of interest (i.e., those with the highest surface brightness), the $[\text{S III}]/[\text{S II}]$ ratio remains flat and we can rule out a large contribution of density-bounded H II regions to the observed emission. The values are comparable to local high-excitation H II regions and $z \sim 1.5$ main sequence galaxies (e.g., Sanders et al., 2020b). In sum, this target lacks the clear distinguishing features in the line ratio maps which we would expect for LINER AGN, shocks, DIG, or escaping ionizing radiation, thus ruling out strong contributions from these sources. In contrast, this target exhibits relatively uniform $[\text{S II}]/(\text{H}\alpha + [\text{N II}])$ and $[\text{S III}]/[\text{S II}]$ ratios across all surface brightnesses which are consistent with that expected from excitation by newly-formed stars, suggesting that

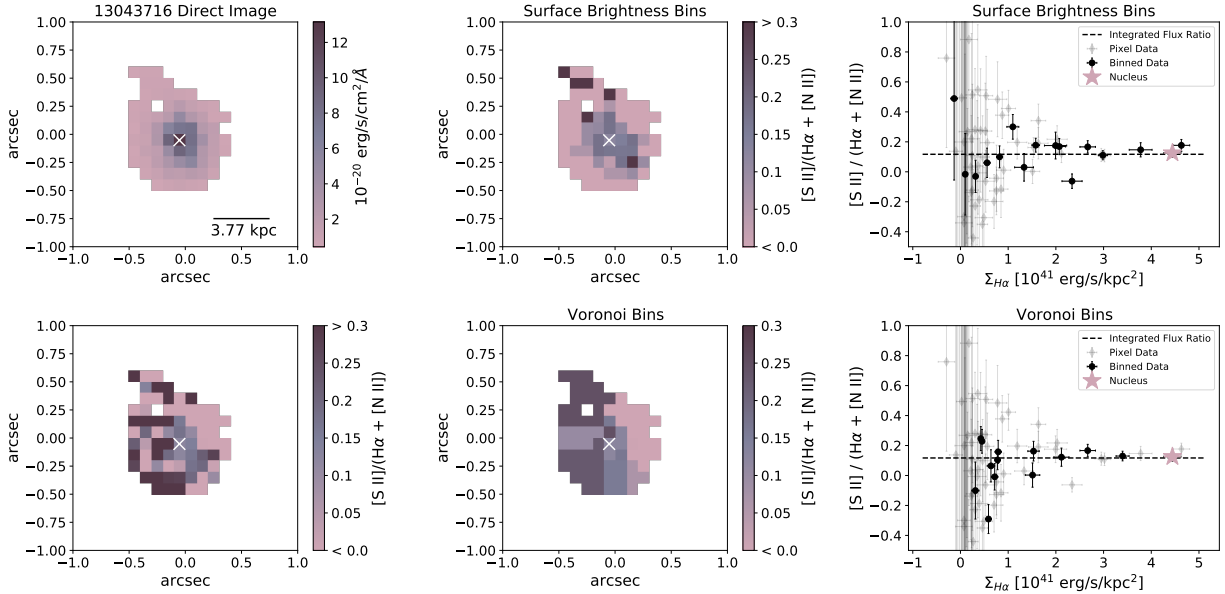


FIGURE 3.7. Spatially resolved $[\text{S II}]/(\text{H}\alpha + [\text{N II}])$ observations for DEEP2-13043716. *Top Left*: HST direct image (F140W). White crosses denote the nucleus, defined by the brightest central pixels in the direct image. *Bottom Left*: The ratio of $[\text{S II}]/(\text{H}\alpha + [\text{N II}])$ per pixel for this target. *Top Center*: $[\text{S II}]/(\text{H}\alpha + [\text{N II}])$ map binned by $\text{H}\alpha + [\text{N II}]$ surface brightness. The pixels in this panel are color coded by the mean $[\text{S II}]/(\text{H}\alpha + [\text{N II}])$ value in their $\text{H}\alpha + [\text{N II}]$ surface brightness bin; pixels in the same $\text{H}\alpha + [\text{N II}]$ surface bin are shown with the same $[\text{S II}]/(\text{H}\alpha + [\text{N II}])$ ratio. *Top Right*: Mean values of $[\text{S II}]/(\text{H}\alpha + [\text{N II}])$ in each surface brightness bin plotted against $\text{H}\alpha + [\text{N II}]$ surface brightness. *Bottom Center*: $[\text{S II}]/(\text{H}\alpha + [\text{N II}])$ map binned into Voronoi bins. Our approach here is to display the same pixels as the original map, with each pixel color coded by the mean $[\text{S II}]/(\text{H}\alpha + [\text{N II}])$ value in their respective Voronoi bin; pixels in the same Voronoi bin are shown with the same $[\text{S II}]/(\text{H}\alpha + [\text{N II}])$ ratio. *Bottom Right*: Mean values of $[\text{S II}]/(\text{H}\alpha + [\text{N II}])$ in each Voronoi bin plotted against $\text{H}\alpha + [\text{N II}]$ surface brightness. Gray points in the right-hand panels show individual pixel values. The black data points show the ratio in each surface brightness or Voronoi bin. Pink stars denote the galaxy nucleus. Black dashed lines show the integrated $[\text{S II}]/(\text{H}\alpha + [\text{N II}])$ ratio. Data points in the right-hand panels remain considerably flat with values $[\text{S II}]/(\text{H}\alpha + [\text{N II}]) \lesssim 0.2$, ruling out LINER AGN, shocks, or DIG as significant contributors to the observed emission.

star formation may be the primary driver of its emission lines in all well-detected spatial regions.

We perform a quantitative analysis for the remainder of our sample in Section 3.5.

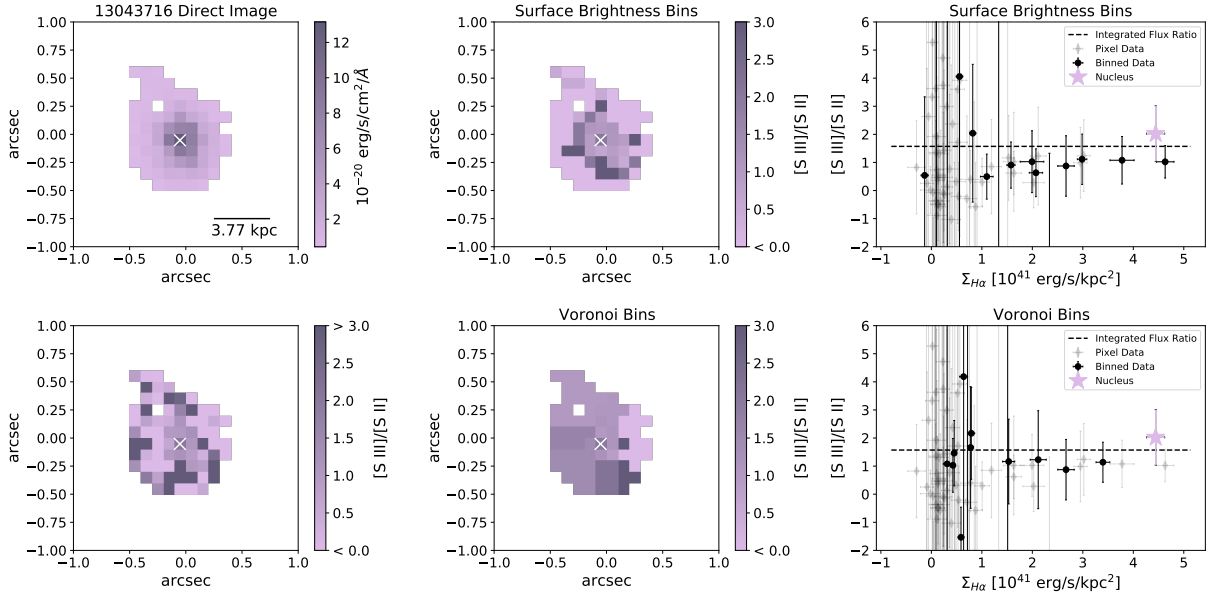


FIGURE 3.8. Spatially resolved $[\text{S III}]/[\text{S II}]$ observations for DEEP2-13043716. *Top Left*: HST direct image (F140W). White crosses denote the nucleus, defined by the brightest central pixels in the direct image. *Bottom Left*: The ratio of $[\text{S III}]/[\text{S II}]$ per pixel for this target. *Top Center*: $[\text{S III}]/[\text{S II}]$ map binned by $\text{H}\alpha + [\text{N II}]$ surface brightness. The pixels in this panel are color coded by the mean $[\text{S III}]/[\text{S II}]$ value in their $\text{H}\alpha + [\text{N II}]$ surface brightness bin; pixels in the same $\text{H}\alpha + [\text{N II}]$ surface bin are shown with the same $[\text{S III}]/[\text{S II}]$ ratio. *Top Right*: Mean values of $[\text{S III}]/[\text{S II}]$ in each surface brightness bin plotted against $\text{H}\alpha + [\text{N II}]$ surface brightness. *Bottom Middle*: $[\text{S III}]/[\text{S II}]$ map binned into Voronoi bins. Our approach here is to display the same pixels as the original map, with each pixel color coded by the mean $[\text{S III}]/[\text{S II}]$ value in their respective Voronoi bin; pixels in the same Voronoi bin are shown with the same $[\text{S III}]/[\text{S II}]$ ratio. *Bottom Right*: Mean values of $[\text{S III}]/[\text{S II}]$ in each Voronoi bin plotted against $\text{H}\alpha + [\text{N II}]$ surface brightness. Gray out points in the right-hand panels show individual pixel values. The black data points show the ratio in each surface brightness or Voronoi bin. Purple stars denote the galaxy nucleus. Black dashed lines show the integrated $[\text{S III}]/[\text{S II}]$ ratio. Data points in the right-hand panels remain considerably flat, and do not appear elevated in or near the brightest regions, ruling out density-bounded H II regions (with large ionizing radiation escape fractions) as a significant contributor to the observed emission.

3.5. Emission Line Powering Mechanisms

In this section we explore the possible sources of energy giving rise to the observed emission lines in our sample. Our approach here is to consider evidence for each emission mechanism based primarily on aggregate characteristics of the sample as a whole, as well as relevant individual objects

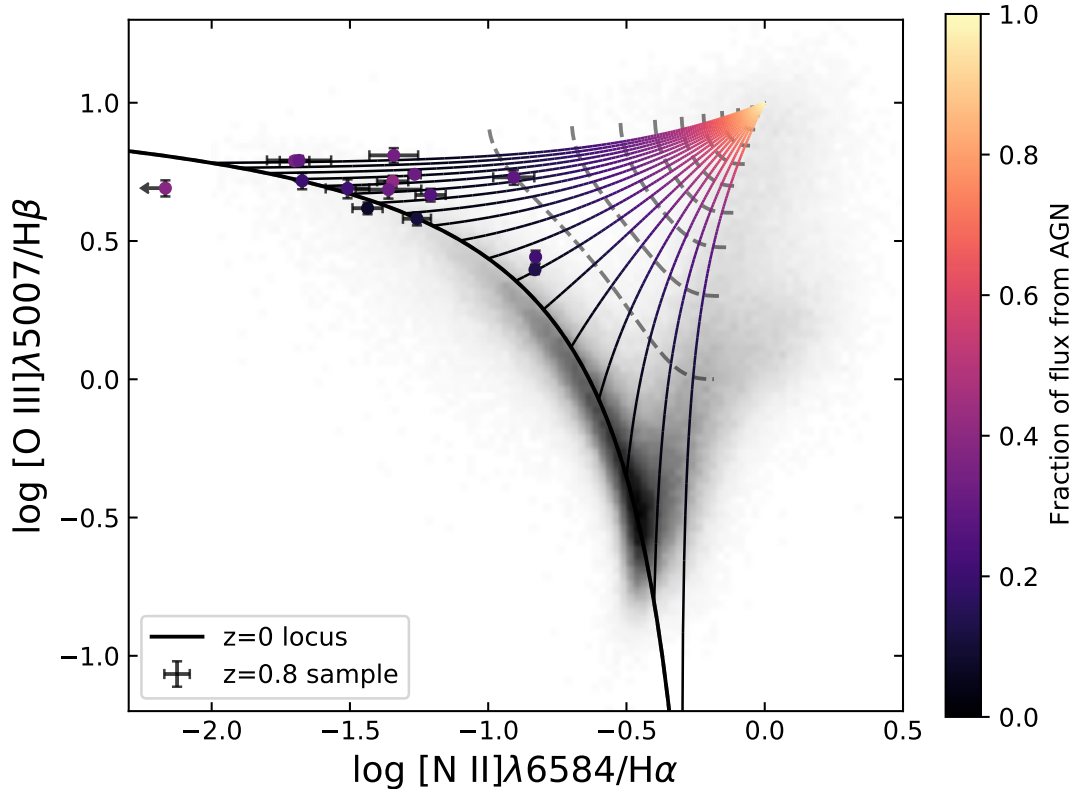


FIGURE 3.9. $[\text{N II}]$ -BPT diagram showing how flux contribution from a fiducial Seyfert AGN offsets galaxies from the star forming locus. Colored lines show the fraction of mixing from purely star forming to pure AGN. Dashed contours show fixed mixing fractions starting with 0% AGN fraction at the star forming locus, increasing in steps of 10% to 100% AGN contribution to the $\text{H}\alpha$ flux. We overlay our HST targets, noting that the observed offsets can be explained by at most 10% of the total flux coming from AGN. HST points are color coded by the percentage of $\text{H}\alpha$ flux in the central resolution element, ranging from 10-40%. To explain the observed BPT offsets, $\sim 25\%$ of the $\text{H}\alpha$ flux in the central resolution element would have to be attributed to AGN emission.

(Appendix C). We note that the general results of this section also hold if we consider only the subset of galaxies with largest offsets in the BPT diagram (e.g., > 0.1 dex offset from Table 3.1).

3.5.1. Weak AGN.

3.5.1.1. *Seyfert AGN.* As noted in Section 3.2, we cannot distinguish Seyfert AGN by looking at $[\text{S II}]/(\text{H}\alpha + [\text{N II}])$ levels because Seyfert AGN-dominated nuclei exhibit the same range of $[\text{S II}]/(\text{H}\alpha + [\text{N II}])$ values as the spaxels dominated purely by star formation (see Figure 3.1a). However, we can still explore whether these offsets are driven by significant Seyfert AGN activity

by estimating what percent of the flux must be attributed to AGN in order to cause the offsets observed in our HST sample.

Figure 3.9 shows how points along the Kewley et al. (2013a) $z \sim 0$ star forming locus would be offset when increasing fractions of the flux are from AGN, assuming 0% Seyfert AGN contribution along the star forming locus and 100% Seyfert AGN contribution at the tip of the AGN branch in the [N II] BPT diagram, assuming fiducial Seyfert line ratios of $\log([\text{N II}]/\text{H}\alpha)=0$ and $\log([\text{O III}]/\text{H}\beta)=1$ (e.g., Kewley et al., 2006). Using this metric, BPT offsets in our sample can be explained by a relatively small contribution of $\lesssim 10\%$ of their $\text{H}\alpha$ flux coming from AGN. The percentages of $\text{H}\alpha$ flux in the central resolution elements of our sample range from 10–40%. Therefore it is plausible that Seyfert AGN could be responsible for the observed offsets, if such emission represents a large fraction of flux from the central 1 kpc². If such AGN emission is common, we would expect to see signatures in IFS data that resolve the [N II]/ $\text{H}\alpha$ lines, or in X-ray or radio observations. We note that, given the luminosities of our sample, we would need relatively deep X-ray or radio data to determine if there is significant AGN emission. However, sensitive IFS surveys at similar redshift indicate low fractions of AGN activity at stellar masses of $\lesssim 10^{10} M_{\odot}$ and integrated [N II]/ $\text{H}\alpha < 0.2$ ratios of our sample (with AGN signatures in $< 10\%$ of galaxies, e.g., Förster Schreiber et al., 2019). Data with adaptive optics in particular can clearly distinguish elevated nuclear [N II] emission from AGN at the level required to explain offsets in our sample, but is rarely seen at these masses (e.g., Hirtenstein et al., 2019; Jones et al., 2013; Leethochawalit et al., 2016). Thus we view Seyfert AGN activity as an unlikely explanation for the BPT offsets.

3.5.1.2. *LINER AGN.* We can distinguish contributions from LINER type emission by looking for elevated $[\text{S II}]/(\text{H}\alpha + [\text{N II}])$ in the nuclear regions (as shown in Figure 3.1b). Figure 3.10 shows all data for the aggregate sample, where we can see that the nuclear and highest surface brightness regions are relatively flat with values $[\text{S II}]/(\text{H}\alpha + [\text{N II}]) \lesssim 0.2$, well below that expected for LINER emission. In order to explain the BPT offsets in our sample, LINER emission would have to account for $\sim 25\%$ of $\text{H}\alpha$ flux in the central resolution element as found for Seyfert AGN. For a fiducial mix of 75% star formation (with $[\text{S II}]/(\text{H}\alpha + [\text{N II}]) = 0.15$) and 25% AGN (with $[\text{S II}]/(\text{H}\alpha + [\text{N II}]) = 0.6$), we would expect a total $[\text{S II}]/(\text{H}\alpha + [\text{N II}]) \sim 0.26$ in the nucleus. This is clearly inconsistent with

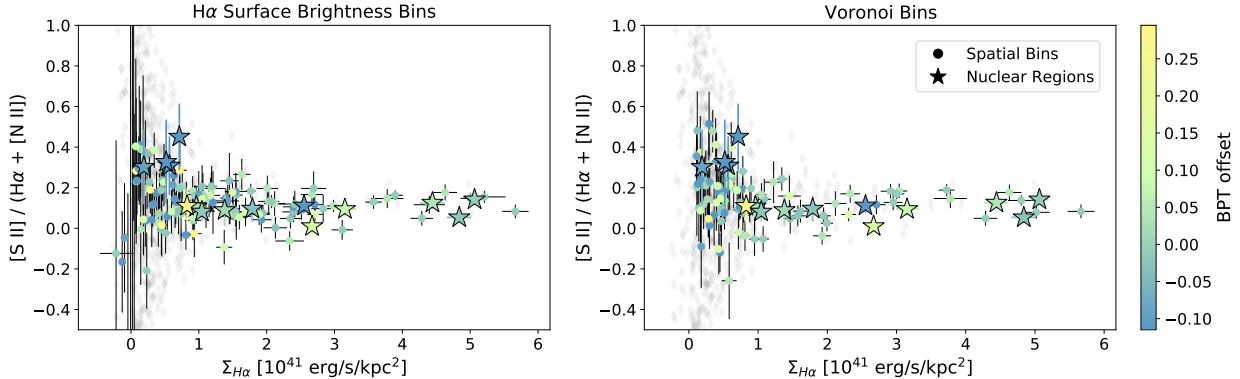


FIGURE 3.10. Our main diagnostic of spatially resolved $[S\ II]/(H\alpha + [N\ II])$ vs. $H\alpha + [N\ II]$ surface brightness, for the entire sample plotted together (individual galaxy breakdowns can be found in Figure 3.7 and Appendix C). Gray points represent individual pixel values, while colored circles represent spatial bins, and stars represent nuclear regions. Data points are color coded by the BPT offset of their respective galaxy. Both of our binning methods are represented here, binned by $H\alpha + [N\ II]$ surface brightness (left) and Voronoi bins (right). For both binning methods, the $[S\ II]/(H\alpha + [N\ II])$ remains flat in the highest surface brightness regions, indicating no overall trend of contribution from AGN. In comparison to the MaNGA galaxies shown in Figure 3.1, although the HST sample is binned over larger regions (typical bin areas of $\sim 2\text{ kpc}^2$), we are still able to distinguish between DIG and LINER emission on these scales in the MaNGA sample. The average $[S\ II]/(H\alpha + [N\ II])$ ratios in the HST sample are also lower than the MaNGA galaxies (even when restricting to their H II regions), which we attribute to a combination of higher excitation and lower metallicity in these $z \simeq 0.8$ HST targets

the majority of our sample, thus ruling out LINER emission as a dominant source even within the central resolution elements of our targets.

Within Figure 3.10 there are four individual targets which show elevated $[S\ II]/(H\alpha + [N\ II]) \gtrsim 0.3$ in their nuclear regions: DEEP2 IDs 21021292 (Figure C.4), 22022835 (Figure C.7), 41059446 (Figure C.11) and 42045870 (Figure C.12). Separate data for these galaxies is presented in Appendix C along with the rest of the sample. In three cases the elevated line ratios are not statistically significant ($\lesssim 1\sigma$) suggesting that the ratios are likely due to noise fluctuations rather than AGN. While these nuclear line ratios are indicative of LINER AGN activity, all four galaxies in question have negligible offsets from the $z \simeq 0$ BPT star forming locus: -0.001, 0.001, 0.016, and -0.03 dex, respectively (all consistent with zero offset).

We conclude that there is little evidence for LINER emission in the grism spectra, with only one object plausibly showing the expected LINER signature at $> 1\sigma$ significance. In particular there is

no sign of LINER activity among the galaxies exhibiting substantial offsets in the BPT diagram, despite sufficient angular resolution and sensitivity to detect the expected signal. Therefore, we can confidently rule out LINER-like line emission as the cause of BPT offsets in our sample.

3.5.2. Shocks and Diffuse Ionized Gas. To determine if shocks or DIG may contribute significantly to the emission properties of our sample, we next look for evidence of elevated $[\text{S II}]/(\text{H}\alpha + [\text{N II}])$ outside of the most luminous star forming regions in galaxy outskirts and in regions of low $\text{H}\alpha + [\text{N II}]$ surface brightness. Although shocked gas and DIG emission show similar signatures in our diagnostic, they have different effects on different emission lines and therefore on BPT diagram offsets. Shocks can cause an elevated $[\text{N II}]/\text{H}\alpha$ ratio, for example as observed in a lensed $z \simeq 1$ arc by Yuan et al. (2012). DIG-dominated regions are not likely to cause offsets on the $[\text{N II}]$ BPT diagram, but have a significant effect on the $[\text{S II}]$ flux and corresponding BPT diagram (e.g., Sanders et al., 2017). We note that while DIG may not be responsible for causing $[\text{N II}]$ BPT offsets, we still seek to quantify the role of DIG emission at moderate redshifts in our spatially resolved sample.

Looking at the entire sample in Appendix C, the $[\text{S II}]/(\text{H}\alpha + [\text{N II}])$ ratio appears flat in the lowest $\text{H}\alpha + [\text{N II}]$ surface brightness regions, to within the statistical uncertainties. While there are a few stray bins with higher $[\text{S II}]/(\text{H}\alpha + [\text{N II}])$ (\sim one bin per galaxy), the uncertainties with these data points are much higher and thus do not suggest significant contributions from shocks or DIG. The integrated data agree with the spatially resolved bins, showing offsets along the $z \sim 0$ SF/AGN dividing line, with no clear signs of offset towards typical shock/DIG emission regions (see Figure 3.3). While there is one galaxy more substantially offset towards the DIG/LIER region in $[\text{S II}]/\text{H}\alpha$, its $[\text{N II}]/\text{H}\alpha$ ratio does not show a significant BPT offset.

While we do not detect strong DIG or shocked gas emission in the individual galaxies, we look to the combined sample for bulk DIG emission across all targets. In Figure 3.11 we fit our observed aggregate sample $[\text{S II}]/(\text{H}\alpha + [\text{N II}])$ as a function of surface brightness (binning by $\text{H}\alpha + [\text{N II}]$ surface brightness for increased SNR at the lowest surface brightnesses) with DIG fractions from Oey et al. (2007). We assume a functional form

$$(3.1) \quad f_{DIG} = -1.50 \times 10^{-14} \times \Sigma_{H\alpha}^{1/3} + 0.748$$

as found by Sanders et al. (2017), treating the line ratios in SF and DIG regions as free parameters. We expect higher $[S\ II]/(H\alpha+[N\ II])$ at lower surface brightnesses due to increasing DIG fraction. Although the Sanders et al. (2017) fit parametrizes f_{DIG} as a function of $H\alpha$ surface brightness, using the blended $H\alpha+[N\ II]$ in this analysis should not strongly affect our results. We have verified that accounting for the contribution of $[N\ II]$ surface brightness, with a plausible range of $[N\ II]/H\alpha$ ratios in DIG-dominated and star forming regions, yields results consistent within our 1σ uncertainties.

Indeed, with this formalism we find evidence for the bulk effect of weak DIG emission at $\sim 2\sigma$ significance (Figure 3.11), with best-fit parameters of $[S\ II]/(H\alpha+[N\ II])= 0.29 \pm 0.09$ for pure DIG emission and $[S\ II]/(H\alpha+[N\ II])= 0.11 \pm 0.01$ for pure star forming regions. Using these best-fit values with the total $[S\ II]$ and $H\alpha+[N\ II]$ fluxes in all bins, we estimate the DIG fraction for our sample as a whole to be $\sim 22\%$. We note that the best-fit DIG line ratio of $[S\ II]/(H\alpha+[N\ II])$ for a pure DIG region is somewhat lower than expected based on nearby galaxies, although compatible given the uncertainty (Belfiore et al., 2016; Sanders et al., 2017; Zhang et al., 2016). If the true DIG line ratio is higher than given by this fit, then the DIG fraction of the sample would be lower than implied above (e.g., a typical DIG line ratio of 0.4–0.5 would imply only $f_{DIG} \sim 10\%$ for the sample). Considering this wide range of plausible DIG line ratios values, our estimated DIG fractions remain consistent with Sanders et al. (2017), who suggest that DIG contributes ~ 0 –20% of the total flux at these surface brightnesses. We conclude that while we do marginally detect weak DIG (at 2σ significance) or shocked gas emission in our sample, it is not a dominant source of emission in these targets and is not responsible for their offsets in the BPT diagram.

3.5.3. Escaping Ionizing Radiation. Galaxies showing signs of escaping ionizing radiation are expected to exhibit elevated levels of $[S\ III]/[S\ II]$ in or near the highest surface brightness regions (e.g., Alexandroff et al., 2015; Zastrow et al., 2013). Although our sample is not ideal for mapping $[S\ III]$ (with the stronger $\lambda 9531$ line redshifted beyond the G141 wavelength coverage in most cases), we consider the target with the strongest $[S\ III]$ signal in Figure 3.8. As discussed in Section 3.4 there is no significant evidence of elevated $[S\ III]/[S\ II]$ in the regions of interest. We do not have sufficient $[S\ III]$ detection for the remainder of the sample to comment further on whether escaping ionizing radiation may significantly affect the emergent nebular emission spectrum. However, the

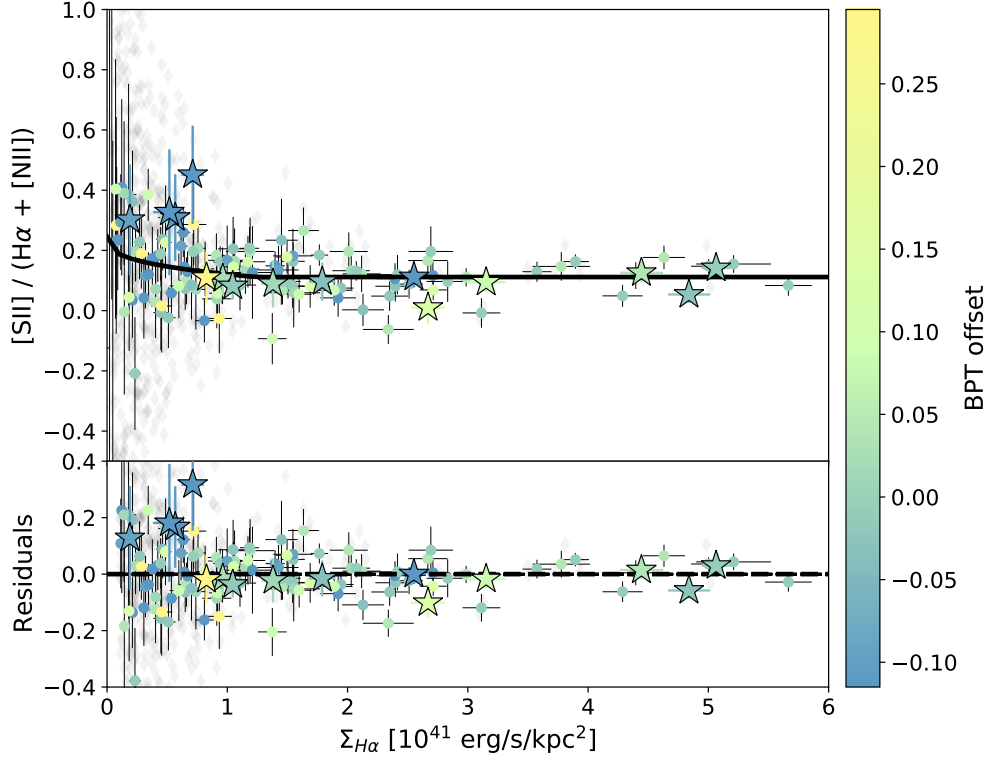


FIGURE 3.11. Our HST sample in aggregate (binned by $H\alpha + [N\ II]$ surface brightness) with the black line showing best-fit $[S\ II]/(H\alpha + [N\ II])$, using DIG fractions from Oey et al. (2007) (top panel). The higher $[S\ II]/(H\alpha + [N\ II])$ at low $\Sigma_{H\alpha}$ is due to contributions from DIG emission. The bottom panel shows residuals from this best-fit relation. We estimate the total DIG fraction in our sample to be $\sim 22\%$. The effect of bulk DIG emission at low surface brightnesses is marginally significant at the 2σ level. This DIG fraction, while consistent with measured DIG fractions at these surface brightnesses, is not large enough to cause the BPT offsets observed in our sample.

modest flux ratios of $[O\ III]/[O\ II] \lesssim 5$ (Jones et al., 2015) suggest low ionizing escape fractions (e.g., $f_{esc} < 0.1$ based on the results of Izotov et al., 2021).

While this study does not provide strong conclusions on the escape of ionizing radiation, we note that similar resolved mapping is possible at lower redshifts with HST’s grisms, and with future facilities including the James Webb Space Telescope (JWST) and Nancy Grace Roman Space Telescope. Such emission line maps may be a powerful diagnostic, especially given the challenges of confirming robust Lyman continuum emission with deep high-resolution imaging (e.g., Mostardi et al., 2015).

3.5.4. Star Formation. The spatially resolved line ratios in our sample, in addition to properties including morphology, color, and spectra (Jones et al. 2015) indicate that spatially extended star formation plays a large and likely dominant role in the nebular emission properties. While we have largely ruled out significant contributions from AGN, shocks and DIG, the HST grism spectra are in excellent agreement with excitation by star formation. The spatially resolved line ratios are broadly indicative of star forming H II regions with moderate metallicity (with median $12 + \log O/H = 8.2$ as indicated by direct measurements using the $[O III]\lambda 4363$ feature; Jones et al. 2015). The large surface brightness indicates a high star formation rate surface density (of order $1 M_{\odot}/\text{yr}/\text{kpc}^2$) which is typical of star-forming galaxies at $z > 1$. At such high surface brightness, DIG is expected to contribute minimally to the total line fluxes ($\lesssim 20\%$; Oey et al. 2007; Sanders et al. 2017; Shapley et al. 2019), consistent with the weak DIG emission signatures from Section 3.5.2.

This conclusion remains consistent with other resolved line ratio work targeting H II regions at high redshift. For example, Jones et al. (2013) and Leethochawalit et al. (2016) conclude that emission lines originate predominantly from star forming H II regions in their lensed samples of galaxies at $z \sim 2$, and that their observed offsets are broadly consistent with extensions of the star-forming locus seen in other high redshift surveys (e.g., Shapley et al., 2015; Steidel et al., 2014). Similarly, Genzel et al. (2014) and Förster Schreiber et al. (2019) find AGN to be uncommon in galaxies at similar masses at $z \simeq 1 - 2$, namely less than 10% for galaxies with $\log(M_{*}/M_{\odot}) < 10.3$. Furthermore, star formation rates derived from $H\alpha$ and $H\beta$ emission lines are in good agreement with results from other methods in $z > 1$ galaxies (Shivaei et al., 2016), supporting star formation as the dominant source of nebular line flux. Our spatially resolved analysis both strengthens the evidence that our sample is dominated by star formation, and provides stringent limits on the fraction of line flux which can be attributed to other ionization mechanisms.

3.6. Emission line excitation from star forming regions at high redshift

Analysis of our sample described in Section 3.5 strongly suggests that the dominant source of line emission in all cases is from H II regions powered by star formation. Here we discuss the implied

star formation properties of our sample and consider which physical properties of H II regions might be responsible for offsets in the BPT diagram compared to $z \sim 0$ galaxies.

The surface brightness of our sample spans $\Sigma_{H\alpha} \sim 0.5\text{--}5 \times 10^{41} \text{ erg s}^{-1} \text{ kpc}^{-2}$ for well-detected regions, with total luminosities $L_{H\alpha} \sim 10^{42} \text{ erg s}^{-1}$ (uncorrected for extinction; two objects have significantly larger luminosities). The emission is extended over several kpc in all cases with at most $\sim 40\%$ of the flux being found within a single resolution element. Accounting for $\sim 1\text{--}2$ magnitudes of extinction (based on Balmer lines; Jones et al. 2015), this corresponds roughly to SFR densities $\Sigma_{\text{SFR}} \sim 1\text{--}10 \text{ M}_{\odot} \text{ yr}^{-1} \text{ kpc}^{-2}$ and total SFR $\sim 10\text{--}50 \text{ M}_{\odot} \text{ yr}^{-1}$ (assuming a Chabrier 2003 initial mass function). These values are characteristic of moderately massive ($M_{*} \sim 10^9 \text{ M}_{\odot}$) star forming galaxies at $z > 1$ (Shivaei et al., 2015; Speagle et al., 2014).

Line ratios and positions in the BPT diagram are known to vary systematically with total emission line luminosity and surface brightness. At the relatively low luminosities (or equivalently SFRs) typical of spatially resolved $z \sim 0$ spiral galaxies, lower $\Sigma_{H\alpha}$ correlates with offsets toward higher $[\text{N II}]/\text{H}\alpha$, $[\text{S II}]/\text{H}\alpha$, and $[\text{O III}]/\text{H}\beta$ which can be explained by increasing fractions of DIG (e.g., Masters et al. 2016; Oey et al. 2007; Sanders et al. 2017; Shapley et al. 2019; Zhang et al. 2016). In contrast, the global trend is opposite, where *higher* integrated $L_{H\alpha}$ correlates with offsets toward higher $[\text{N II}]/\text{H}\alpha$ and/or $[\text{O III}]/\text{H}\beta$ as seen in the BPT diagram for both $z \sim 0$ and $z > 1$ galaxies (e.g., Brinchmann et al., 2008; Cowie et al., 2016; Masters et al., 2016). Our sample is clearly characteristic of the latter case, having luminosities typical of the $z > 1$ galaxies analyzed by Cowie et al. (2016). While our sample is not large enough to establish an explicit relationship in BPT offset with luminosity, we can nonetheless explore whether the observed BPT offsets of the HST targets follow the same trends as found in larger populations. The luminosity of our sample (typical $L_{H\beta} \sim 10^{41.5} \text{ erg s}^{-1}$) corresponds to offsets in $[\text{N II}]/\text{H}\alpha$ and $[\text{O III}]/\text{H}\beta$ of $\sim 0.1\text{--}0.2$ dex according to Cowie et al. (2016). This is in good agreement with the median offsets solely in $[\text{N II}]/\text{H}\alpha$ or $[\text{O III}]/\text{H}\beta$ (0.19 and 0.7 dex, respectively) in our sample. Thus the BPT offsets in Table 3.1 are commensurate with trends in global properties seen at both low and high redshifts. As such, the physical mechanisms responsible for offsets in this sample are likely to be the same as in broader galaxy populations.

Many other works have further explored the main driving mechanisms of the more extreme ISM conditions at $z > 0$. Such studies have invoked a variety of properties at high redshift such as H II regions having higher ionization parameters than at $z \sim 0$ (e.g., Kewley et al. 2013a,b), an enhanced N/O abundance (e.g., Masters et al. 2014; Shapley et al. 2015), and high α /Fe abundance ratios (e.g., Sanders et al. 2020a, 2021b; Shapley et al. 2019; Steidel et al. 2016). A key result of our spatially resolved analysis is that the emission line ratios appear nearly constant across individual galaxies. That is, offsets in the BPT diagram appear linked to physical conditions in the H II regions. Given the limited number of emission lines in HST grism data, we cannot clearly distinguish between various mechanisms proposed in the literature on spatially resolved scales. However, the results of this work support treating the integrated emission line fluxes of high- z galaxies as originating from H II regions ionized by massive stars, for purposes of modeling and interpreting their spectra. As an example, the photoionization modeling framework from Sanders et al. (2021b) – adopting the T_e -based O/H measurements for our sample (Jones et al., 2015) – indicates that the BPT offsets in our sample are caused by super-solar O/Fe abundances. In our future work, we will apply a rigorous photoionization modeling analysis of this sample using stellar population synthesis models as input (e.g. BPASS).

Increased O/Fe abundances are generally expected for galaxies at high redshifts, given the shorter enrichment timescale for α -elements such as O compared to Fe. Recent work has suggested that O/Fe may typically reach $\sim 4\times$ the solar value at $z \sim 2$ (e.g., Jones et al., 2018; Sanders et al., 2021b; Steidel et al., 2016; Topping et al., 2020a). Such α -enhancement results in harder stellar ionizing spectra at fixed O/H abundance, which drives offsets in the BPT diagram. While we cannot measure O/Fe directly in our sample, we expect it to correlate with young ages and hence high specific star formation rates (sSFR). Figure 3.12 explores this idea, using H α equivalent width (EW) as a proxy for sSFR (and hence possibly α -enhancement). To correct for the dependence of H α EW along the $z \sim 0$ BPT locus, we first fit for a relationship between mean H α EW of the $z \sim 0$ sample and the parameter O3N2 ($= \log([\text{O III}]/\text{H}\beta) - \log([\text{N II}]/\text{H}\alpha)$), using the rest frame H α EW. We note that lines of constant O3N2 are roughly orthogonal to the BPT star-forming sequence in the region of interest here, such that normalization at fixed O3N2 is appropriate for

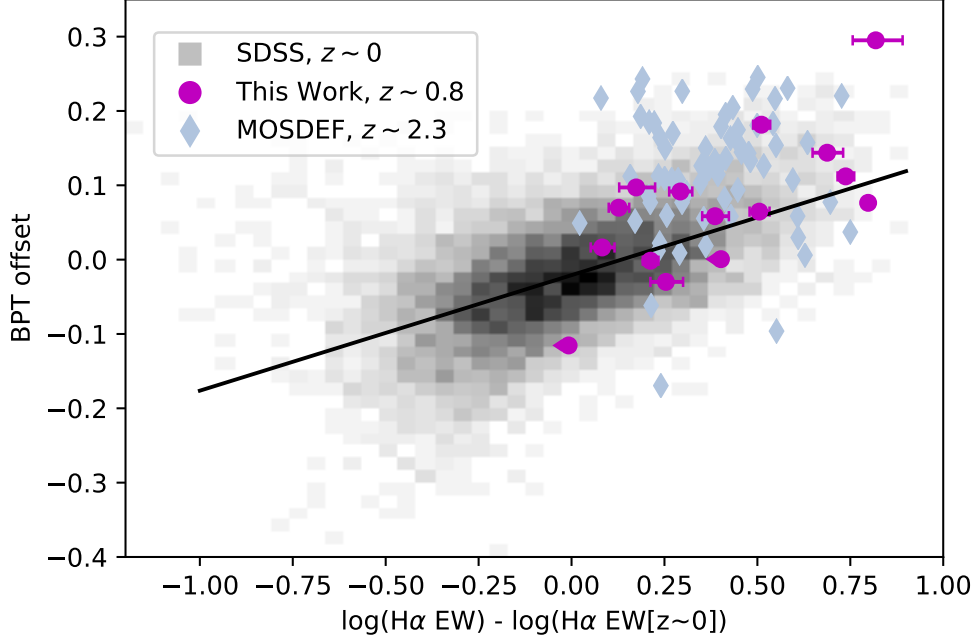


FIGURE 3.12. BPT offset plotted against normalized $H\alpha$ equivalent width for star forming galaxies at $z \sim 0$ (SDSS), our HST sample at $z \sim 0.8$, and $z \sim 2.3$ (MOSDEF, Reddy et al. 2018; Sanders et al. 2018). The solid black line shows the best fit to the SDSS data. We see a clear trend in the SDSS data of BPT offset with normalized $H\alpha$ equivalent width. The high redshift sources are, on average, offset above the best fit line at fixed equivalent width, consistent with expectations for increased α -enhancement at earlier cosmic times. $H\alpha$ equivalent width is chosen here as a proxy for sSFR, which correlates with age. This is interesting to consider in the context of chemical abundance patterns, in particular super-solar α/Fe at young ages. The correlation seen here indicates that larger BPT offsets are indeed associated with younger ages (higher sSFR and equivalent width), consistent with the trend expected if α -enhancement is responsible for the observed BPT offsets in our sample.

comparison with our BPT offset measurements. We find a linear relationship of

$$(3.2) \quad \log(H\alpha \text{ EW}[z \sim 0]) = 0.762 + 0.779 \times \text{O3N2}$$

(with $H\alpha$ EW measured in \AA) to be a good fit for star-forming galaxies in SDSS, spanning the $\text{O3N2} > 1.2$ values of our sample.

Figure 3.12 plots the normalized $H\alpha$ EW (using the mean relationship in Equation 3.2) at fixed O3N2 , revealing a clear correlation between normalized $H\alpha$ EW and offsets in the BPT diagram for the SDSS sample (as has been noted previously by, e.g., Brinchmann et al., 2008). Moreover,

the higher redshift data – shown for both our HST sample at $z \sim 0.8$ and MOSDEF galaxies at $z \sim 2.3$ (Reddy et al., 2018; Sanders et al., 2018) – show increased BPT offsets at fixed EW. The median displacement above the SDSS best fit line appears to increase with redshift (0.02 dex for the HST sample, 0.08 dex for the MOSDEF sample), although there is no clear correlation within the MOSDEF sample. This suggests a smooth evolution of increased BPT offset with increasing redshift at fixed H α EW beyond the relation at $z \sim 0$ (consistent with the expectation of increasing α enhancement at high redshifts compared to $z \sim 0$).

While our analysis supports α -enhanced abundance patterns, we note that this is indistinguishable from the case where ISM metallicity is higher than that of ionizing stars, with solar abundance patterns. Recent ISM enrichment from massive stars may show significant deviations from the mean galaxy metallicity and be localized to $\lesssim 1$ kpc spatial scales (Krumholz & Ting, 2018). While the stars responsible for ionizing H II regions are generally thought to have similar composition as the ISM, our data do not provide direct measurements of the stellar abundance. We also note that Topping et al. (2020a) suggest α -enhancement even among $z \sim 2$ galaxies which are not offset from the $z \sim 0$ BPT locus, such that additional properties beyond abundance patterns must play a significant role.

We note that there are many other possibilities that may drive BPT offsets beyond abundances. In particular, effects of binary stellar evolution (leading to stripped stars or high-mass X-ray binaries), turbulence (e.g., Gray & Scannapieco, 2017), and higher ionization parameters (e.g., Jaskot et al., 2019) may also drive high redshift galaxies off of the $z \sim 0$ star forming locus. Nonetheless, our results are generally consistent with offsets driven by moderate α -enhancement, if indeed the H α EW correlates with young ages and α -enhanced abundance patterns. We conclude that photo-ionization modeling of H II regions ionized by massive stars will be a reasonable tool for further interpreting these results since there are no significant signatures from other ionizing sources beyond star formation.

3.7. Summary

In this paper we present and analyze spatially resolved emission line maps of 15 galaxies at $z \sim 0.8$ in the DEEP2 fields, observed with HST grism spectroscopy. Our targets show moderate

offsets from the $z \sim 0$ locus of star forming galaxies on the $[\text{O III}]/\text{H}\beta$ versus $[\text{N II}]/\text{H}\alpha$ BPT diagram, comparable to those seen in typical $z \sim 2$ galaxies. While line emission in the sample appears to be dominated by star formation, we analyzed $\text{H}\alpha+[\text{N II}]$, $[\text{S II}]$ and $[\text{S III}]$ maps in order to distinguish signatures of AGN, shocks/DIG, or escaping ionizing radiation in our sample to determine whether these mechanisms may be responsible for the observed BPT diagram offsets. Our main results are as follows:

- (1) *AGN*: We achieve ~ 1 kpc spatial resolution to distinguish possible contributions from faint AGN. We find that AGN would need to account for a large fraction of emission ($\gtrsim 25\%$ of $\text{H}\alpha$ flux) within the central resolution element, in order to explain the observed magnitude of BPT offsets. In the case of LINER AGN, we would expect significantly elevated $[\text{S II}]/(\text{H}\alpha+[\text{N II}])$ ratios in the nuclear regions, which are not observed. In particular the objects in our sample with the largest BPT offsets are inconsistent with significant emission from LINER AGN. For Seyfert AGN, the $[\text{S II}]/(\text{H}\alpha+[\text{N II}])$ ratio is not necessarily different from that of H II regions, and so we cannot clearly distinguish their presence in the sample. However if Seyfert AGN emission is indeed widespread, it would be easily distinguishable in IFS surveys via high $[\text{N II}]/\text{H}\alpha$ ratios in galaxy nuclei, which are not commonly observed in galaxies with mass and metallicity comparable to this sample. We therefore conclude that substantial Seyfert AGN contributions are unlikely, and LINER AGN are clearly ruled out as causes of BPT offsets.
- (2) *Shocks and DIG*: We examine how $[\text{S II}]/(\text{H}\alpha+[\text{N II}])$ varies spatially and as a function of surface brightness, in order to distinguish contributions from shocks and DIG. There is no clear evidence of shock/DIG emission in individual galaxies, however we find some evidence of bulk DIG emission at 2σ significance across the entire sample. We estimate the DIG fraction in our sample to be $\sim 22\%$, in line with the expected fractions based on the resolved surface brightnesses of our sample, and thus conclude that DIG or shocked gas emission are not the primary emission sources in our targets.
- (3) *Escaping ionizing radiation*: In principle the $[\text{S III}]/[\text{S II}]$ ratio can identify locations of density-bounded H II regions with escaping ionizing radiation. We demonstrate for one object that high ionizing escape fractions are unlikely, although in general the $[\text{S III}]$ signals

are too weak to examine this possibility. Nonetheless future deep grism spectroscopy mapping the [S III] lines, for example with JWST, holds promise for further study.

- (4) *Star formation*: All targets in our sample exhibit spatially extended emission with high surface brightness and line ratios indicative of star forming H II regions. It is clear that star formation is responsible for the vast majority of emission line flux in our targets. Having found that shocks, DIG, and LINER emission cannot explain the observed BPT offsets, we conclude that these line ratio offsets are most likely caused by different physical characteristics of H II regions and/or young stars compared to typical star forming galaxies at $z \sim 0$. We consider trends in BPT offset with global properties of $z \sim 0$ star-forming galaxies, and find that the $z \sim 0.8$ sample follows similar relations. In particular the BPT offsets are consistent with expectations based on Balmer line luminosities and equivalent widths. The BPT offsets thus appear to be connected to high SFR and sSFR which are typical of high- z galaxies. Although not conclusive, the trend with sSFR supports recent work suggesting that α -enhanced abundance patterns cause BPT offsets at high redshift.

Overall, the spatially resolved data in our sample appear to be consistent with emission driven by star formation, despite their integrated line ratios being offset from the $z \sim 0$ BPT star forming locus. This highlights an important outstanding question in galaxy evolution studies: how do the physical properties of H II regions at high redshifts differ from those observed locally? In future work we intend to perform a thorough photo-ionization modeling analysis of this sample with a full suite of emission lines to further probe this question and discern between the properties that may drive line ratio offsets, such as high ionization parameters, enhanced N/O abundance, or high α /Fe. A key result of this work is that, since emission is powered by star formation, models of photoionization by massive stars should be appropriate for interpreting the spectra of high- z galaxies with similar BPT offsets. Likewise, direct-method abundance measurements (e.g., Jones et al., 2015; Sanders et al., 2020a) and other nebular emission probes should indeed reflect the physical conditions of H II regions.

Looking forward, we can soon extend this type of analysis to a wider range of redshifts and a larger sample size. JWST will provide increased SNR along with excellent spatial resolution through grisms, IFU, or slit-stepping to distinguish between the properties of nuclear regions, high surface

brightness regions, and galactic outskirts. This will allow further exploration of DIG emission and trends with surface brightness, and to use [S III] as a diagnostic of density-bounded H II regions with escaping ionizing radiation at high redshifts. Additionally, this analysis is not limited by spectra that cannot resolve H α and [N II]; as shown with the MaNGA data in Figure 3.1, we can clearly distinguish different physical mechanisms using the [S II]/(H α + [N II]) metric without high spectral resolution. Space-based grism spectroscopy is thus a powerful technique which can additionally benefit from multiplexing. While we found no strong evidence of properties beyond star formation in our sample, a larger spatially resolved sample can provide more certainty for high redshift galaxies as a broader population. However if high redshift galaxy emission is truly dominated by star formation, integrated emission line measurements are sufficient to discern between the various proposed properties within H II regions. Further understanding of the origin of emission line excitation at high redshift will improve our ability to calibrate metallicity measurements between the low and high redshift universe, and propel our knowledge of galaxy evolution.

CHAPTER 4

Conclusion

Stellar feedback is an integral component in galaxy formation and evolution. I measured gas velocity dispersion as a function of sSFR, in order to test theoretical predictions regarding whether the cusp-core problem may be resolved with stellar feedback. I found a direct relationship consistent with cosmological hydrodynamic simulations which suggests that stellar feedback is able to generate dark matter cores, and thus resolve the cusp-core problem in low mass galaxies. I also measured and analyzed spatially resolved emission line maps of $H\alpha+[N\ II]$, $[S\ II]$ and $[S\ III]$ for a sample of $z \sim 0.8$ galaxies in order to determine the specific processes that drive emission at high redshift and that result in the observed offset of high- z galaxies from the $z = 0$ BPT star forming locus. I found that the emission in high redshift galaxies is likely dominated by star forming H II regions, and that the physical characteristics of H II regions in high redshift galaxies must differ from what we observe locally. Understanding how the ISM environments evolve with redshift is a critical step in calibrating our metallicity measurement techniques across different epochs. This in turn is critical in order to use chemical evolution as a probe of stellar feedback.

Further analysis of the data presented in Chapter 2 can provide further constraints on the mass budget and dark matter in dwarf galaxies at moderate redshifts. Through analyzing the dynamical mass profiles of the OLAS sample, we can constrain the dark matter mass of the systems, specifically in the central regions where increased dark matter masses indicate cusps and reduced dark matter masses suggest cores. Similarly, we can explore whether stellar feedback is the primary mechanism of gas and heavy metal mixing in low mass galaxies. Through analyzing the metallicity gradients (available for a majority of the sample) we can determine if stellar feedback is strong enough to redistribute metals from the rich centers of star forming dwarf galaxies thus resulting in flattened metallicity gradients.

Up until recently we have not had the technology to resolve dwarf galaxies beyond the local group. As such, minimal progress has been made to observationally study how feedback driven

outflows affect the gravitational potential and dark matter distribution in dwarf galaxies or how these same outflows may disrupt the creation and distribution of heavy metals in low-mass galaxies. My work with the OLAS survey pushed resolved kinematics down to the lowest masses achieved at these redshifts, requiring the unique combination of AO and gravitational lensing to reach a suitable resolution of ~ 100 pc scales. Upcoming 30m-class facilities will enable even higher spatial resolution.

The next generation of telescopes will push to measurements we are unable to currently realistically achieve. In particular, future studies using JWST, TMT/IRIS and other ELTs will allow us to probe a wider dynamic range in sSFR, specifically towards the fainter end. More importantly, they will provide the sensitivity to measure kinematics from stellar absorption lines (although this will still be very difficult to measure), which are a more direct probe of the gravitational potential well compared to the gas kinematics analyzed in Chapter 2. Measuring the relationship between sSFR and stellar velocity dispersion provides a more direct test for stellar feedback resolving the cusp-core problem.

A careful photoionization modeling of the galaxies in the HST sample, coupled with a full suite of emission lines and stellar population synthesis can diagnose the specific properties of star formation that power emission lines at high redshift, discerning between high ionization parameters, enhanced N/O abundance, high α /F and more. This will provide a key step forward in the field of galaxy evolution studies, where most current studies assume $z = 0$ ISM conditions in high redshift galaxies in their analyses. Deep spectroscopy with JWST is expected to significantly expand the availability of T_e metallicities for high- z galaxies, with multiple Cycle 1 programs targeting auroral lines in ~ 100 galaxies each at $z > 1$. Future studies can utilize the methods of Chapter 3 applied to these and other future JWST programs to analyze a larger sample with deeper data. The increased sensitivity of JWST will also provide higher signal-to-noise measurements of [S III] and allow us to analyze whether escaping ionizing radiation may play a significant role in the emission properties of high redshift galaxies. Additionally, with the larger sample size and higher quality data we can use methods similar to those imparted in Chapter 3 to improve constraints on the DIG fraction in galaxies.

Overall, this is a critical time to study the role of stellar feedback in galaxy evolution. With all of the upcoming facilities such as JWST, 30-m class telescopes and AO upgrades to current observatories we are closing in on a new era of galaxy evolution research. In the next 5-10 years we expect an influx of high quality data (in terms of depth, spatial resolution, and AO corrections) that we can use to further constrain the role of stellar feedback in galaxy evolution. My work has acted as a preview of what we can expect to learn with future facilities. The lensed low-mass galaxy sample I analyzed in Chapter 2 is representative of the quality of data we can expect to observe with the higher resolution and sensitivity of upcoming ELTs *without* lensing; the combination of ELTs and lensing will push observations to lower mass galaxies and higher spatial resolutions. The spatially resolved HST sample with previous auroral line measurements I study in Chapter 3 can be achieved for a much larger sample with the capabilities of JWST.

With larger samples of deep observations of high redshift galaxies we will be able to better compare to simulations to discern between different feedback prescriptions, as well as refine our models for the next generation of cosmological simulations (e.g., upgrades to current simulation suites such as FIRE-2, Illustris-TNG, and NIHAO). Similarly, pinning down the primary emission line powering mechanisms at high redshift will allow us to better calibrate our metallicity measurements between the local and high redshift universes.

APPENDIX A

Fire Simulations

Table A.1 presents properties of the simulated galaxies from FIRE that were used in our analysis, as described in Section 2.3.3.

TABLE A.1. Simulated Galaxies

galaxy	resolution	mass ($z=1.5$) ^a	σ ($z=1.5$)	mass ($z=2$) ^b	σ ($z=2$)	citation
		$\log(M_*/M_\odot)$	km/s	$\log(M_*/M_\odot)$	km/s	
m11i	7100	7.64	6-38	-	-	El-Badry et al. (2018a)
m11q	880	8.05	4-66	-	-	Hopkins et al. (2018)
m11d	7100	8.39	5-43	8.25	9-40	El-Badry et al. (2018a)
m11e	7100	8.37	3-70	7.82	7-44	El-Badry et al. (2018a)
m11h	7100	8.67	15-52	8.38	12-68	El-Badry et al. (2018a)
m12z	4200	8.88	15-75	8.53	11-48	Hopkins et al. (2018)
m12c	7100	9.23	13-54	-	-	Hopkins et al. (2018)
m12m	7100	9.68	31-125	9.29	12-92	Hopkins et al. (2018)
m12i	7100	9.74	28-80	9.36	20-89	Hopkins et al. (2018)

^a $z \sim 1.5$ ranges from $z = 1.32 - 1.72$.

^b $z \sim 2$ ranges from $z = 1.89 - 2.57$.

APPENDIX B

OLAS Kinematic Maps

Maps of kinematics, $H\alpha$ emission, and HST broad-band images of each target are presented in Figures B.1 - B.17. The methods for generating these maps are described in Section 2.3.1.

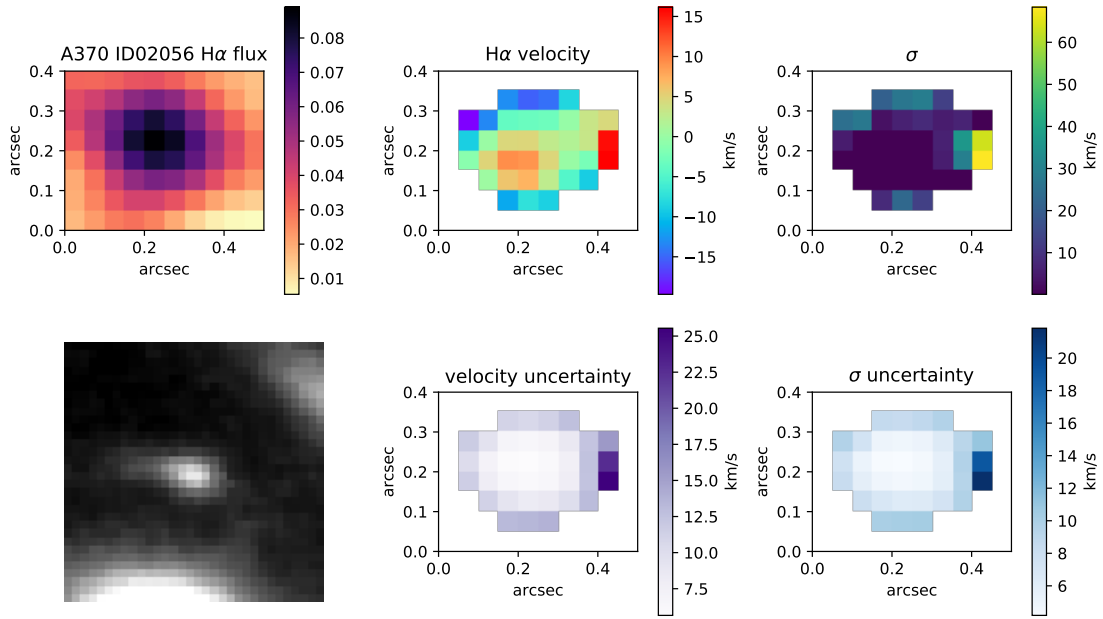


FIGURE B.1. From left to right: (Top) $H\alpha$ flux map, $H\alpha$ velocity map, σ map, (Bottom) Hubble Image, velocity uncertainty map, σ uncertainty map for A370 ID02056. The HST image field of view is 2x2 arcseconds.

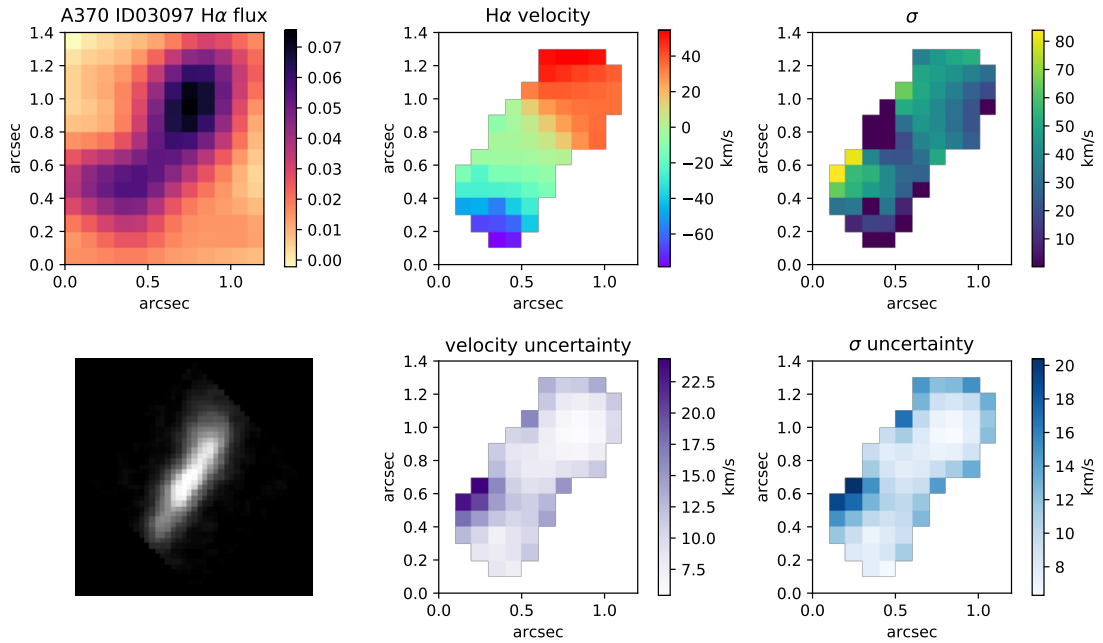


FIGURE B.2. Same as Figure B.1, for A370 ID03097

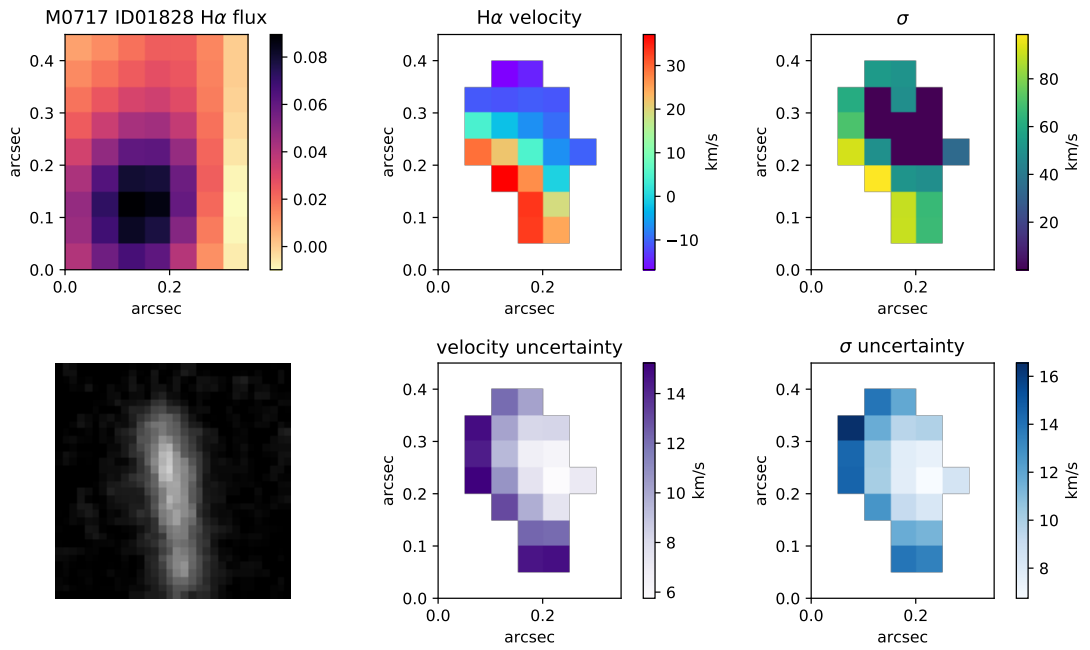


FIGURE B.3. Same as Figure B.1, for M0717 ID01828

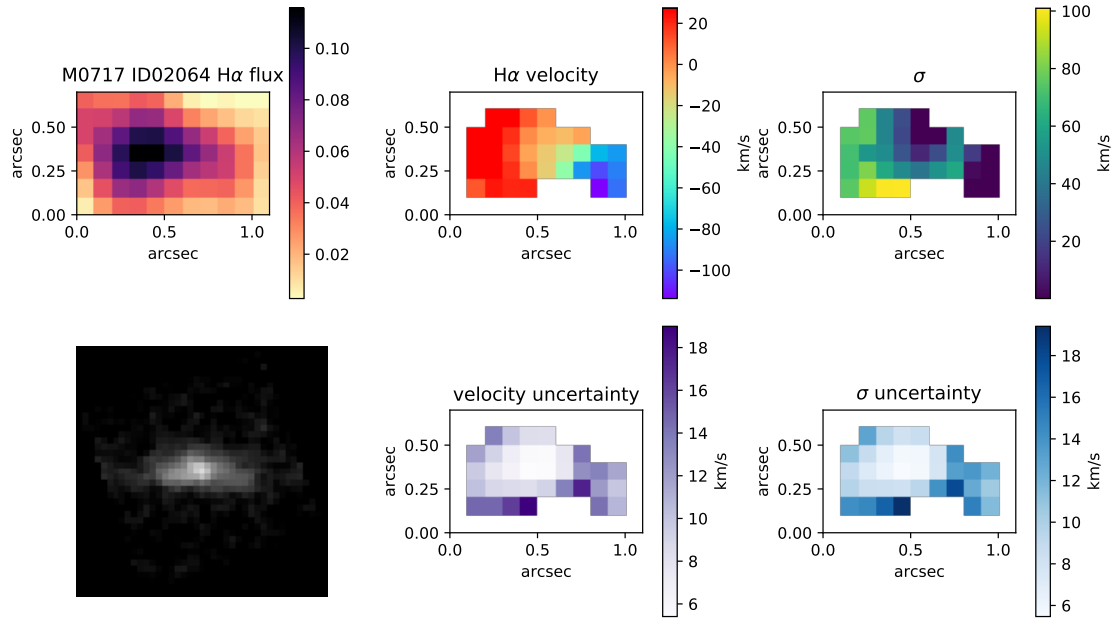


FIGURE B.4. Same as Figure B.1, for M0717 ID02064

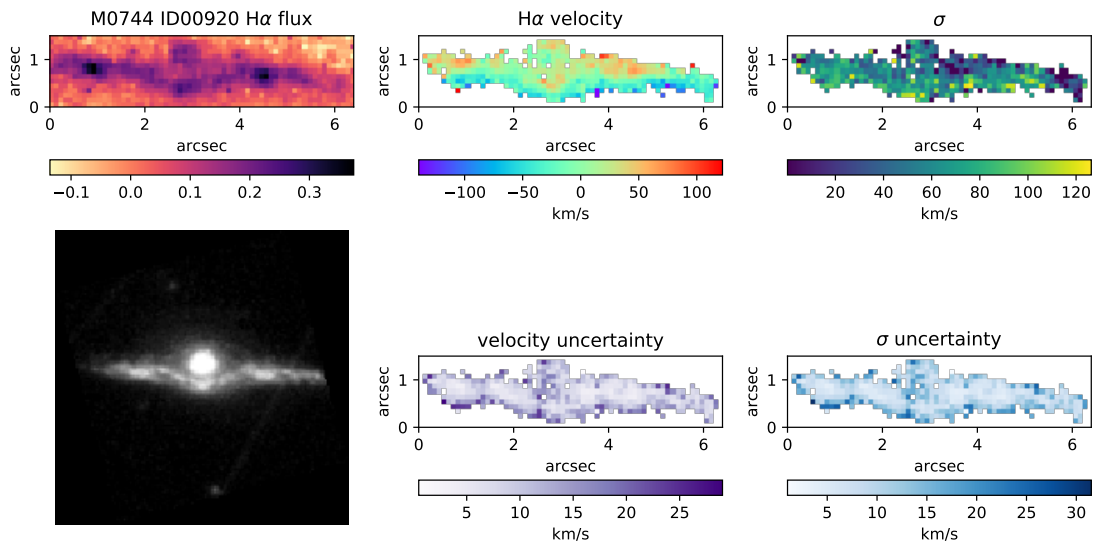


FIGURE B.5. Same as Figure B.1, for M0744 ID00920. The HST image field of view is 7x7 arcseconds.

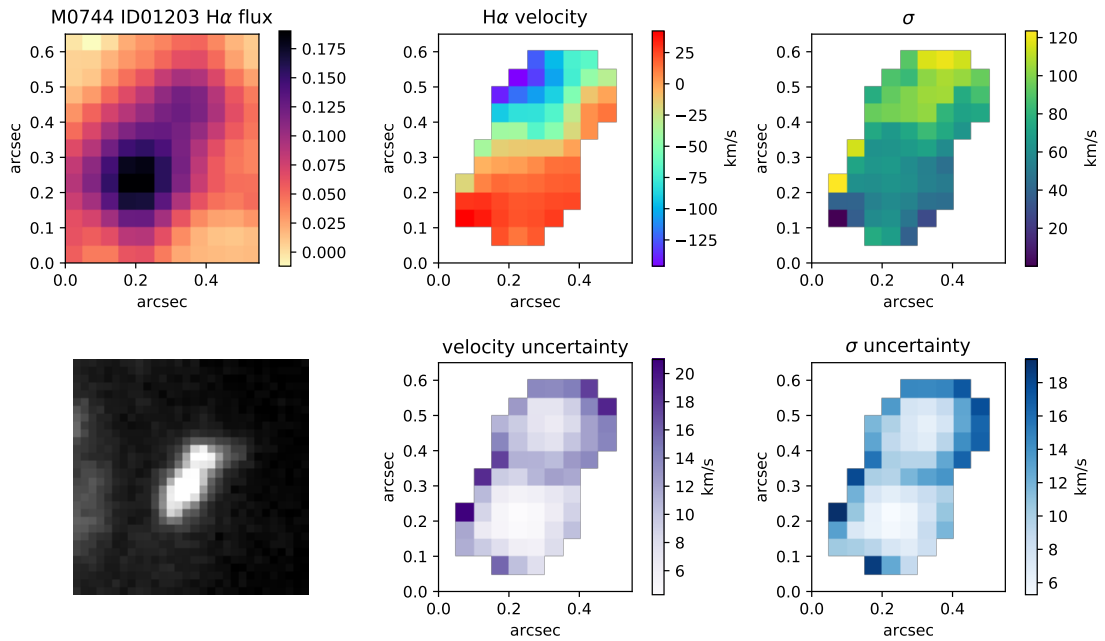


FIGURE B.6. Same as Figure B.1, for M0744 ID01203

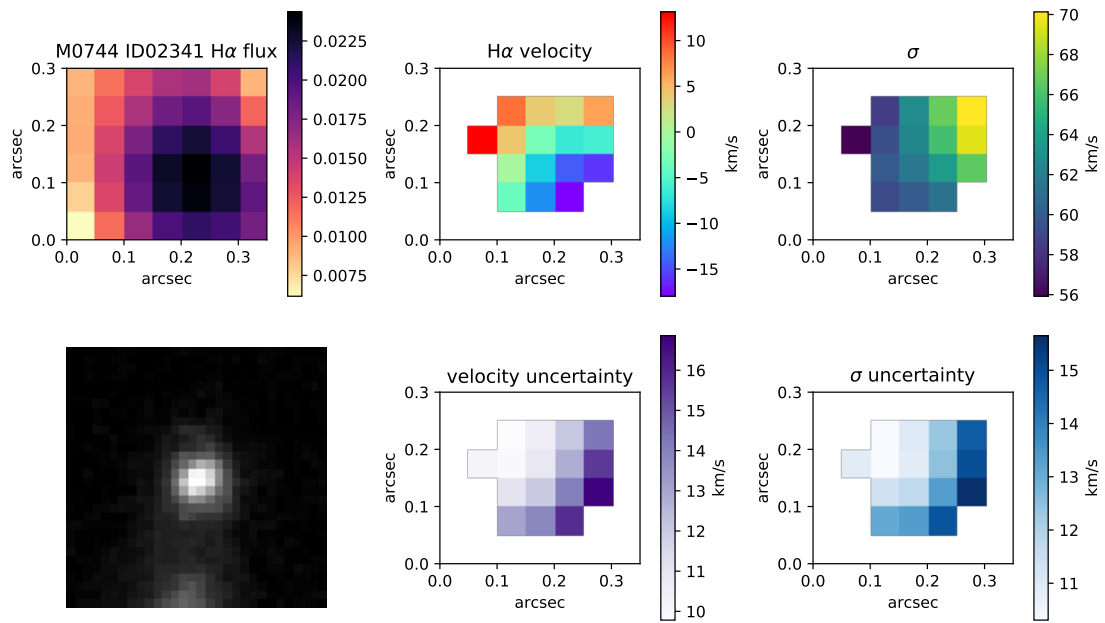


FIGURE B.7. Same as Figure B.1, for M0744 ID02341

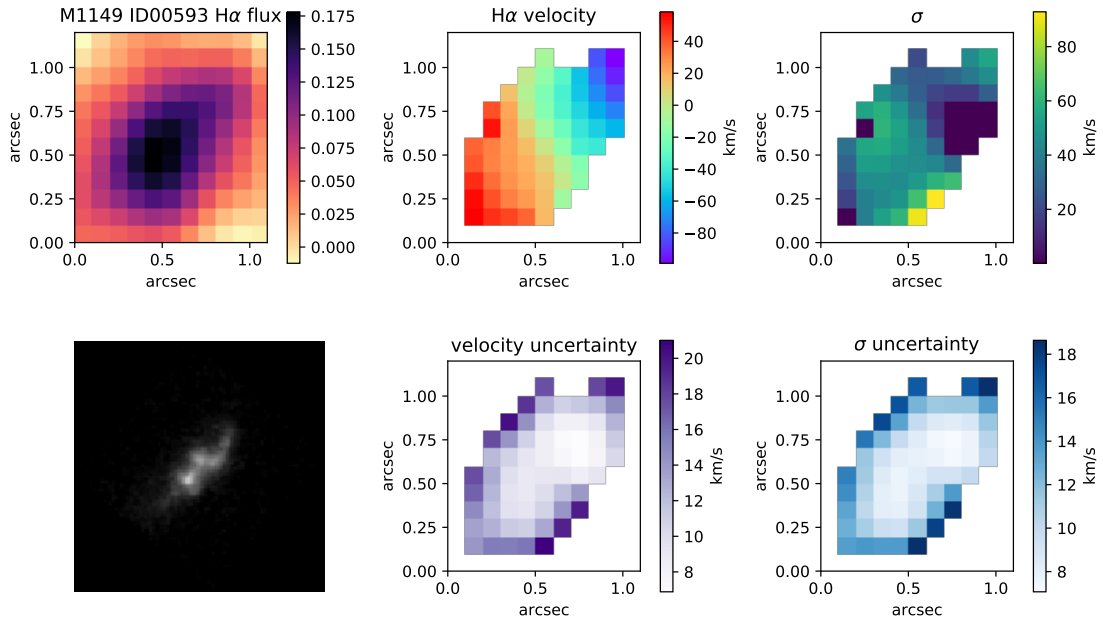


FIGURE B.8. Same as Figure B.1, for M1149 ID00593

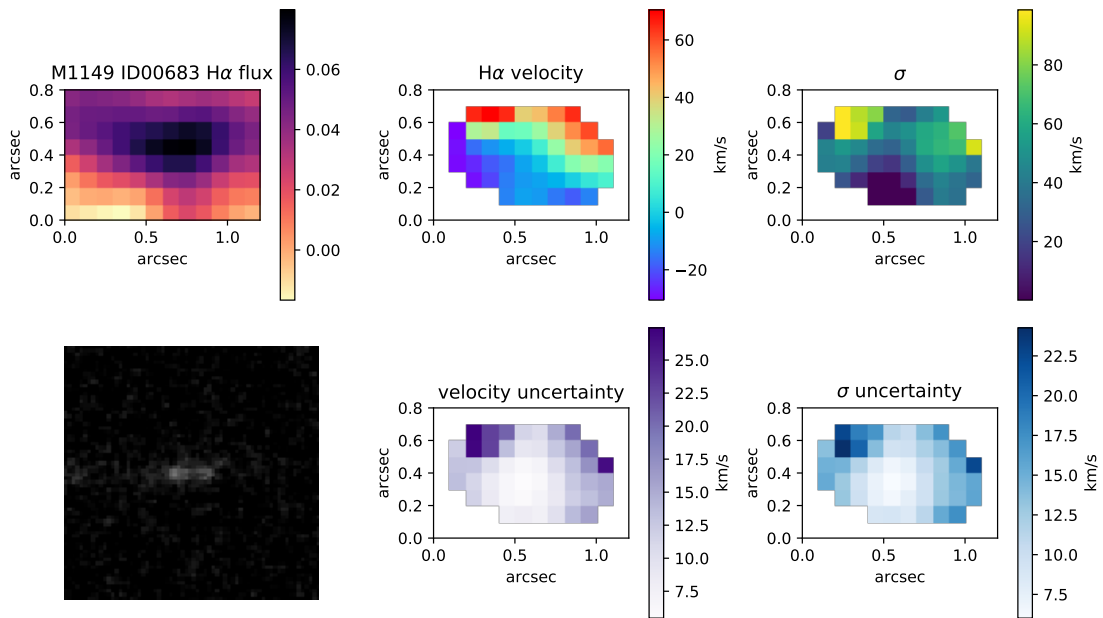


FIGURE B.9. Same as Figure B.1, for M1149 ID00683

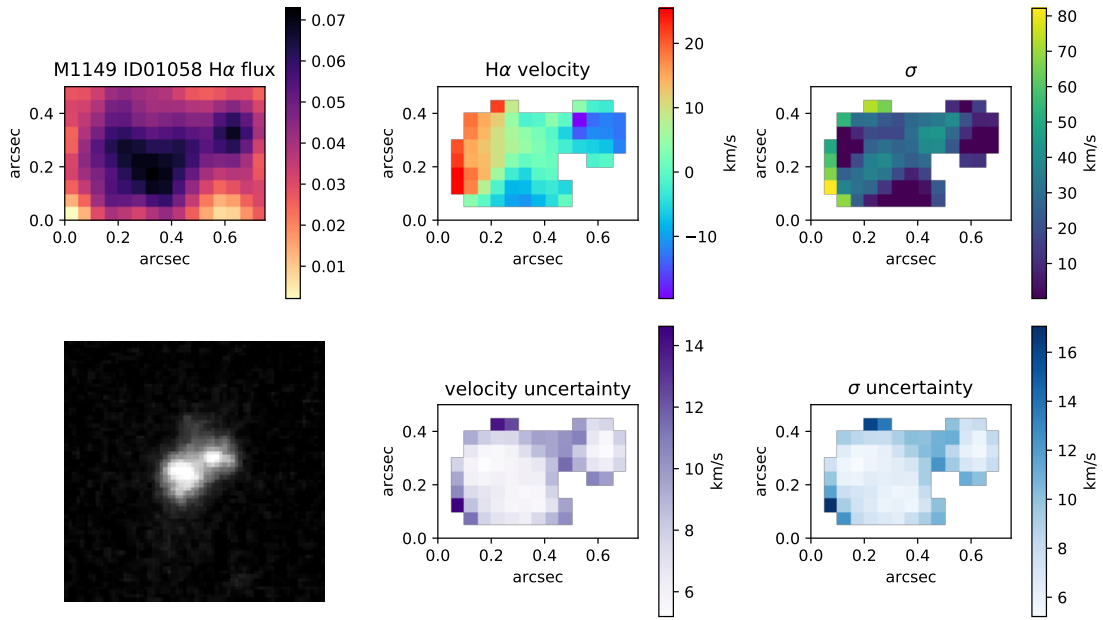


FIGURE B.10. Same as Figure B.1, for M1149 ID01058

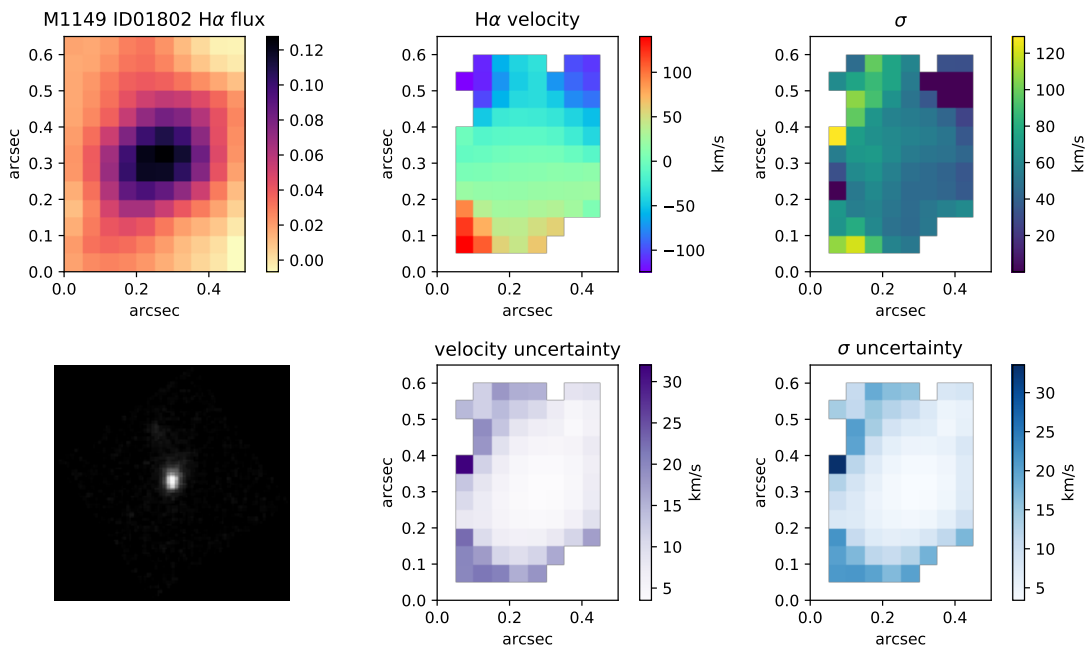


FIGURE B.11. Same as Figure B.1, for M1149 ID01802

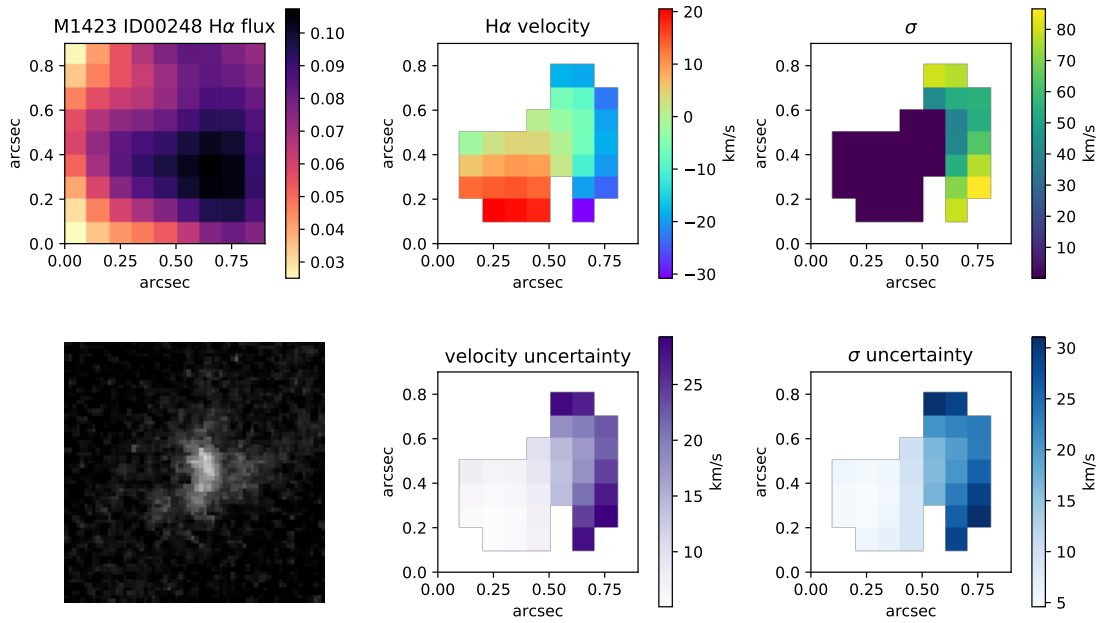


FIGURE B.12. Same as Figure B.1, for M1423 ID00248

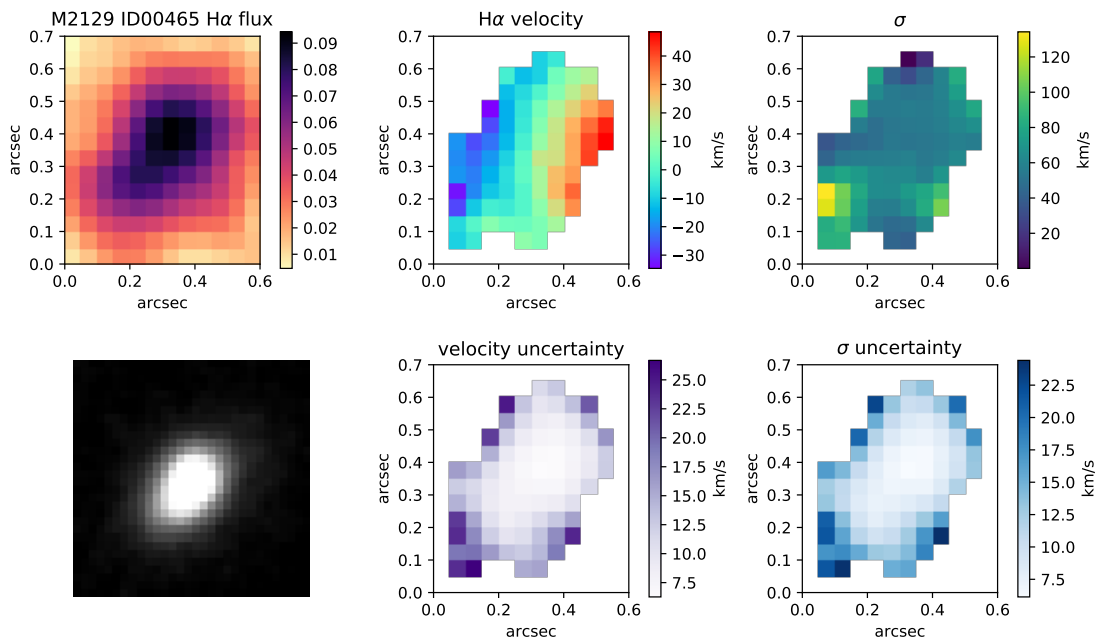


FIGURE B.13. Same as Figure B.1, for M2129 ID00465

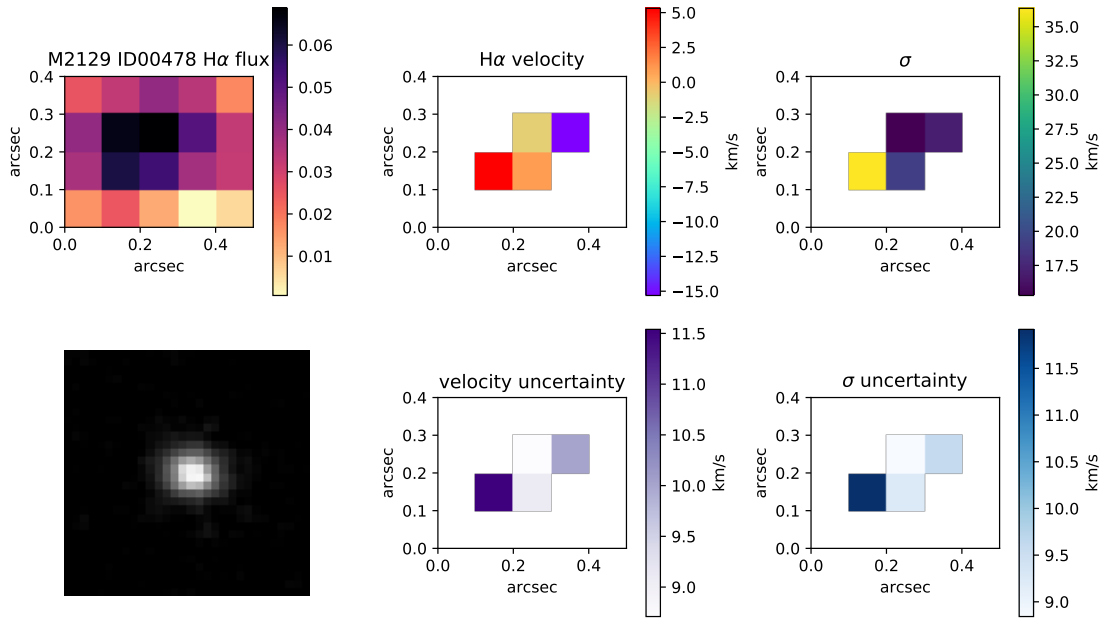


FIGURE B.14. Same as Figure B.1, for M2129 ID00478

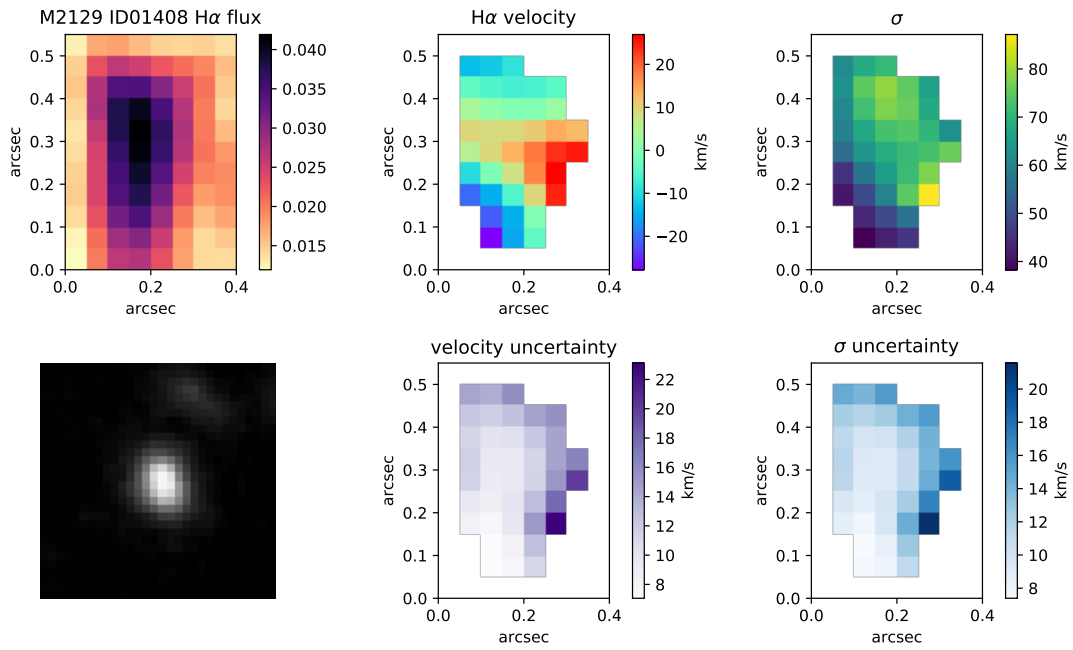


FIGURE B.15. Same as Figure B.1, for M2129 ID01408

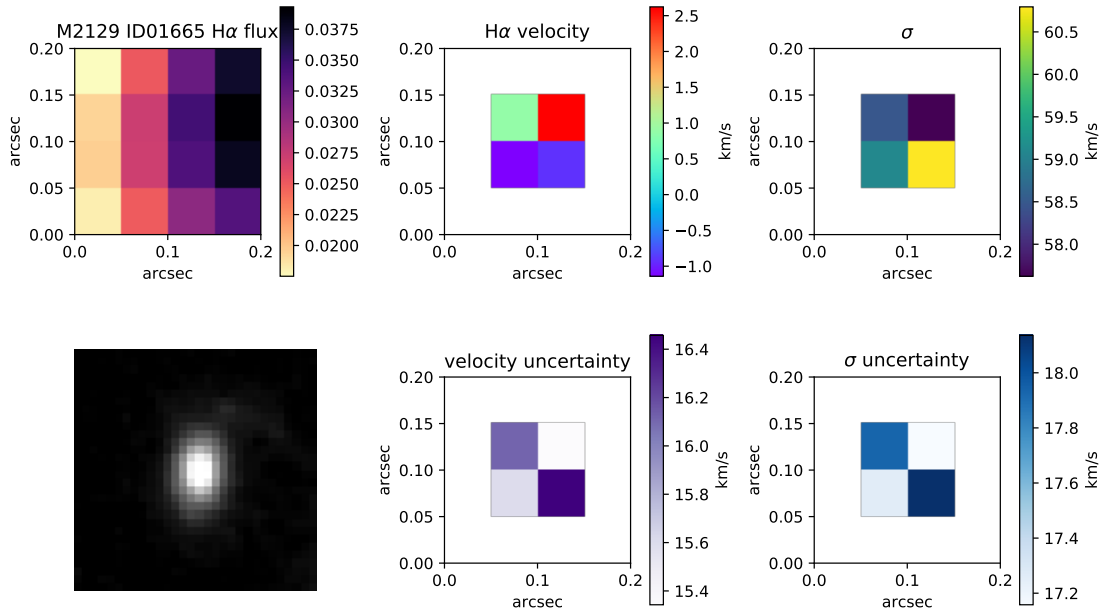


FIGURE B.16. Same as Figure B.1, for M2129 ID01665

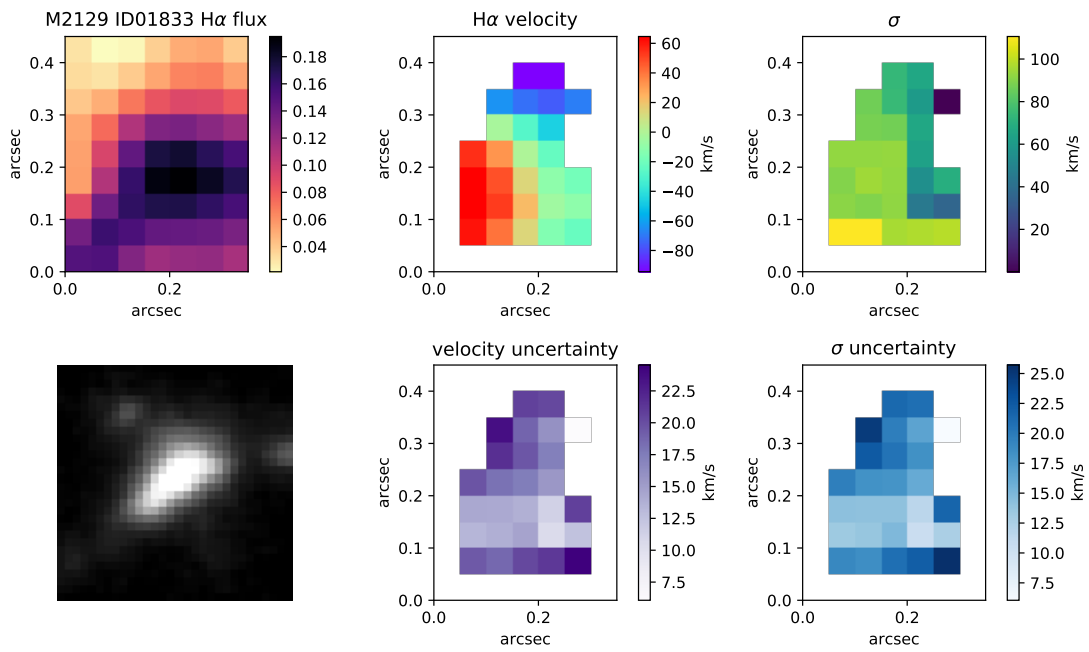


FIGURE B.17. Same as Figure B.1, for M2129 ID01833

APPENDIX C

HST Emission Line Maps

Emission line maps and $[\text{S II}]/(\text{H}\alpha + [\text{N II}])$ line ratio analysis for the galaxy DEEP2-13043716 are shown in Figures 3.7 and 3.8, and interpretation of this example object is discussed in Section 3.4. Equivalent data are shown in Figures C.1-C.14 for the remaining 14 galaxies in our sample.

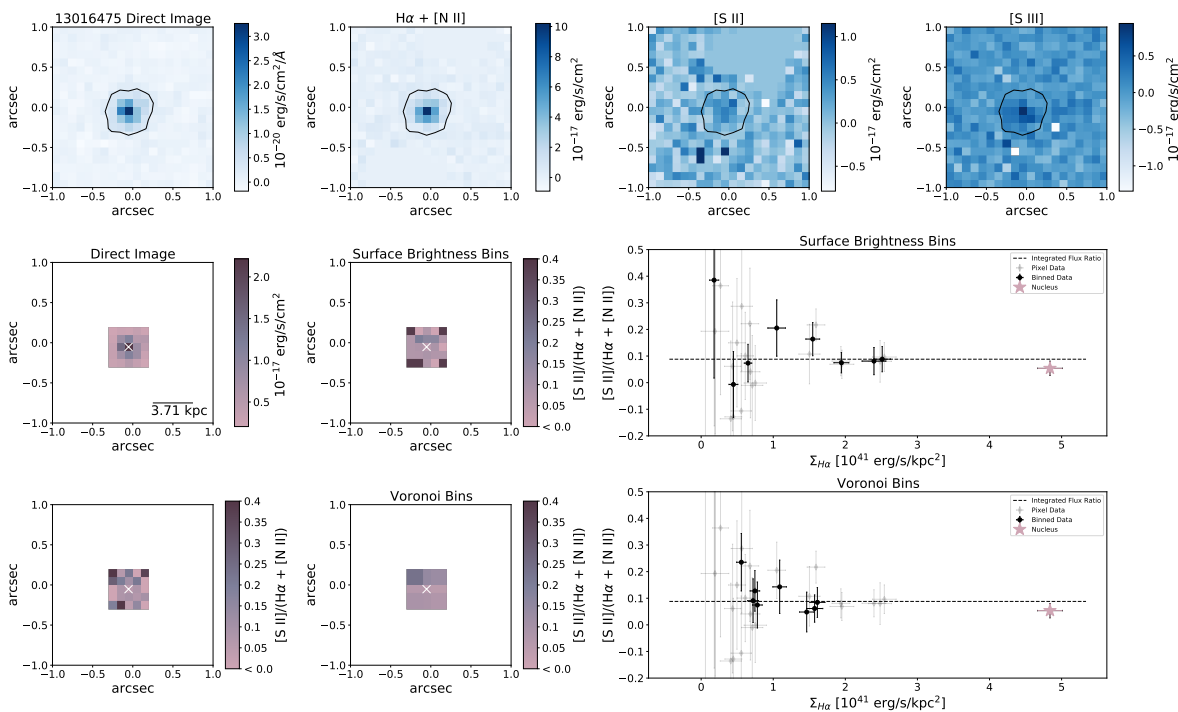


FIGURE C.1. Top Row: Same as Figure 3.6, Bottom Rows: Same as Figure 3.7.

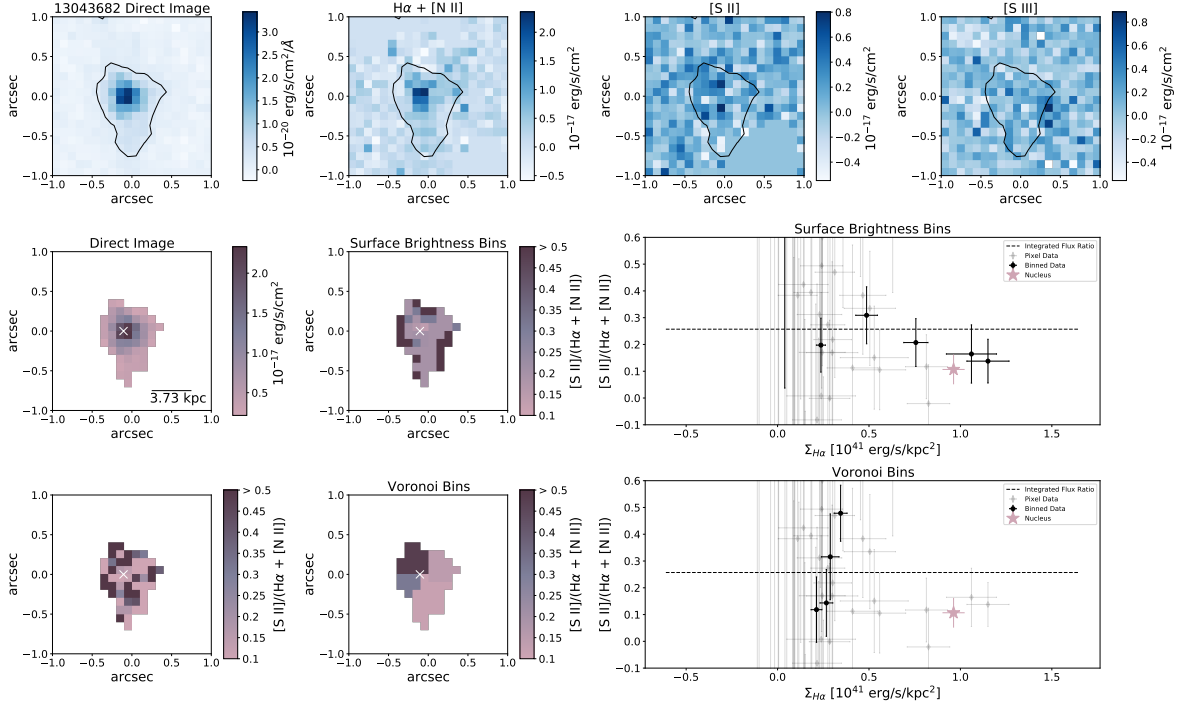


FIGURE C.2. Top Row: Same as Figure 3.6, Bottom Rows: Same as Figure 3.7.

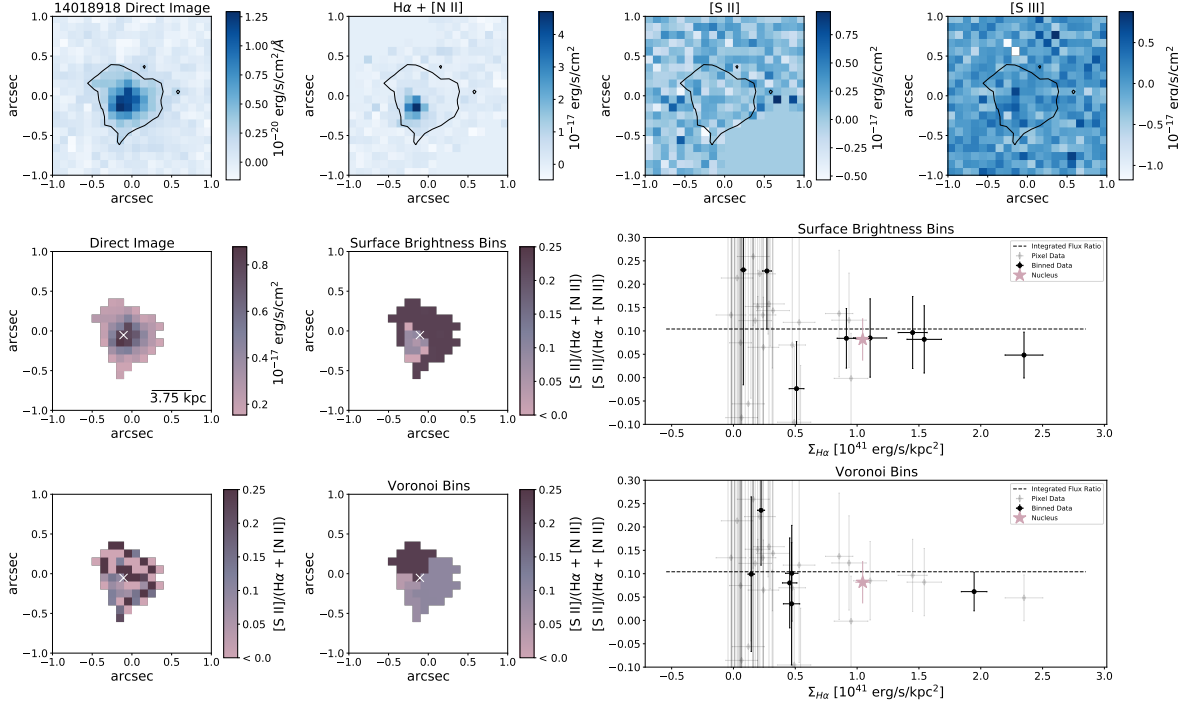


FIGURE C.3. Top Row: Same as Figure 3.6, Bottom Rows: Same as Figure 3.7.

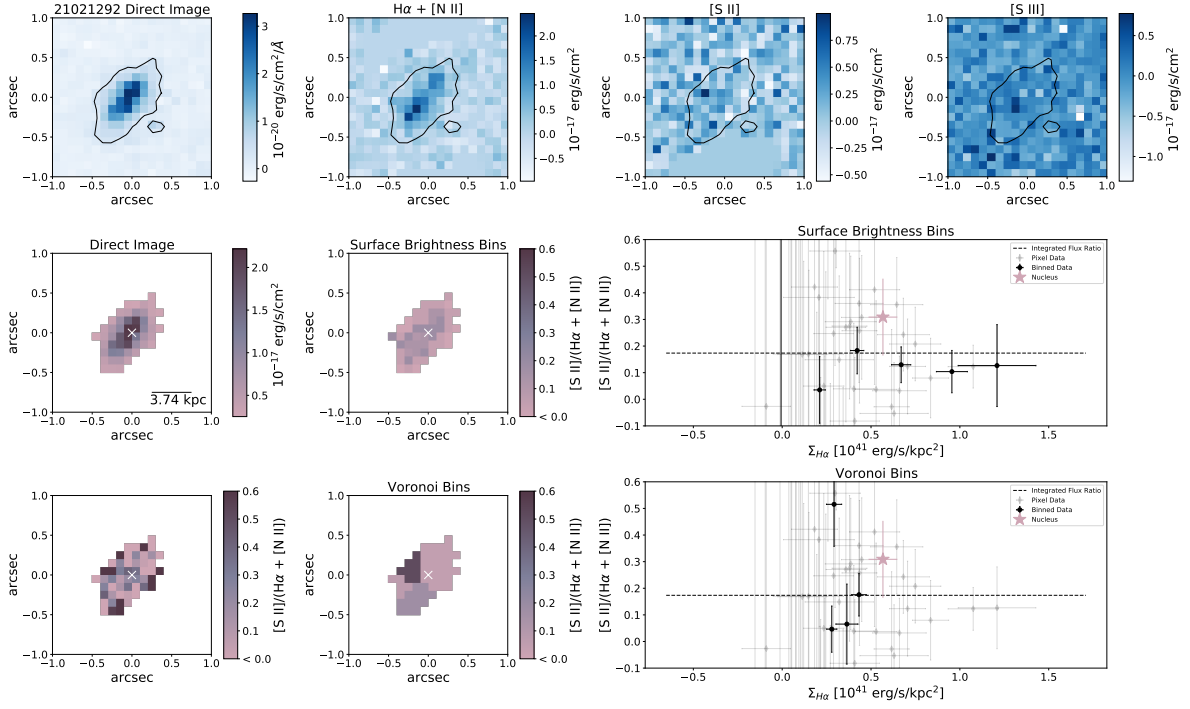


FIGURE C.4. Top Row: Same as Figure 3.6, Bottom Rows: Same as Figure 3.7.

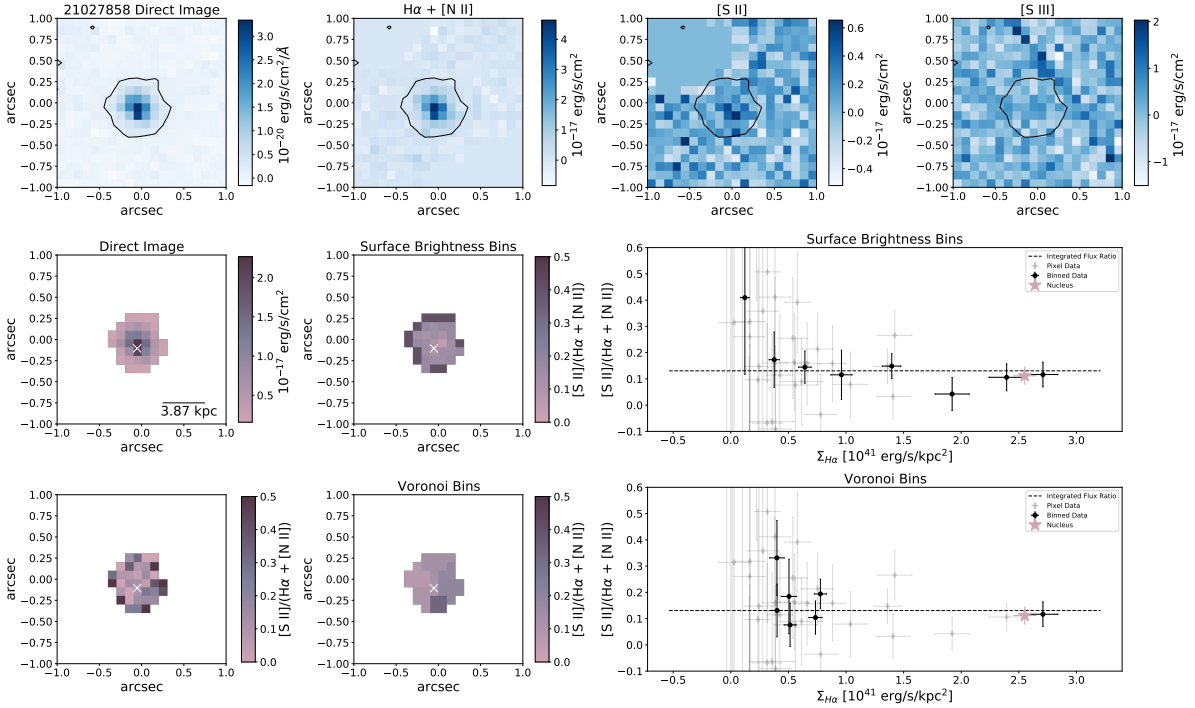


FIGURE C.5. Top Row: Same as Figure 3.6, Bottom Rows: Same as Figure 3.7.

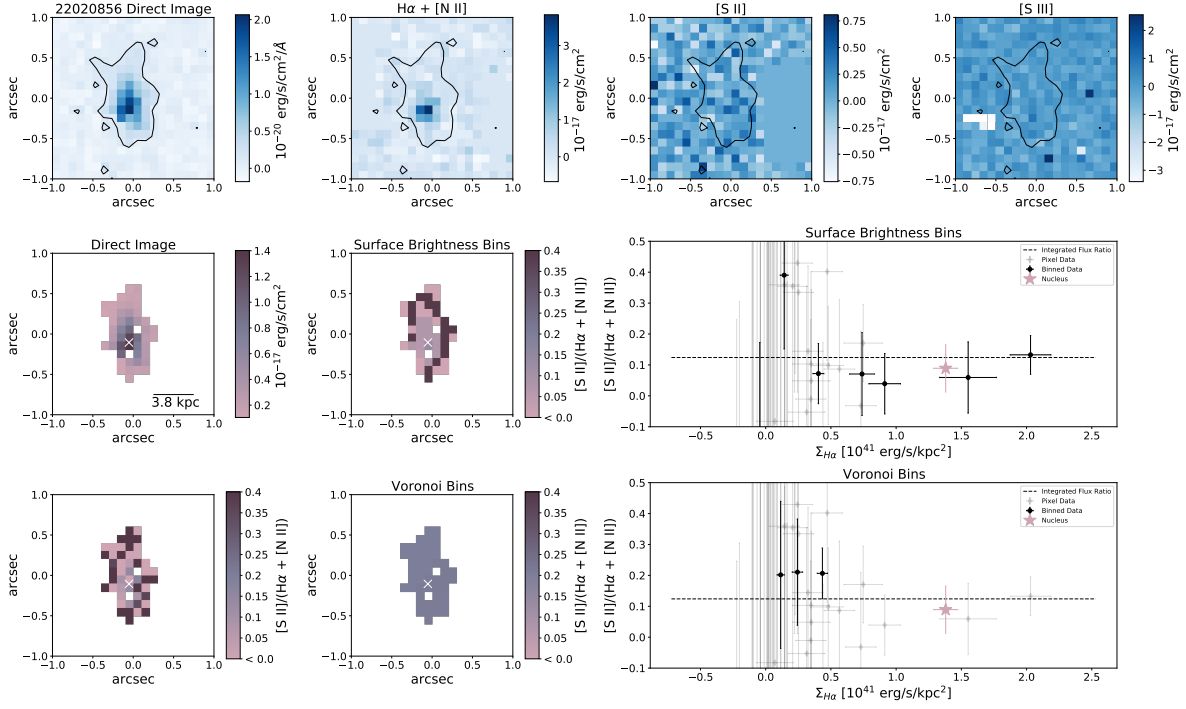


FIGURE C.6. Top Row: Same as Figure 3.6, Bottom Rows: Same as Figure 3.7.

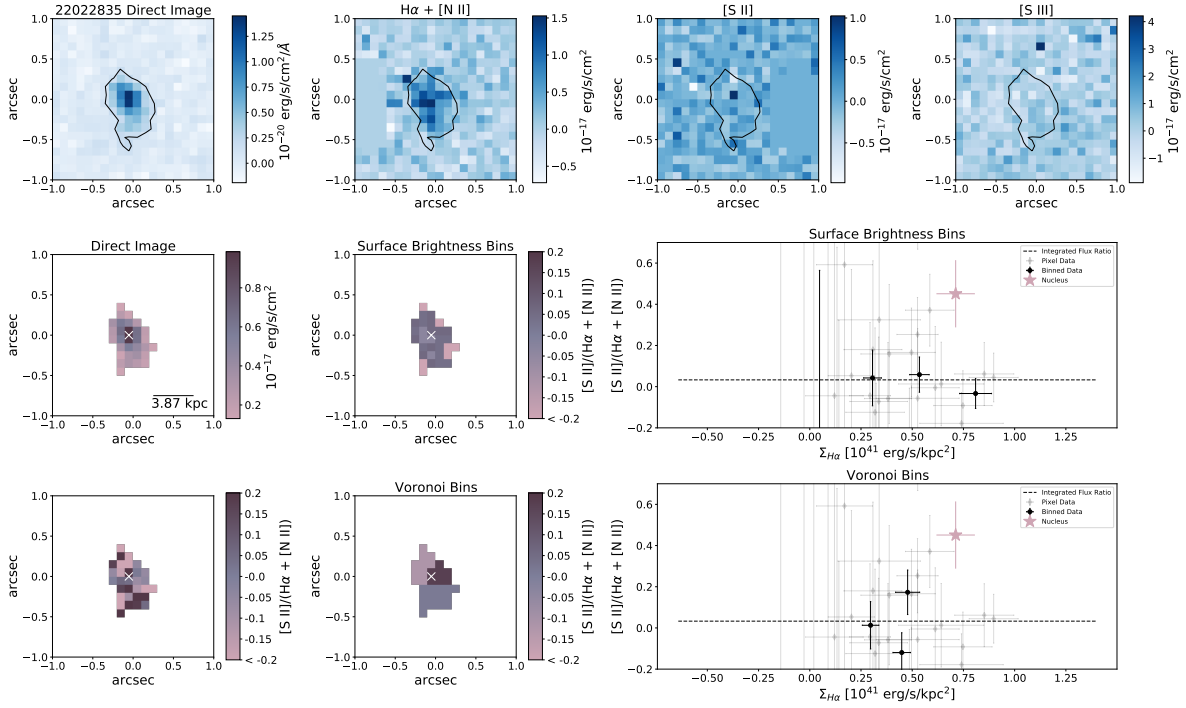


FIGURE C.7. Top Row: Same as Figure 3.6, Bottom Rows: Same as Figure 3.7.

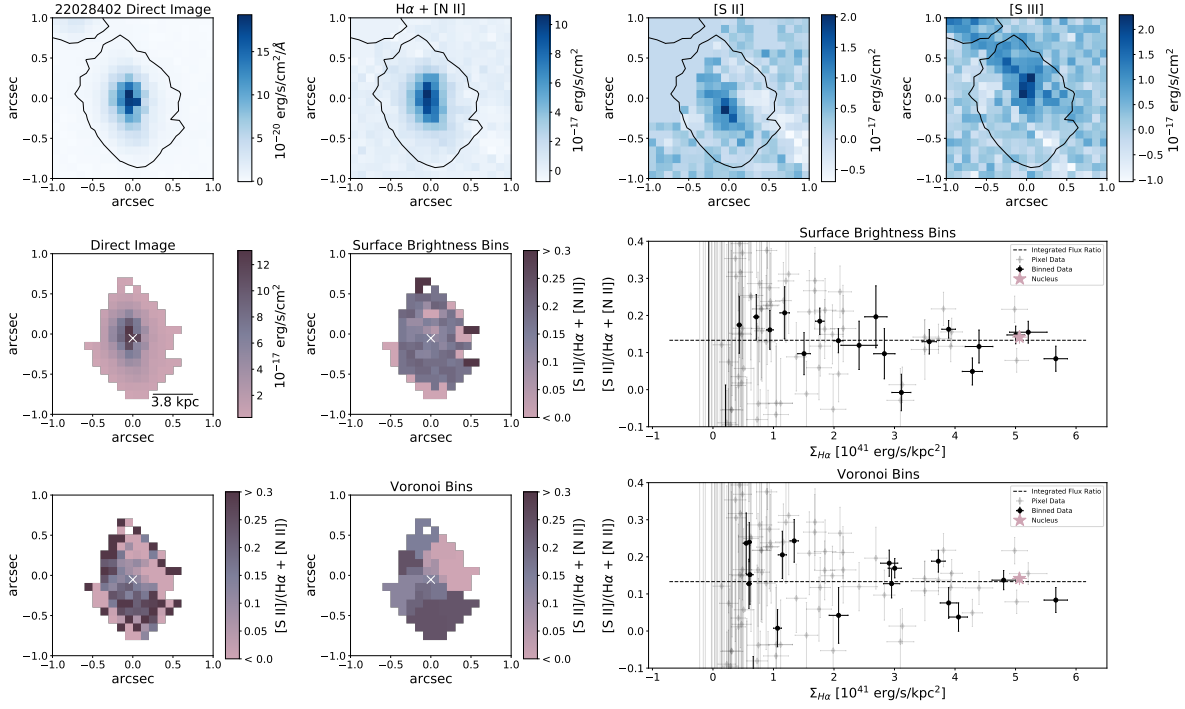


FIGURE C.8. Top Row: Same as Figure 3.6, Bottom Rows: Same as Figure 3.7.

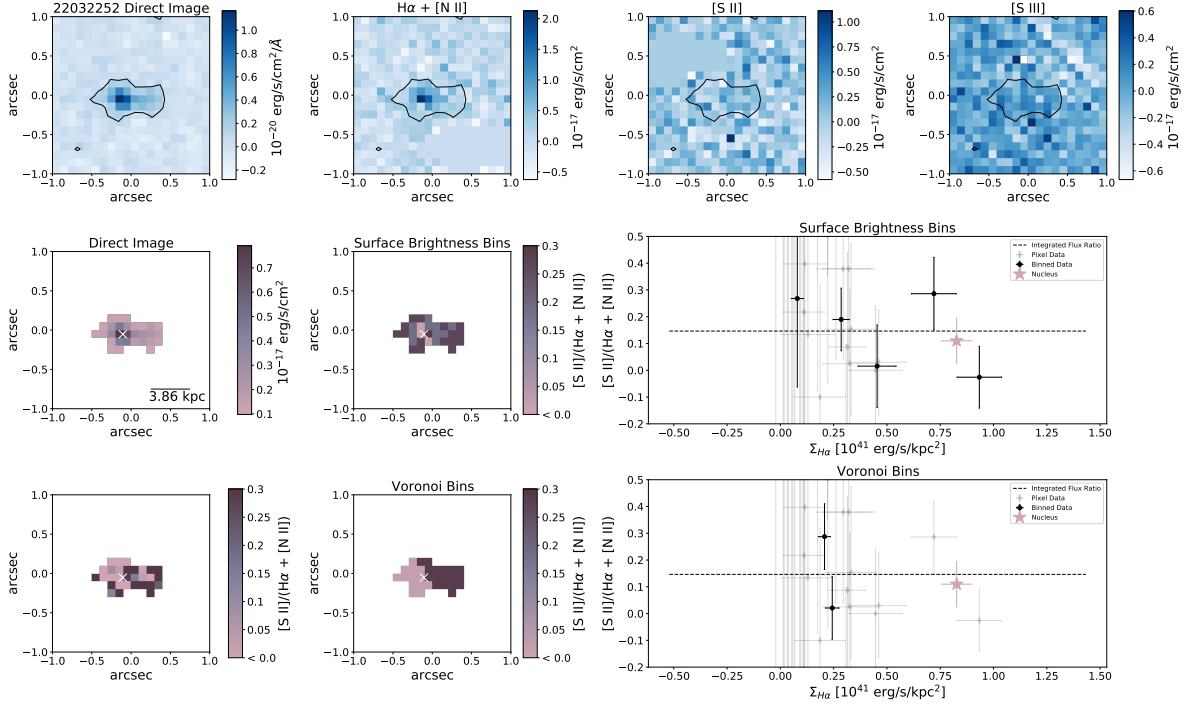


FIGURE C.9. Top Row: Same as Figure 3.6, Bottom Rows: Same as Figure 3.7.

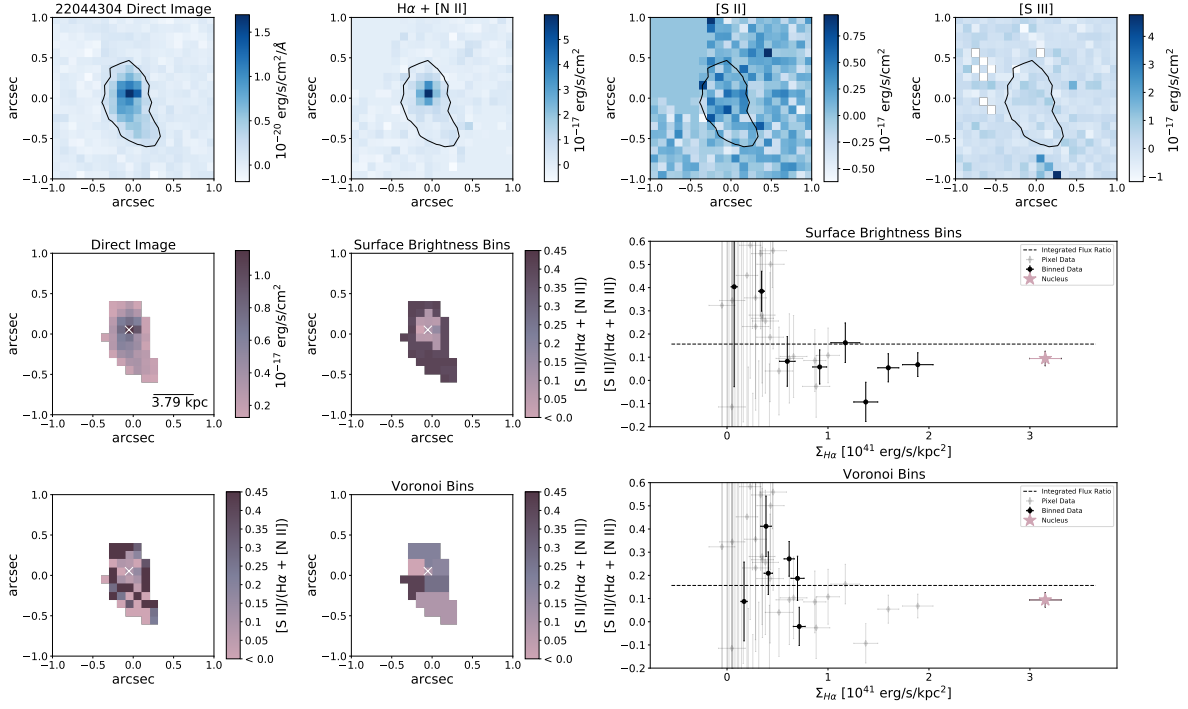


FIGURE C.10. Top Row: Same as Figure 3.6, Bottom Rows: Same as Figure 3.7.

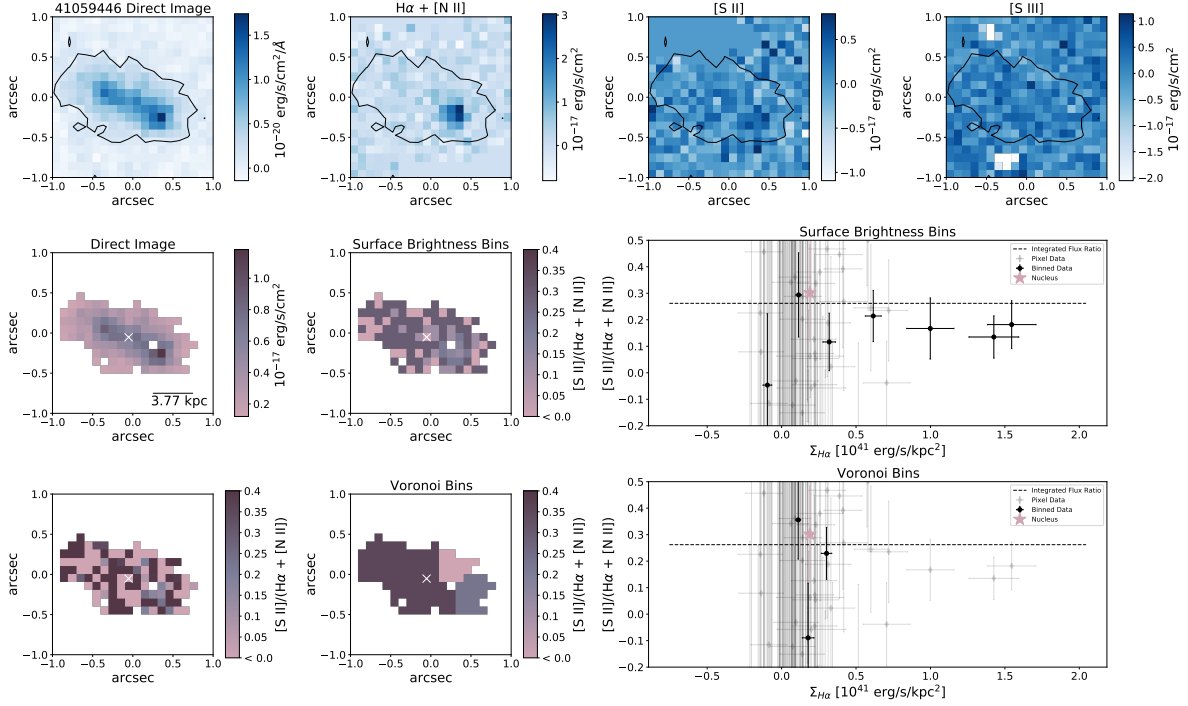


FIGURE C.11. Top Row: Same as Figure 3.6, Bottom Rows: Same as Figure 3.7.

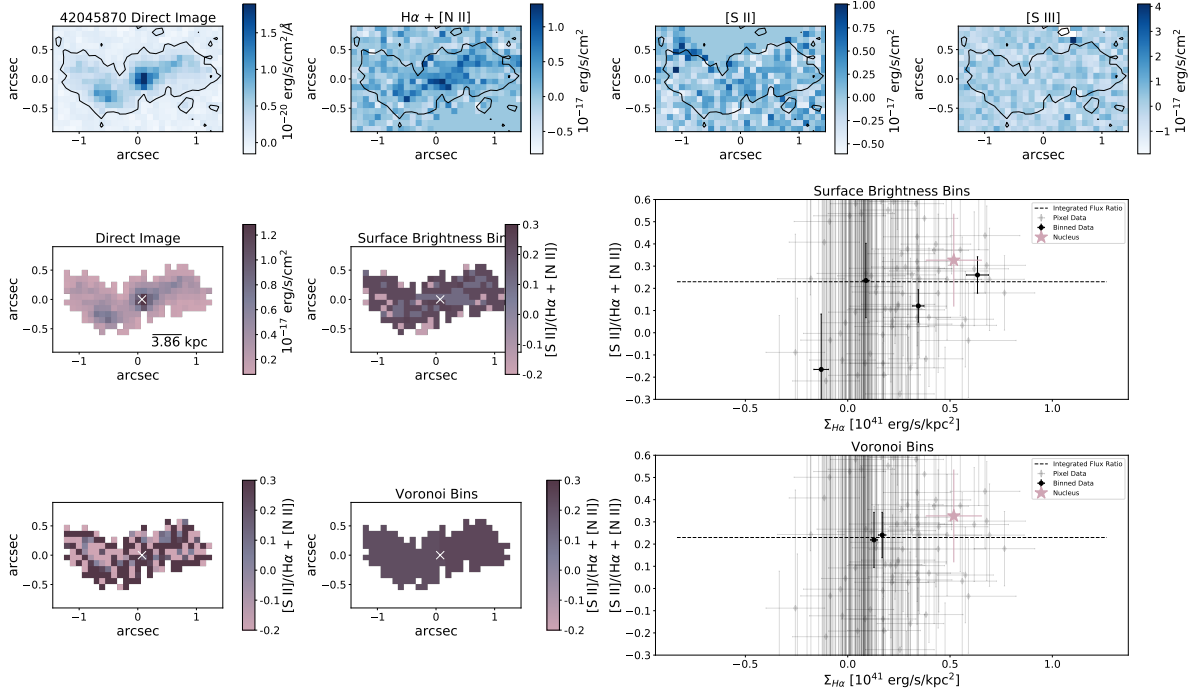


FIGURE C.12. Top Row: Same as Figure 3.6, Bottom Rows: Same as Figure 3.7.

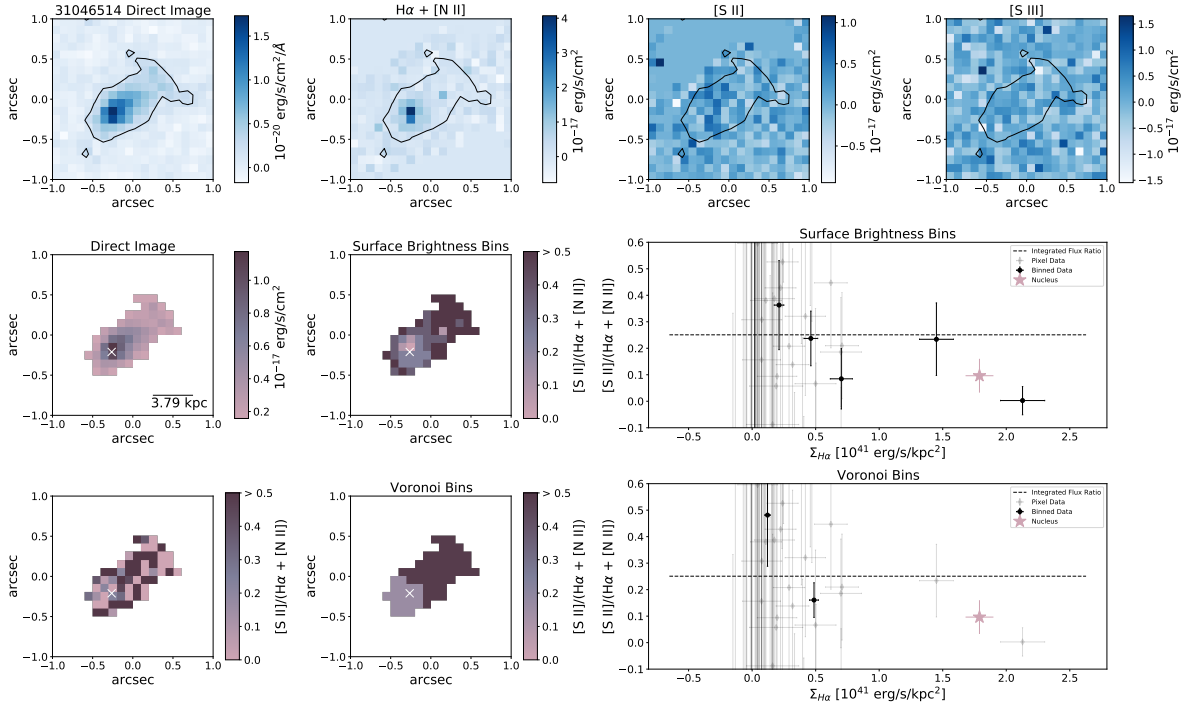


FIGURE C.13. Top Row: Same as Figure 3.6, Bottom Rows: Same as Figure 3.7.

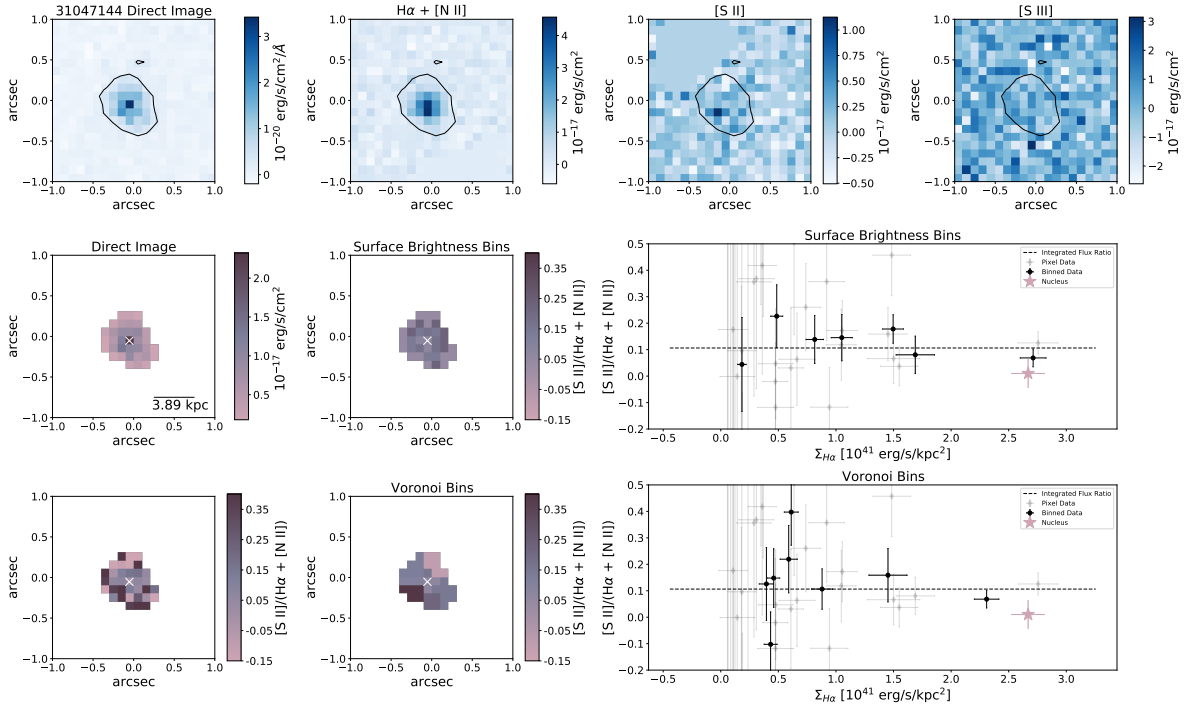


FIGURE C.14. Top Row: Same as Figure 3.6, Bottom Rows: Same as Figure 3.7.

Bibliography

- Abazajian, K. N., Adelman-McCarthy, J. K., Agüeros, M. A., et al. 2009, *Astrophysical Journals*, 182, 543
- Alexandroff, R. M., Heckman, T. M., Borthakur, S., Overzier, R., & Leitherer, C. 2015, *The Astrophysical Journal*, 810, 104
- Anglés-Alcázar, D., Faucher-Giguère, C.-A., Kereš, D., et al. 2017, *Monthly Notices of the Royal Astronomical Society*, 470, 4698
- Baldwin, J. A., Phillips, M. M., & Terlevich, R. 1981, *Publications of the ASP*, 93, 5
- Beckman, J. E., Rozas, M., Zurita, A., Watson, R. A., & Knapen, J. H. 2000, *The Astronomical Journal*, 119, 2728
- Belfiore, F., Maiolino, R., Maraston, C., et al. 2016, *Monthly Notices of the Royal Astronomical Society*, 461, 3111
- Berg, D. A., Skillman, E. D., Croxall, K. V., et al. 2015, *Astrophysical Journal*, 806, 16
- Bian, F., Kewley, L. J., & Dopita, M. A. 2018, *Astrophysical Journal*, 859, 175
- Bose, S., Frenk, C. S., Jenkins, A., et al. 2018, *ArXiv e-prints*, arXiv:1810.03635
- Boylan-Kolchin, M., Bullock, J. S., & Kaplinghat, M. 2011, *Monthly Notices of the Royal Astronomical Society*, 415, L40
- Bradač, M., Treu, T., Applegate, D., et al. 2009, *The Astrophysical Journal*, 706, 1201
- Bradač, M., Schneider, P., Lombardi, M., & Erben, T. 2005, *A&A*, 437, 39
- Brammer, G. 2019, *Grizli: Grism redshift and line analysis software*, ascl:1905.001
- Brinchmann, J., Pettini, M., & Charlot, S. 2008, *Monthly Notices of the Royal Astronomical Society*, 385, 769
- Bruzual, G., & Charlot, S. 2003, *Monthly Notices of the Royal Astronomical Society*, 344, 1000
- Buckley, M. R., & Fox, P. J. 2010, *Phys. Rev. D*, 81, 083522
- Bullock, J. S., & Boylan-Kolchin, M. 2017, *Annual Review of Astronomy and Astrophysics*, 55, 343

Bundy, K., Bershady, M. A., Law, D. R., et al. 2015, *Astrophysical Journal*, 798, 7

Burkert, A., Genzel, R., Bouché, N., et al. 2010, *The Astrophysical Journal*, 725, 2324

Calzetti, D., Armus, L., Bohlin, R. C., et al. 2000, *The Astrophysical Journal*, 533, 682

Cappellari, M., & Copin, Y. 2003, *Monthly Notices of the Royal Astronomical Society*, 342, 345

Chabrier, G. 2003, *Publications of the ASP*, 115, 763

Chan, T. K., Kere, D., Oorbe, J., et al. 2015, *Monthly Notices of the Royal Astronomical Society*, 454, 2981

Contini, T., Epinat, B., Bouché, N., et al. 2016, *A&A*, 591, A49

Cowie, L. L., Barger, A. J., & Songaila, A. 2016, *Astrophysical Journal*, 817, 57

Croxall, K. V., Pogge, R. W., Berg, D. A., Skillman, E. D., & Moustakas, J. 2015, *Astrophysical Journal*, 808, 42

—. 2016, *Astrophysical Journal*, 830, 4

Curti, M., Mannucci, F., Cresci, G., & Maiolino, R. 2020, *Monthly Notices of the Royal Astronomical Society*, 491, 944

Davé, R., Finlator, K., & Oppenheimer, B. D. 2012, *Monthly Notices of the Royal Astronomical Society*, 421, 98

Davis, M., Faber, S. M., Newman, J., et al. 2003, in *Discoveries and Research Prospects from 6- to 10-Meter-Class Telescopes II*, ed. P. Guhathakurta, Vol. 4834, *International Society for Optics and Photonics (SPIE)*, 161 – 172

de Blok, W. J. G., Walter, F., Brinks, E., et al. 2008, *The Astronomical Journal*, 136, 2648

Dekel, A., Freundlich, J., Jiang, F., et al. 2021, *arXiv e-prints*, arXiv:2106.01378

El-Badry, K., Wetzel, A., Geha, M., et al. 2016, *The Astrophysical Journal*, 820, 131

El-Badry, K., Wetzel, A. R., Geha, M., et al. 2017, *The Astrophysical Journal*, 835, 193

El-Badry, K., Bradford, J., Quataert, E., et al. 2018a, *Monthly Notices of the Royal Astronomical Society*, 477, 1536

El-Badry, K., Quataert, E., Wetzel, A., et al. 2018b, *Monthly Notices of the Royal Astronomical Society*, 473, 1930

Emami, N., Siana, B., Weisz, D. R., & Johnson, B. D. 2018, *ArXiv e-prints*, arXiv:1809.06380

Finney, E. Q., Bradač, M., Huang, K.-H., et al. 2018, *The Astrophysical Journal*, 859, 58

Förster Schreiber, N. M., Renzini, A., Mancini, C., et al. 2018, ArXiv e-prints, arXiv:1802.07276

Förster Schreiber, N. M., Übler, H., Davies, R. L., et al. 2019, *Astrophysical Journal*, 875, 21

Freeman, W. R., Siana, B., Kriek, M., et al. 2019, *Astrophysical Journal*, 873, 102

Gburek, T., Siana, B., Alavi, A., et al. 2019, *Astrophysical Journal*, 887, 168

Genzel, R., Newman, S., Jones, T., et al. 2011, *The Astrophysical Journal*, 733, 101

Genzel, R., Förster Schreiber, N. M., Rosario, D., et al. 2014, *Astrophysical Journal*, 796, 7

Gibson, B. K., Pilkington, K., Brook, C. B., Stinson, G. S., & Bailin, J. 2013, *A&A*, 554, A47

Governato, F., Zolotov, A., Pontzen, A., et al. 2012, *Monthly Notices of the Royal Astronomical Society*, 422, 1231

Gray, W. J., & Scannapieco, E. 2017, *The Astrophysical Journal*, 849, 132

Hirtenstein, J., Jones, T., Wang, X., et al. 2019, *Astrophysical Journal*, 880, 54

Hoag, A., Bradač, M., Trenti, M., et al. 2017, *Nature Astronomy*, 1, 0091 EP

Hopkins, P. F., Wetzel, A., Kere, D., et al. 2018, *Monthly Notices of the Royal Astronomical Society*, 480, 800

Huang, K.-H., Lemaux, B. C., Schmidt, K. B., et al. 2016, *The Astrophysical Journal Letters*, 823, L14

Hung, C.-L., Hayward, C. C., Yuan, T., et al. 2018, ArXiv e-prints, arXiv:1806.04233

Izotov, Y. I., Stasińska, G., Meynet, G., Guseva, N. G., & Thuan, T. X. 2006, *Astronomy and Astrophysics*, 448, 955

Izotov, Y. I., Worseck, G., Schaerer, D., et al. 2021, *Monthly Notices of the Royal Astronomical Society*, arXiv:2103.01514

Jaskot, A. E., Dowd, T., Oey, M. S., Scarlata, C., & McKinney, J. 2019, *The Astrophysical Journal*, 885, 96

Jones, T., Ellis, R., Jullo, E., & Richard, J. 2010, *The Astrophysical Journal*, 725, L176

Jones, T., Ellis, R. S., Richard, J., & Jullo, E. 2013, *Astrophysical Journal*, 765, 48

Jones, T., Martin, C., & Cooper, M. C. 2015, *The Astrophysical Journal*, 813, 126

Jones, T., Stark, D. P., & Ellis, R. S. 2018, *Astrophysical Journal*, 863, 191

Kashino, D., Silverman, J. D., Sanders, D., et al. 2017, *Astrophysical Journal*, 835, 88

—. 2019, *Astrophysical Journals*, 241, 10

- Kennicutt, R. C. 1998, *Annual Review of Astronomy and Astrophysics*, 36, 189
- Kewley, L. J., Dopita, M. A., Leitherer, C., et al. 2013a, *Astrophysical Journal*, 774, 100
- Kewley, L. J., Dopita, M. A., Sutherland, R. S., Heisler, C. A., & Trevena, J. 2001, *Astrophysical Journal*, 556, 121
- Kewley, L. J., Groves, B., Kauffmann, G., & Heckman, T. 2006, *Monthly Notices of the Royal Astronomical Society*, 372, 961
- Kewley, L. J., Maier, C., Yabe, K., et al. 2013b, *Astrophysical Journal*, 774, L10
- Kriek, M., van Dokkum, P. G., Labb, I., et al. 2009, *The Astrophysical Journal*, 700, 221
- Kriek, M., Shapley, A. E., Reddy, N. A., et al. 2015, *The Astrophysical Journal Supplement Series*, 218, 15
- Krumholz, M. R., & Ting, Y.-S. 2018, *Monthly Notices of the Royal Astronomical Society*, 475, 2236
- Lacey, C., & Cole, S. 1993, *Monthly Notices of the Royal Astronomical Society: Letters*, 262, 627
- Larkin, J., Barczys, M., Krabbe, A., et al. 2006, in *Ground-based and Airborne Instrumentation for Astronomy*, ed. I. S. McLean & M. Iye, Vol. 6269, International Society for Optics and Photonics (SPIE), 441 – 445
- Leethochawalit, N., Jones, T. A., Ellis, R. S., et al. 2016, *The Astrophysical Journal*, 820, 84
- Liang, Y. C., Hammer, F., Yin, S. Y., et al. 2007, *Astronomy and Astrophysics*, 473, 411
- Lilly, S. J., Carollo, C. M., Pipino, A., Renzini, A., & Peng, Y. 2013, *Astrophysical Journal*, 772, 119
- Livermore, R. C., Jones, T. A., Richard, J., et al. 2015, *Monthly Notices of the Royal Astronomical Society*, 450, 1812
- Lotz, J. M., Koekemoer, A., Coe, D., et al. 2017, *The Astrophysical Journal*, 837, 97
- Ma, X., Hopkins, P. F., Feldmann, R., et al. 2017, *Monthly Notices of the Royal Astronomical Society*, 466, 4780
- Madau, P., & Dickinson, M. 2014, *Annual Review of Astronomy and Astrophysics*, 52, 415
- Mason, C. A., Treu, T., Fontana, A., et al. 2017, *The Astrophysical Journal*, 838, 14
- Masters, D., Faisst, A., & Capak, P. 2016, *Astrophysical Journal*, 828, 18
- Masters, D., McCarthy, P., Siana, B., et al. 2014, *Astrophysical Journal*, 785, 153

- McGaugh, S. S., Rubin, V. C., & de Blok, W. J. G. 2001, *The Astronomical Journal*, 122, 2381
- Meurer, G. R., Heckman, T. M., & Calzetti, D. 1999, *The Astrophysical Journal*, 521, 64
- Momcheva, I. G., Brammer, G. B., van Dokkum, P. G., et al. 2016, *The Astrophysical Journal Supplement Series*, 225, 27
- Mostardi, R. E., Shapley, A. E., Steidel, C. C., et al. 2015, *Astrophysical Journal*, 810, 107
- Navarro, J. F., Frenk, C. S., & White, S. 1996, *The Astrophysical Journal*, 462, 563
- Navarro, J. F., Ludlow, A., Springel, V., et al. 2010, *Monthly Notices of the Royal Astronomical Society*, 402, 21
- Newman, J. A., Cooper, M. C., Davis, M., et al. 2013, *The Astrophysical Journal Supplement Series*, 208, 5
- Newman, S. F., Griffin, K. S., Genzel, R., et al. 2012, *The Astrophysical Journal*, 752, 111
- Oñorbe, J., Boylan-Kolchin, M., Bullock, J. S., et al. 2015, *Monthly Notices of the Royal Astronomical Society*, 454, 2092
- Oey, M. S., Meurer, G. R., Yelda, S., et al. 2007, *Astrophysical Journal*, 661, 801
- Oh, S.-H., Brook, C., Governato, F., et al. 2011, *Astronomical Journal*, 142, 24
- Patrício, V., Christensen, L., Rhodin, H., Cañameras, R., & Lara-López, M. A. 2018, *Monthly Notices of the Royal Astronomical Society*, 481, 3520
- Pettini, M., & Pagel, B. E. J. 2004, *Monthly Notices of the Royal Astronomical Society*, 348, L59
- Pilyugin, L. S., & Thuan, T. X. 2005, *Astrophysical Journal*, 631, 231
- Planck Collaboration, Aghanim, N., Akrami, Y., et al. 2018, arXiv e-prints, arXiv:1807.06209
- . 2020, *Astronomy and Astrophysics*, 641, A1
- Pontzen, A., & Governato, F. 2012, *Monthly Notices of the Royal Astronomical Society*, 421, 3464
- Postman, M., Coe, D., Bentez, N., et al. 2012, *The Astrophysical Journal Supplement Series*, 199, 25
- Read, J. I., Agertz, O., & Collins, M. L. M. 2016, *Monthly Notices of the Royal Astronomical Society*, 459, 2573
- Read, J. I., Walker, M. G., & Steger, P. 2018, ArXiv e-prints, arXiv:1808.06634
- Read, J. I., Wilkinson, M. I., Evans, N. W., Gilmore, G., & Kleyna, J. T. 2006, *Monthly Notices of the Royal Astronomical Society*, 367, 387

- Reddy, N. A., Shapley, A. E., Sanders, R. L., et al. 2018, *Astrophysical Journal*, 869, 92
- Runco, J. N., Shapley, A. E., Sanders, R. L., et al. 2021, *Monthly Notices of the Royal Astronomical Society*, 502, 2600
- Sánchez, S. F., Pérez, E., Sánchez-Blázquez, P., et al. 2016a, *Revista Mexicana de Astronomía y Astrofísica*, 52, 21
- . 2016b, *Revista Mexicana de Astronomía y Astrofísica*, 52, 171
- Sanders, R. L., Shapley, A. E., Zhang, K., & Yan, R. 2017, *Astrophysical Journal*, 850, 136
- Sanders, R. L., Shapley, A. E., Kriek, M., et al. 2016a, *Astrophysical Journal*, 825, L23
- . 2016b, *Astrophysical Journal*, 816, 23
- . 2018, *Astrophysical Journal*, 858, 99
- Sanders, R. L., Shapley, A. E., Reddy, N. A., et al. 2020a, *Monthly Notices of the Royal Astronomical Society*, 491, 1427
- Sanders, R. L., Jones, T., Shapley, A. E., et al. 2020b, *Astrophysical Journal*, 888, L11
- Sanders, R. L., Shapley, A. E., Jones, T., et al. 2021a, *Astrophysical Journal*, 914, 19
- . 2021b, *Astrophysical Journal*, 914, 19
- Shapley, A. E., Reddy, N. A., Kriek, M., et al. 2015, *The Astrophysical Journal*, 801, 88
- Shapley, A. E., Sanders, R. L., Shao, P., et al. 2019, *Astrophysical Journal*, 881, L35
- Shivaei, I., Reddy, N. A., Shapley, A. E., et al. 2015, *Astrophysical Journal*, 815, 98
- Shivaei, I., Kriek, M., Reddy, N. A., et al. 2016, *Astrophysical Journal*, 820, L23
- Simon, J. D. 2019, *Annual Review of Astronomy and Astrophysics*, 57, 375
- Simons, R. C., Kassin, S. A., Trump, J. R., et al. 2016, *The Astrophysical Journal*, 830, 14
- Sparre, M., Hayward, C. C., Feldmann, R., et al. 2017, *Monthly Notices of the Royal Astronomical Society*, 466, 88
- Speagle, J. S., Steinhardt, C. L., Capak, P. L., & Silverman, J. D. 2014, *Astrophysical Journal*, 214, 15
- Spergel, D. N., & Steinhardt, P. J. 2000, *Phys. Rev. Lett.*, 84, 3760
- Stark, D. P., Swinbank, A. M., Ellis, R. S., et al. 2008, *Nature*, 455, 775
- Steidel, C. C., Strom, A. L., Pettini, M., et al. 2016, *Astrophysical Journal*, 826, 159
- Steidel, C. C., Rudie, G. C., Strom, A. L., et al. 2014, *The Astrophysical Journal*, 795, 165

- Stott, J. P., Swinbank, A. M., Johnson, H. L., et al. 2016, *Monthly Notices of the Royal Astronomical Society*, 457, 1888
- Strait, V., Bradač, M., Hoag, A., et al. 2018, ArXiv e-prints, arXiv:1805.08789
- Strom, A. L., Steidel, C. C., Rudie, G. C., Trainor, R. F., & Pettini, M. 2018, *Astrophysical Journal*, 868, 117
- Teyssier, R., Pontzen, A., Dubois, Y., & Read, J. I. 2013, *Monthly Notices of the Royal Astronomical Society*, 429, 3068
- Topping, M. W., Shapley, A. E., Reddy, N. A., et al. 2020a, *Monthly Notices of the Royal Astronomical Society*, 499, 1652
- . 2020b, *Monthly Notices of the Royal Astronomical Society*, 495, 4430
- Treu, T., Schmidt, K. B., Brammer, G. B., et al. 2015, *The Astrophysical Journal*, 812, 114
- Troncoso, P., Maiolino, R., Sommariva, V., et al. 2014, *Astronomy and Astrophysics*, 563, A58
- Viel, M., Lesgourgues, J., Haehnelt, M. G., Matarrese, S., & Riotto, A. 2005, *Phys. Rev. D*, 71, 063534
- Vogelsberger, M., Zavala, J., Simpson, C., & Jenkins, A. 2014, *Monthly Notices of the Royal Astronomical Society*, 444, 3684
- Wang, X., Jones, T. A., Treu, T., et al. 2017, *The Astrophysical Journal*, 837, 89
- Wang, X., Jones, T. A., Treu, T., et al. 2018, ArXiv e-prints, arXiv:1808.08800
- Wechsler, R. H., & Tinker, J. L. 2018, *Annual Review of Astronomy and Astrophysics*, 56, 435
- Wright, S. A., Larkin, J. E., Graham, J. R., & Ma, C.-P. 2010, *The Astrophysical Journal*, 711, 1291
- Wuyts, S., Schreiber, N. M. F., Wisnioski, E., et al. 2016, *The Astrophysical Journal*, 831, 149
- Yuan, T. T., Kewley, L. J., Swinbank, A. M., & Richard, J. 2012, *Astrophysical Journal*, 759, 66
- Zahid, H. J., Dima, G. I., Kudritzki, R.-P., et al. 2014, *Astrophysical Journal*, 791, 130
- Zahid, H. J., Geller, M. J., Kewley, L. J., et al. 2013, *The Astrophysical Journal Letters*, 771, L19
- Zastrow, J., Oey, M. S., Veilleux, S., & McDonald, M. 2013, *Astrophysical Journal*, 779, 76
- Zastrow, J., Oey, M. S., Veilleux, S., McDonald, M., & Martin, C. L. 2011, *The Astrophysical Journal*, 741, L17

Zavala, J., Vogelsberger, M., & Walker, M. G. 2013, Monthly Notices of the Royal Astronomical Society: Letters, 431, L20

Zhang, K., Yan, R., Bundy, K., et al. 2016, Monthly Notices of the Royal Astronomical Society, 466, 3217